

DESIGNING MULTI-COMPONENT OXIDES AS AIR CATHODE FOR
RECHARGEABLE AQUEOUS Zn-AIR BATTERIES

A THESIS SUBMITTED TO
THE GRADUATE SCHOOL OF NATURAL AND APPLIED SCIENCES
OF
MIDDLE EAST TECHNICAL UNIVERSITY

BY

ÇAĞLA ÖZGÜR

IN PARTIAL FULFILLMENT OF THE REQUIREMENTS
FOR
THE DEGREE OF MASTER OF SCIENCE
IN
METALLURGICAL AND MATERIALS ENGINEERING

AUGUST 2024

Approval of the thesis:

**DESIGNING MULTI-COMPONENT OXIDES AS AIR CATHODE FOR
RECHARGEABLE AQUEOUS Zn-AIR BATTERIES**

submitted by **ÇAĞLA ÖZGÜR** in partial fulfillment of the requirements for the degree of **Master of Science in Metallurgical and Materials Engineering, Middle East Technical University** by,

Prof. Dr. Naci Emre Altun
Dean, **Graduate School of Natural and Applied Sciences** _____

Prof. Dr. Ali Kalkanlı
Head of the Department, **Metallurgical and Materials Engineering** _____

Assoc. Prof. Dr. Çiğdem Toparlı
Supervisor, **Metallurgical and Materials Engineering, METU** _____

Examining Committee Members:

Prof. Dr. Mehmet Kadri Aydınol
Metallurgical and Materials Eng., METU _____

Assoc. Prof. Dr. Çiğdem Toparlı
Metallurgical and Materials Eng., METU _____

Prof. Dr. Hüsnü Emrah Ünalın
Metallurgical and Materials Eng., METU _____

Assist. Prof. Dr. Gökhan Çelik
Chemical Eng., METU _____

Assoc. Prof. Dr. Burak Ülgüt
Chemistry, Bilkent Uni. _____

Date: 16.08.2024

I hereby declare that all information in this document has been obtained and presented in accordance with academic rules and ethical conduct. I also declare that, as required by these rules and conduct, I have fully cited and referenced all material and results that are not original to this work.

Name Last name : Çaęla Özgür

Signature :

ABSTRACT

DESIGNING MULTI-COMPONENT OXIDES AS AIR CATHODE FOR RECHARGEABLE AQUEOUS ZN-AIR BATTERIES

Özgür, Çağla

Master of Science, Metallurgical and Materials Engineering

Supervisor : Assoc. Prof. Dr. Çiğdem Toparlı

August 2024, 120 pages

To address environmental pollution concerns and meet the increasing energy demand, the development of renewable energy systems and cost-effective electrochemical energy storage solutions is essential. Rechargeable zinc-air batteries have gathered significant attention among various energy storage devices due to their high specific energy, cost-effectiveness, and environmental friendliness. However, the sluggish kinetics of the oxygen reduction reaction (ORR) and oxygen evolution reaction (OER) during the discharge and recharge process of the air cathode hinder large-scale application. Thus, designing robust and economically viable bifunctional oxygen electrocatalysts is crucial for the commercialization of Zn-air batteries. In this thesis, multicomponent oxide bifunctional electrocatalysts namely high entropy oxides (HEOs) and double perovskite oxides for Zn-air batteries are thoroughly investigated. The effect of oxygen vacancy, porosity, and doping on the electrocatalytic OER/ORR activity and Zn-air battery performance are explored.

Firstly, we introduce a novel synthesis method to produce $(\text{FeCrCoMnZn})_3\text{O}_{4-\delta}$ high entropy spinel oxide in a vacuum atmosphere, primarily aimed at incorporating oxygen vacancies into the crystal structure. Compared to its air-synthesized counterpart, the resulting HEO with abundant oxygen vacancies exhibits a better bifunctional index of 0.89 V, indicating enhanced electrocatalytic activity for oxygen

reactions. When used as electrocatalysts in the air cathode of Zn-air batteries, the vacuum-synthesized HEO catalysts outperform HEO treated in air, demonstrating superior peak power density, specific capacity, and cycling stability. Then, we applied a low-temperature sol-gel method to synthesize nano-porous $(\text{FeCrCoMnZn})_3\text{O}_{4-\delta}$ powders. To understand the effect of pore size on the electrocatalytic activity, calcination is applied at various temperatures. The HEO powder treated at 600°C exhibits larger pore size and a higher concentration of oxygen vacancies compared to other electrocatalysts calcined at 500°C and 700°C . When used as an air cathode in a Zn-air battery, the HEO treated at 600°C achieves greater capacity and peak power density. Notably, the Zn-air battery with nanoporous HEO treated at 600°C maintains its stability even after 1000 hours of cyclic charge-discharge, demonstrating exceptional stability and durability. Finally, we synthesized B-site doped $\text{NdBaCo}_a\text{Fe}_{2-a}\text{O}_{5+\delta}$ ($a= 1.0, 1.4, 1.6, 1.8$) electrocatalysts to understand the effect of cobalt and iron amount on the B-site of double perovskite oxides. X-ray photoelectron spectroscopy analysis revealed a correlation between iron reduction and increased oxygen vacancy content, which influences the electrocatalyst's bifunctionality by lowering the work function. The electrocatalyst with the highest cobalt content, $\text{NdBaCo}_{1.8}\text{Fe}_{0.2}\text{O}_{5+\delta}$, exhibited a bifunctionality value of 0.95 V, outperforming the other synthesized electrocatalysts. As an air cathode in a Zn-air battery, $\text{NdBaCo}_{1.8}\text{Fe}_{0.2}\text{O}_{5+\delta}$ demonstrated superior performance characteristics, including elevated capacity, the highest peak power density, and enhanced durability and stability. Our findings strongly suggest that adjusting the quantity of oxygen vacancies, porosity, and doping of multi-component oxides offers a novel approach to customize electrochemical OER/ORR performance.

Keywords: Zinc-air battery, Oxygen Evolution Reaction, Oxygen Reduction Reaction, Perovskite Oxide, High Entropy Oxide

ÖZ

ŞARJ EDİLEBİLİR SULU ÇİNKO-HAVA PİLLERİ İÇİN ÇOK BİLEŞENLİ OKSİTLERİN HAVA KATODU OLARAK TASARLANMASI

Özgür, Çağla

Yüksek Lisans, Metalurji ve Malzeme Mühendisliği

Tez Yöneticisi: Assoc. Prof. Dr. Çiğdem Toparlı

Ağustos 2024, 120 sayfa

Çevre kirliliği endişelerini gidermek ve artan enerji talebini karşılamak için yenilenebilir enerji sistemlerinin ve uygun maliyetli elektrokimyasal enerji depolama çözümlerinin geliştirilmesi esastır. Şarj edilebilir çinko-hava pilleri, yüksek özgül enerjileri, uygun maliyetli olmaları ve çevre dostu olmaları sebebiyle çeşitli enerji depolama cihazları arasında öne çıkmaktadır. Ancak, deşarj ve şarj işlemi sırasında hava katodunda gerçekleşen oksijen indirgenme reaksiyonunun (ORR) ve oksijen yükseltgenme reaksiyonunun (OER) yavaş kinetiği, büyük ölçekli uygulamayı engellemektedir. Bu nedenle, sağlam ve ekonomik bifonksiyonel oksijen elektro katalizörleri tasarlamak, Zn-hava pillerinin ticarileştirilmesi için çok önemlidir. Bu tezde, Zn-hava pilleri için çok bileşenli oksit bifonksiyonel elektro katalizörler (yüksek entropili oksitler (HEO'lar) ve çift perovskit oksitler) kapsamlı bir şekilde incelenmiştir. Oksijen boşluğunun, gözenekliliğin ve dopingin elektro katalitik OER/ORR aktivitesi ve Zn-hava pil performansı üzerindeki etkisi araştırılmıştır. Öncelikle, kristal yapıya oksijen boşlukları dahil etmeyi amaçlayan vakum atmosferinde $(\text{FeCrCoMnZn})_3\text{O}_{4-\delta}$ yüksek entropili spinel oksit üretmek için yeni bir sentez yöntemi sunuyoruz. Havada sentezlenen muadiliyle karşılaştırıldığında, bol oksijen boşluğuna sahip HEO, oksijen reaksiyonlarında elektrokimyasal aktiviteyi gösteren 0.89 V'luk bifonksiyonel indeksiyle daha iyi

performans sergiliyor. Zn-hava pillerinin hava katodunda elektrokimyasal katalizör olarak kullanıldığında, vakumda sentezlenen HEO katalizörleri havada işlenen HEO'dan daha iyi performans göstererek üstün tepe güç yoğunluğu, özgül kapasite ve çevrim kararlılığı gösteriyor. Daha sonra, nano gözenekli (FeCrCoMnZn)₃O₄- δ tozlarını sentezlemek için düşük sıcaklıklı sol-jel yöntemini uyguladık. Gözenek boyutunun elektrokimyasal aktivite üzerindeki etkisini anlamak için çeşitli sıcaklıklarda kalsinasyon uygulanır. 600°C'de işlenen HEO tozu, 500°C ve 700°C'de kalsine edilen diğer elektro katalizörlere kıyasla daha büyük gözenek boyutu ve daha yüksek oksijen boşlukları konsantrasyonu sergiler. Bir Zn-hava pilinde hava katodu olarak kullanıldığında, 600°C'de işlenen HEO daha büyük kapasite ve tepe güç yoğunluğuna ulaşır. Özellikle, 600°C'de işlenen nanogözenekli HEO'lu Zn-hava pili, 1000 saatlik döngüsel şarj-deşarjdan sonra bile kararlılığını koruyarak olağanüstü kararlılık ve dayanıklılık gösterir. Son olarak, kobalt ve demir miktarının çift perovskit oksitlerin B-bölgesindeki etkisini anlamak için B-bölgesi katkılı NdBaCo_aFe_{2-a}O_{5+ δ} (a= 1.0, 1.4, 1.6, 1.8) elektro katalizörleri sentezledik. X-ışını fotoelektron spektroskopisi analizi, demir indirgemesi ile artan oksijen boşluğu içeriği arasında bir korelasyon olduğunu ortaya koydu; bu, elektrokatalistin işlevini düşürerek çift işlevliliğini etkiler. En yüksek kobalt içeriğine sahip elektrokatalizör, NdBaCo_{1.8}Fe_{0.2}O_{5+ δ} , 0.95 V'luk bir çift işlevlilik değeri sergileyerek diğer sentezlenen elektrokatalizörlerden daha iyi performans gösterdi. Bir Zn-hava pilinde hava katodu olarak NdBaCo_{1.8}Fe_{0.2}O_{5+ δ} , yükseltilmiş kapasite, en yüksek tepe güç yoğunluğu ve geliştirilmiş dayanıklılık ve kararlılık dahil olmak üzere üstün performans özellikleri gösterdi. Bulgularımız, oksijen boşluklarının miktarını, gözenekliliği ve çok bileşenli oksitlerin katkılanmasını ayarlamamanın, elektrokimyasal OER/ORR performansını özelleştirmek için yeni bir yaklaşım sunduğunu güçlü bir şekilde önermektedir.

Anahtar Kelimeler: Çinko-hava pili, Oksijen Evrim Reaksiyonu, Oksijen İndirgenme Reaksiyonu, Perovskit Oksit, Yüksek Entropili Oksit

To my family...

ACKNOWLEDGMENTS

I would like to express my deepest gratitude to my supervisor, Assoc. Prof. Dr. Çiğdem Toparlı, for her unwavering support, guidance, and encouragement throughout this research. Her insights and expertise have been invaluable in shaping this work. Her mentorship has been a cornerstone of my academic journey, providing not only the intellectual rigor needed to complete this thesis but also a source of inspiration and motivation. Her laughter and positive energy have made even the longest working hours enjoyable, and for that, I am truly grateful.

I also wish to extend my sincere thanks to Assist. Prof. Dr. Ersu Lökçü and Dr. İlker Yıldız for their cooperation and contributions to this project. Their collaboration and input have greatly enhanced the quality of this research. Special thanks to Prof. Dr. Eren Kalay and Can Okuyucu for their assistance with HRTEM analysis, which was crucial for the success of this work.

I am incredibly grateful to my labmates, Ali Burçay Coşkuner, Kasım Erdem Erik, Hüseyin İnan Cihan, Hasan Girgin, Deniz Okan Bayraktar and my colleague and dearest friend Cansu Aygüzer, for their constant support and encouragement. A special thanks to Uygur Geyikçi, whose knowledge and support, especially during the rechargeable Zn-air battery tests, were crucial to my work. I would also like to extend my sincere appreciation to Tuncay Erdil, who has supported my research from the beginning of my master's degree not only with his knowledge but also with his genuine friendship. Each of them brought joy to the laboratory, making the working environment not only productive but also fun and inspiring. Thank you all.

I am profoundly grateful to my parents, Mefaret Özgür and Süleyman Özgür, and my aunts Gülçin Sanal, and Gülşen Turan for their endless love, encouragement, and support throughout this journey. My parents have always instilled in me the importance of hard work, shaping me into the person I am today. Their belief in me

has been my greatest source of strength. Without them, none of this would have been possible.

Lastly, I would like to thank my closest friends, Ece Karaarslan, Edanur Eşmen, Büşra Kandemir, Çağatay Önder, and Kaan Kantar who have been there to lift my spirits whenever I felt frustrated. A special mention goes to Görkem Varol, who has stood by me through thick and thin. He offers care, understanding, and support as my companion through all of life's ups and downs. I am fortunate to have you by my side.

TABLE OF CONTENTS

ABSTRACT	v
ÖZ	vii
ACKNOWLEDGMENTS	x
TABLE OF CONTENTS	xii
LIST OF TABLES	xv
LIST OF FIGURES	xvi
CHAPTERS	
1 INTRODUCTION	1
2 LITERATURE REVIEW	5
2.1 Metal- Air Batteries	5
2.2 Zinc-Air Batteries	6
2.2.1 Design and Working Principle of Rechargeable Zinc-Air Batteries .	7
2.2.2 Oxygen Reduction and Oxygen Evolution Reactions	10
2.3 Components of Rechargeable Zinc-Air Batteries.....	12
2.3.1 Zinc Anode	13
2.3.2 Electrolyte.....	14
2.3.3 Air Cathode and Bifunctional Electrocatalysts for OER and ORR.	15
3 EXPERIMENTAL PROCEDURE.....	23
3.1 Synthesis of (FeCrCoMnZn) ₃ O _{4-δ} Powders in Vacuum and Air Atmosphere.....	23

3.2	Synthesis of Nanoporous (FeCrCoMnZn) ₃ O _{4-δ} Powders	24
3.3	Synthesis of NdBaCo _a Fe _{2-a} O _{5+δ} (a= 1.0, 1.4, 1.6, 1.8) Powders	25
3.4	Materials Characterization	25
3.5	Electrochemical Characterization	27
3.6	Evaluation of the Zn-Air Battery Performance	30
4	RESULTS AND DISCUSSION FOR (FeCrCoMnZn) ₃ O _{4-δ} ELECTROCATALYSTS SYNTHESIZED IN AIR AND VACUUM ATMOSPHERES	33
4.1	Crystal Structure and Morphology of the HEO-Air and HEO-Vac Electrocatalysts	33
4.2	Electronic Structure of the HEO-Air and HEO-Vac Electrocatalysts	39
4.3	OER/ORR Performance of the HEO-Air and HEO-Vac Electrocatalysts 42	
4.4	Materials Characterization after Galvanostatic Stability Test	51
4.5	Evaluation of Zinc-Air Battery Performance of HEO-Air and HEO-Vac Electrocatalysts	54
5	RESULTS AND DISCUSSION FOR NANOPOROUS (FeCrCoMnZn) ₃ O _{4-δ} HIGH ENTROPY OXIDE ELECTROCATALYSTS	59
5.1	Crystal Structure and Morphology of Nanoporous HEOs	59
5.2	Electronic Structure of Nanoporous HEOs	63
5.3	OER/ORR Performance of Nanoporous HEO Electrocatalysts	67
5.4	Zn-Air Battery Performance of Nanoporous HEO Electrocatalysts	71
6	RESULTS AND DISCUSSION FOR NdBaCo _a Fe _{2-a} O _{5+δ} (a= 1.0, 1.4, 1.6, 1.8) DOUBLE PEROVSKITE OXIDE ELECTROCATALYSTS	75
6.1	Crystal Structure and Morphology of NBCF Electrocatalysts	75

6.2	Electronic Structure of NBCF Electrocatalysts	78
6.3	OER/ORR Performance of NBCF Electrocatalysts	81
6.4	Zn-Air Battery Performance of NBCF Electrocatalysts.....	88
6.5	Analysis of the Electronic Structure of Co _{1.8} Fe _{0.2} and CoFe	91
6.6	Materials Characterization after Cyclic Charge/Discharge Battery Test	93
7	CONCLUSIONS	95
	REFERENCES	97

LIST OF TABLES

TABLES

Table 4.1 Rietveld refinement data for HEO-Air	35
Table 4.2 Rietveld refinement data for HEO-Vac	36
Table 4.3 Bet analysis data for HEO-Air	46
Table 4.4 Bet analysis data for HEO-Vac	47
Table 6.1 Lattice parameters, crystal volume, crystal structure and space group for CoFe, Co _{1.4} Fe _{0.6} , Co _{1.6} Fe _{0.4} and Co _{1.8} Fe _{0.2}	76

LIST OF FIGURES

FIGURES

Figure 2.1 Comparison for different metal-air batteries in terms of specific energies, volumetric energy densities, and cell voltages [52].	6
Figure 2.2 Schematic of a typical rechargeable Zn-air battery [48].	8
Figure 2.3 (a) Pourbaix diagram of oxygen and zinc (b) Schematic illustration of corrosion, dendrite growth, and HEO on Zn [39]	13
Figure 2.4 (a) Schematic illustration of the catalyst-loaded gas diffusion electrode (GDE) in contact with the liquid electrolyte, designed to facilitate the easy permeation of oxygen from the surrounding atmosphere and its reduction on supported electrocatalysts (b) SEM image of commercial Toray carbon paper treated with hydrophobic PTFE [65].	16
Figure 2.5 Different crystal structures, and elements for HEOs that is researched in the electrochemical applications [118]	19
Figure 2.6 Center shows the crystal structure of a cubic perovskite oxide while in the outer circle double perovskite oxides with different crystal structure such as rock-salt, layered etc. are presented.	22
Figure 3.1 Schematic illustrating the sequential procedures in the synthesis of $(\text{FeCrCoMnZn})_3\text{O}_{4-\delta}$ HEO under vacuum conditions.	23
Figure 3.2 Schematic illustrating the sequential procedures in the synthesis of GLY500, GLY600, and GLY700 nanoporous HEOs	24
Figure 3.3 Schematic illustrating the sequential procedures in the synthesis of NBCF double perovskite oxides.	25
Figure 3.4 (a) RDE set-up (b) Three electrode cell set-up for long-term stability.	30
Figure 3.5 Rechargeable Zn-air battery testing with Neware battery testing system	31
Figure 4.1 (a) XRD patterns of HEO-Air and HEO-Vac. Rietveld refinement analysis performed for (b) HEO-Air (c) HEO-Vac	34

Figure 4.2 HEO-Vac's (a) BF TEM image and the inset displays the SAED pattern from $\langle 211 \rangle$ zone axis (b) HRTEM image and the inset shows the FFT pattern (c) HADDF image and corresponding EDS element mapping of Fe, Cr, Co, Mn, Zn, and O. HEO-Air's (d) BF TEM and the inset displays the SAED pattern from the $\langle 211 \rangle$ zone axis (e) HRTEM image and inset shows the FFT pattern (f) HADDF image and corresponding EDS element mapping of Fe, Cr, Co, Mn, Zn, and O.....	38
Figure 4.3 Deconvolution of XPS core level spectra for (a) Fe 2p (b) Cr 2p (c) Co 2p (d) Mn 2p, and (e) Zn 2p.....	40
Figure 4.4 HEO-Air and HEO-Vac electrocatalyst's (a) O 1s XPS core level spectra (b) EPR spectrum.....	41
Figure 4.5 HEO- Air and HEO-Vac electrocatalyst's (a) LSV curves at OER region (b) Tafel plots (c) EIS data (d) Electric double layer capacitance analysis (e) Mass activity and specific activity calculations (f) Galvanostatic stability curve recorded at a current density of 10 mA cm^{-2}	43
Figure 4.6 Multistep chronoamperometry to determine the Tafel slopes for HEO-Air and HEO-Vac.....	44
Figure 4.7 Cyclic Voltammetry (CV) scans were conducted for (a) HEO-Air (b) HEO-Vac at scan rates of 10, 20, 30, 40, 60, 80, 100, and 120 mV s^{-1}	45
Figure 4.8 HEO- Air and HEO- Vac electrocatalysts' (a) ORR activity curves (b) Tafel plots (c) Koutecky-Levich plots at 0.15V (d) Kinetic current density (J_k) and electron transfer number (n).....	48
Figure 4.9 At 400, 800, 1200, 1600, 2000 rpm rotation speeds (a) LSV experiments for HEO-Air and (b) LSV experiments HEO-Vac. At potentials ranging from 0.50 to 0.15 V, Koutecky-Levich (K-L) for (c) HEO-Air and (d) HEO-Vac.....	50
Figure 4.10 XRD patterns of the HEO-Air, HEO-Vac and the carbon foam-coated nickel after the galvanostatic stability test.....	51
Figure 4.11 HRTEM after the galvanostatic stability test for HEO-Vac and HEO-Air. HEO-Vac's (a) BF TEM image, with the SAED pattern inside (b,c) HRTEM images, with the insets showing the FFT signals (d) HAADF image and subsequent EDS elemental mapping. HEO-Airs' (e,f) BF TEM images, with the inset displaying	

the SAED pattern (g) HRTEM analysis, with the inset showing the FFT signal (h) HAADF image and EDS elemental mapping.....	53
Figure 4.12 HEO-Air and HEO-Vac based Zn-air battery's (a) charge and discharge polarization curves and peak power density plots (b) specific capacities at 5, 10, 20, and 50 mA cm ⁻² current densities (c) rate capability study (d) cyclic charge-discharge curves (e) coulombic efficiencies (f) durability performance over the first seven cycles of cyclic charge-discharge (g) open circuit voltage of the HEO-Vac based Zn-air battery, and (h-i) digital photographs of the operating HEO-Vac based Zn-air battery.....	57
Figure 5.1 (a) XRD patterns of GLY500, GLY600, and GLY700 nanoporous HEOs. Rietveld refinement analysis of (b) GLY500 (c) GLY600 (d)GLY700.....	59
Figure 5.2 SEM images of GLY500 (a) at 20000x magnification (b) at 10000x mag. (c) at 5000x mag. (d) EDS Mapping of GLY500 for Fe, Cr, Co, Mn, Zn, and O. SEM images of GLY600 (e) at 20000x mag. (f) at 10000x mag. (g) at 5000x mag. (h) EDS Mapping of GLY600. SEM images of GLY700 (i) at 20000x mag. (j) at 10000x mag. (k) at 5000x mag. (l) EDS Mapping of GLY700.	61
Figure 5.3 (a) BF TEM image of GLY500 and the inset shows the SAED pattern (b) HRTEM image of GLY500 and the inset shows the FFT pattern (c) BF TEM image of GLY600 and the inset shows the SAED pattern (d) HRTEM image of GLY600 and inset shows the FFT pattern (e) BF TEM image of GLY700 and the inset shows the SAED pattern (f) HRTEM image of GLY700 and the inset shows the FFT pattern	63
Figure 5.4 XPS core level spectra and corresponding deconvolution of (a) Fe 2p (b) Co 2p (c) Cr 2p (d) Mn 2p, and (e) Zn 2p for GLY500, GLY600, and GLY700...	65
Figure 5.5 O 1s XPS core level spectra for (a) GLY500 (b) GLY600 (c) GLY700	66
Figure 5.6 GLY500, GLY600 and GLY700 nanoporous HEO electrocatalysts' (a) LSV curves (b) Tafel plots (c) Fitted EIS data (d) Electric double layer capacitance analysis results (e) MA and SA activity calculations	68
Figure 5.7 CV scans at scan rates 10, 20, 30, 40, 60, 80, 100, and 120 mV s ⁻¹ for (a) GLY500 (b) GLY600 (c) GLY700	69

Figure 5.8 GLY500, GLY600 and GLY700 nanoporous HEO electrocatalysts' (a) ORR activity curves (b) Tafel plots	70
Figure 5.9 Zn-air batteries with nanoporous GLY500, GLY600, and GLY700 HEO electrocatalyst's (a) Peak power density plots along with charge and discharge polarization curves (b) Capacities at a current density of 5 mA cm ⁻² (c) Capacities at a current density of 10 mA cm ⁻² (d) Capacities at a current density of 20 mA cm ⁻² (e) Rate capability study from 0 to 20 mA cm ⁻² and back to 0 mA cm ⁻² (f) Durability performance during the first hour of cyclic charge-discharge (g) Cyclic charge-discharge performance at 5 mA cm ⁻²	74
Figure 6.1 (a) XRD patterns of NBCF double perovskite oxides. Rietveld refinement analysis for (b) CoFe (c) Co _{1.4} Fe _{0.6} (d) Co _{1.6} Fe _{0.4} and (e) Co _{1.8} Fe _{0.2}	76
Figure 6.2 SEM images of CoFe (a) at 50000x magnification (b) at 10000x mag. (c) EDS Mapping of CoFe for Nd, Ba, Co,Fe, and O. SEM images of Co _{1.4} Fe _{0.6} (d) at 50000x mag. (e) at 10000x mag. (f) EDS Mapping of Co _{1.4} Fe _{0.6} . SEM images of Co _{1.6} Fe _{0.4} (g) at 50000x mag. (h) at 10000x mag. (i) EDS Mapping of Co _{1.6} Fe _{0.4} SEM images of Co _{1.8} Fe _{0.2} (j) at 50000x mag. (k) at 10000x mag. (l) EDS Mapping of Co _{1.8} Fe _{0.2}	77
Figure 6.3 XPS core level spectra and corresponding deconvolution of Fe 2p and Co2p respectively for (a,b) CoFe (c,d) Co _{1.4} Fe _{0.6} (e,f) Co _{1.6} Fe _{0.4} (g,h) Co _{1.8} Fe _{0.2}	79
Figure 6.4 O 1s XPS core level spectra for (a) CoFe (b) Co _{1.4} Fe _{0.6} (c) Co _{1.6} Fe _{0.4} (d) Co _{1.8} Fe _{0.2}	80
Figure 6.5 For CoFe, Co _{1.4} Fe _{0.6} , Co _{1.6} Fe _{0.4} and Co _{1.8} Fe _{0.2} double perovskite oxide electrocatalysts (a) LSV curves in OER region (b) Tafel plots (c) EIS data with corresponding electrical circuit (d) Electric double layer capacitance measurements (e) MA and SA analysis (f) Mott-Schottky plots.....	82
Figure 6.6 CV scans conducted at scan rates of 10, 20, 30, 40, 60, 80, 100, and 120 mV s ⁻¹ for a) CoFe (b) Co _{1.4} Fe _{0.6} (c) Co _{1.6} Fe _{0.4} (d) Co _{1.8} Fe _{0.2}	83

Figure 6.7 For NBCF electrocatalysts (a) ORR activity curves (b) Tafel plots (c) Koutecky-Levich plots at 0.15V (d) Kinetic current density (J_k) and electron transfer number (n).	85
Figure 6.8 LSV curves at 400, 800, 1200,1600, and 200 rpm of (a) CoFe (b) Co _{1.4} Fe _{0.6} (c) Co _{1.6} Fe _{0.4} (d) Co _{1.8} Fe _{0.2}	86
Figure 6.9 KL plots at 0.15, 0.20, 0.25, 0.30, 0.40 V of (a) CoFe (b) Co _{1.4} Fe _{0.6} (c) Co _{1.6} Fe _{0.4} (d) Co _{1.8} Fe _{0.2}	87
Figure 6.10 Zn-air batteries with NBCF-based air cathodes' (a) Peak power density plots along with charge and discharge polarization curves (b) Capacities at a current density of 5 mA cm ⁻² (c) Capacities at a current density of 10 mA cm ⁻² (d) Capacities at a current density of 50 mA cm ⁻² (e) Rate capability study (f) Durability performance during the first hour of cyclic charge-discharge (g) Cyclic charge-discharge performance at 5 mA cm ⁻²	91
Figure 6.11 (a) UPS spectra and (b) XPS valence band spectra of CoFe, and Co _{1.8} Fe _{0.2}	92
Figure 6.12 XRD patterns of Co _{1.8} Fe _{0.2} before and after the cyclic charge-discharge experiment in the Zn-air battery.	93

CHAPTER 1

INTRODUCTION

Renewable energy sources such as solar and wind power have emerged as the most promising alternatives to traditional fossil fuels. However, effectively storing the energy generated from these sources is a significant challenge. Thus, developing advanced energy storage systems which are reliable, efficient, and highly safe is very important. Zinc-air (Zn-air) batteries have gained significant attention as a potential and sustainable solution for future electrochemical energy storage because of their high theoretical specific energy densities, safety features, and cost-effectiveness [1–4]. Although Zn-air batteries are promising for grid energy storage, it is still essential to have an economically feasible, highly efficient, and chemically stable catalyst for both the oxygen evolution reaction (OER) and the oxygen reduction reaction (ORR) at the air cathode to make Zn-air batteries practically viable [5–7]. Currently, state-of-the-art platinum group electrocatalysts like Pt/C, IrO₂, and RuO₂ are used to accelerate these reactions. However, despite their high bifunctional activity for both OER and ORR, their high cost and scarcity limit the commercial potential of Zn-air batteries [8–10]. Therefore, designing durable, efficient, and cost-effective bifunctional electrocatalysts both for OER and ORR is critical for their application in the air cathode of rechargeable Zn-air batteries [11,12].

Recently, high entropy oxides (HEOs) and double perovskite oxides, particularly those containing transition metals in their structure, have gained significant attention in electrochemical applications [7,13–18]. HEOs are single-phase oxides containing five or more elements in their structure in equal molar or near equal molar ratios. Especially, HEOs containing 3d transition metals have shown remarkable electrocatalytic activity for oxygen reactions [19–22]. Double perovskite oxides (A₂BB'O_{5+δ}) are currently being explored as potential electrocatalysts due to their tunable properties, and enhanced stabilities [23]. Their surface electronic structure

can be changed and active sites for electrochemical reactions can be increased, for example by doping [24–26]. Additionally, oxygen vacancies significantly affect material properties such as ionic/electronic conductivity, electronic structure, and magnetic characteristics of both HEOs and double perovskite oxides [27–30]. Previous research has demonstrated that an optimal number of oxygen vacancies can enhance the OER and ORR activity in transition metal oxides [29,31]. This improvement is attributed to significant alterations in bulk properties such as energy levels and conductivity, along with changes in surface properties and molecular adsorption. [32,33]. Various techniques have been utilized to generate oxygen vacancies in metal oxides, involving both during synthesis methods and post-synthesis treatments [34–36]. These methods include thermal treatment, reduction processes, cation/anion doping, plasma treatment, and other advanced techniques like laser processing, flame treatment, exfoliation, and template strategies [37,38].

In this thesis, HEO and double perovskite oxide OER/ORR electrocatalysts were synthesized for an air cathode application on rechargeable Zn-air batteries. Firstly, to understand the effect of oxygen vacancy content on the electrocatalytic activity of HEOs, our objective is to create an oxygen vacancy-rich spinel $(\text{FeCrCoMnZn})_3\text{O}_{4-\delta}$ HEO using a fast and efficient one-step synthesis approach. We employed the coprecipitation method followed by sintering in both air and vacuum conditions. Transitioning from an air to a vacuum environment during synthesis resulted in a higher production of oxygen vacancies. A higher concentration of oxygen vacancies significantly improved the electrocatalytic performance of $(\text{FeCrCoMnZn})_3\text{O}_{4-\delta}$. The sample treated in a vacuum demonstrated superior OER/ORR performance with lower overpotentials compared to the sample treated in air. Both electrocatalysts were tested as an air cathode in a custom-made Zn-air battery cell. The Zn-air battery with vacuum-calcined $(\text{FeCrCoMnZn})_3\text{O}_{4-\delta}$ exhibited a peak power density of 102 mW cm^{-2} and a specific capacity of $576.07 \text{ mA h g}^{-1}$ at 5 mA cm^{-2} . Additionally, it demonstrated superior cycling stability compared to the battery with air-calcined $(\text{FeCrCoMnZn})_3\text{O}_{4-\delta}$ [12]. Then, to understand the effect of pore structure and pore size on the OER/ORR performance of HEOs, we successfully produced

(FeCrCoMnZn)₃O_{4-δ} nano-porous HEOs using a pore-forming aging process conducted at low temperatures. After producing our (FeCrCoMnZn)₃O_{4-δ} powders by low-temperature sol-gel method using glycine we applied calcination at 500 °C, 600 °C, and 700 °C. Then, we investigated the porous nature of our electrocatalysts by scanning electron microscopy (SEM) and high-resolution electron microscopy (HRTEM). The HEO powder treated at 600°C exhibits bigger pore size as compared to other electrocatalysts. In addition, X-Ray photoelectron spectroscopy (XPS) revealed that (FeCrCoMnZn)₃O_{4-δ} treated at 600°C has higher oxygen vacancy content in its structure which influences its OER/ORR activity. When applied to a rechargeable Zn-air battery as an air cathode, the electrocatalyst treated at 600°C reaches a capacity of 443.34 mA h at 5 mA cm⁻², and a peak power density of 80 mW cm⁻² at a current density of 133 mA cm⁻². More importantly, the Zn-air battery with nano-porous (FeCrCoMnZn)₃O_{4-δ} treated at 600°C does not lose its stability even after 1000 hours (over 1.5 months) cyclic charge-discharge. Hence, it shows outstanding stability and durability.

Finally, we designed double perovskite oxide electrocatalysts by doping the B-site for rechargeable Zn-air battery application. A series of NdBaCo_aFe_{2-a}O_{5+δ} (NBCF) double perovskite oxides were synthesized with cobalt and iron ratios denoted by 'a' values of 1.0, 1.4, 1.6, and 1.8. Our study systematically evaluated B-site doped double perovskite oxide's bifunctional electrocatalytic performance focusing on how variations in cobalt and iron content affect their OER/ORR activity. The NBCF electrocatalysts were synthesized by modified sol-gel Pechini method and then they were subjected to calcination. The electrocatalyst with the lowest iron content, NdBaCo_{1.8}Fe_{0.2}O_{5+δ}, significantly shows superior performance when it is used in a rechargeable Zn-air battery as compared to other NBCF double perovskite oxides. Zn-air battery with the NdBaCo_{1.8}Fe_{0.2}O_{5+δ} electrocatalyst demonstrated a maximum capacity of 428.27 mA h at 10 mA cm⁻², a peak power density of 64 mW cm⁻², and outstanding durability and stability with maintaining its performance over 350 hours of cyclic charge-discharge [39].

CHAPTER 2

LITERATURE REVIEW

2.1 Metal- Air Batteries

Metal-air batteries are viewed as a next-generation promising energy storage device with their high energy densities, and cost-effectiveness. Metal-air batteries have a unique half-open cell structure. They are mainly composed of a metal anode such as lithium (Li), sodium (Na), potassium (K), magnesium (Mg), aluminum (Al), zinc (Zn) and iron (Fe), and air cathode which utilizes oxygen (O_2) in the ambient air [40–42]. In Figure 2.1 theoretical specific energies, volumetric energy densities, and cell voltages for different metal anodes are presented. Among the various metal-air batteries, Li-air batteries are widely investigated since Li-air batteries offer the highest theoretical energy density and high battery voltage, theoretically. However, they have safety problems and Li is an expensive, and scarce metal [43–45]. Alkali metal-based metal-air batteries such as Na, Li, and K are highly susceptible to water and moisture, presenting safety concerns in aqueous environments. Hence, they are used mainly in non-aqueous systems, but non-aqueous metal-air batteries suffer from low coulombic efficiency and self-discharge. Therefore, the practical application of these batteries is inhibited [46,47]. Al-air and Mg-air batteries also have similar theoretical energy densities and operating cell voltages as compared to Li-air batteries. However, they show self-discharge phenomena and low coulombic efficiency resulting from their low reduction potential. In addition, they have challenges such as parasitic corrosion due to the hydrogen evolution reaction (HER) on Al and Mg electrode surfaces. Moreover, they cannot be rechargeable because, in aqueous electrolytes, Al and Mg electrodeposition are impossible thermodynamically. In contrast, both Fe-air and Zn-air batteries can be rechargeable in aqueous environments. Hence, they offer potential advantages for widespread

application. As can be seen in Figure 2.1 Fe-air batteries have lower energy density than Zn-air batteries. As a result, Zn-air batteries attract great attention with their high theoretical energy densities (1086 W h kg^{-1}), high specific energy (1218 W h kg^{-1}), and a volumetric energy density of 6136 W h L^{-1} . Additionally, Zn metal is safe, abundant, and eco-friendly [48–52].

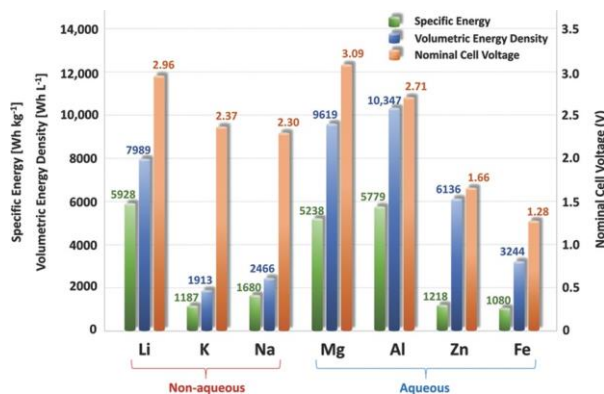


Figure 2.1 Comparison of different metal-air batteries in terms of specific energies, volumetric energy densities, and cell voltages [53].

2.2 Zinc-Air Batteries

Among the primary metal-air batteries Zn-air battery is highly favored because of its affordability and high capacity as mentioned before. The first primary Zn-air battery dates back to 1868 and it used an NH_4Cl aqueous solution as an electrolyte [54]. However, it faced challenges such as low working voltage and instability. Then in the 1930s, the electrolyte of the Zn-air battery is switched from neutral to alkaline media resulting in improved discharge performance [55]. Additionally, thanks to improvements in battery packaging technology, alkaline Zn-air batteries started to be used as power sources for hearing aids, railway signals, and other equipment. Since primary Zn-air batteries have an impressive volumetric energy density, they are widely used in hearing aids [53]. Over the last twenty years, the progress of materials and catalytic science has been stimulated by the improvements in nanotechnology. Consequently, the development of rechargeable Zn-air batteries is accelerated. Rechargeable Zn-air batteries especially for electric vehicles (EVs) were

extensively studied between the 1970s to 2000s with both mechanically and electrically rechargeable alternatives proposed [56,57]. In mechanical Zn-air batteries, the used zinc electrode is replaced physically as a result the battery can be recharged mechanically. However, mechanically rechargeable Zn-air batteries have challenges such as high setup costs. Therefore, electrically rechargeable Zn-air batteries are the most promising power source for EVs and portable electronic devices. In addition, they are generally considered one of the most economically viable battery solutions for grid-scale applications [49]. In rechargeable applications, the Zn electrode demonstrates low activity which provides stability in aqueous electrolytes. Hence, electrically rechargeable Zn-air batteries are promising for long-term cyclic operation. Nevertheless, rechargeable Zn-air batteries still face challenges such as low output power density, limited cycling stability, and poor discharge voltage plateaus which inhibit their large-scale commercial applications [43]. One significant obstacle affecting rechargeable Zn-air battery performance is the high overpotential on the air cathode, mainly due to the slow kinetics of oxygen reduction reaction (ORR) and oxygen evolution reactions (OER) [58,59]. Moreover, zinc anodes have problems like passivation, dendrite growth, and HER [60,61]. In addition, present rechargeable Zn-air batteries mainly work with liquid basic electrolytes that eventually cause leakage or volatilization [62–64]. Today, research efforts are mainly focused on material design for OER/ORR electrocatalysts and companies like EOS Energy Storage, Fluidic Energy, and ZincNyx Energy Solutions have already tried to develop innovative Zn-air systems [65].

2.2.1 Design and Working Principle of Rechargeable Zinc-Air Batteries

As can be seen from the schematic of a typical rechargeable Zn-air battery represented in Figure 2.2 the rechargeable Zn-air batteries generally contain four primary components: an air cathode which consists of a catalyst-coated gas diffusion layer (GDL), an alkaline electrolyte (commonly potassium hydroxide (KOH)), a separator, and a zinc anode.

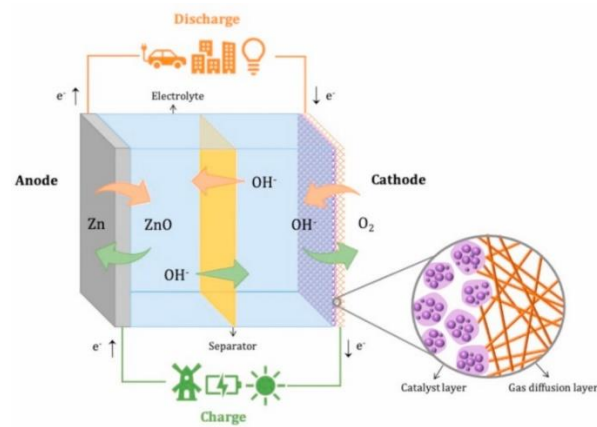
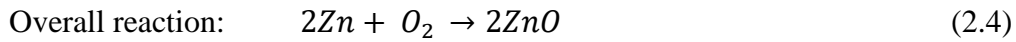
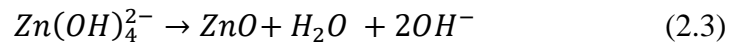
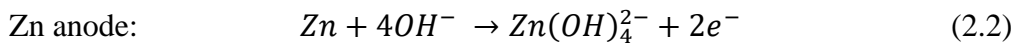
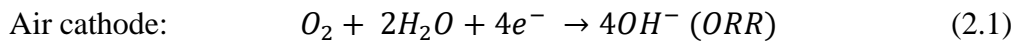


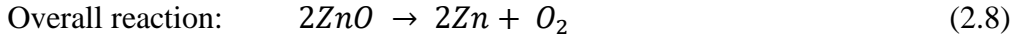
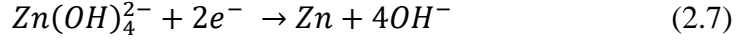
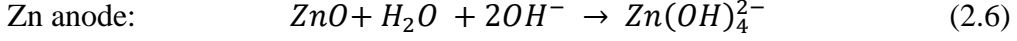
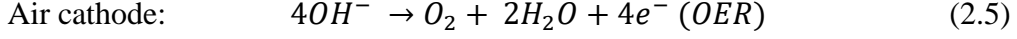
Figure 2.2 Schematic of a typical rechargeable Zn-air battery [49]

Rechargeable Zn-air battery reactions take place in the Zn anode and the air cathode during the discharge process are as follows:

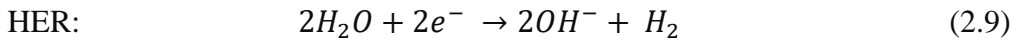


During discharge, the Zn-air battery acts as a power source by chemically coupling zinc metal with atmospheric oxygen (O_2) at the air cathode in the presence of an alkaline electrolyte. While zinc ions (Zn^{2+}) are produced at the zinc anode, electrons released from the zinc anode travel through an external circuit to the air cathode. Meanwhile, O_2 from the air diffuses into the porous air cathode and it experiences reduction to hydroxide ions (OH^-) by the ORR at a three-phase reaction site among the electrocatalyst (solid), electrolyte (liquid) and O_2 (gas). OH^- ions then move to the zinc anode, and with Zn^{2+} ions they form zincate ions ($Zn(OH)_4^{2-}$) together. When the concentration of $Zn(OH)_4^{2-}$ ions in the electrolyte becomes saturated, it decomposes into ZnO [66,67]. The insulating nature of ZnO hinders the Zn anode from efficiently releasing Zn^{2+} ions, potentially reducing effective contact at the electrolyte-Zn interface and subsequently decreasing the cell's overall efficiency. [68].

For the charging process reactions take place at the Zn anode and the air cathode in the rechargeable Zn-air battery are as follows:



During charging, the Zn-air battery stores electrical energy with OER at the electrode-electrolyte interface while ZnO reduces back to Zn. The Zn^{+2} ions in the electrolyte are reduced to form metallic Zn, which is then deposited onto the surface of the Zn anode. Simultaneously, OH^- ions are oxidized to produce O_2 at the air cathode. During charging Zn can deposit on the Zn anode non-uniformly due to uneven distribution of current densities. As a result, significant shape changes may occur on the anode surface. This uneven deposition can create sharp, needle-like structures called dendrites. These dendrites may separate from the anode, decrease the battery capacity, or break the separator and cause short circuits [69]. In addition, during battery charging, the hydrogen evolution reaction (HER) creates another barrier to Zn-air battery performance. As illustrated in reaction 2.9 HER competes with the anode for electrons, thus reducing the energy efficiency of the charging process [70].



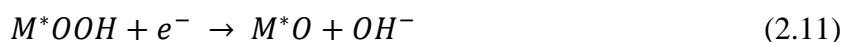
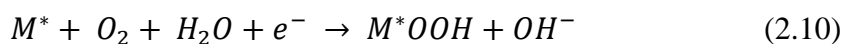
More importantly, the battery efficiency is significantly affected by the sluggish redox pathways at the air cathode. The four-electron oxygen chemistry depicted in reaction 2.5 is remarkably slow because of the strong oxygen bonds, resulting in elevated overpotentials in the OER/ORR. Electrocatalysts are commonly utilized to accelerate the OER/ORR. However, finding a catalyst that promotes both redox reactions at the air cathode is challenging, thus it limits the power density of Zn-air batteries. Although developing bifunctional oxygen electrocatalysts to accelerate

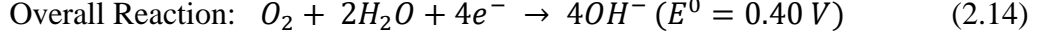
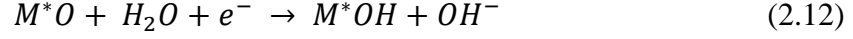
OER/ORR is investigated by the researchers vastly, the current achievable discharge voltages of Zn-air batteries remain below the theoretical voltage of 1.65 V under standard conditions. Additionally, a recharge voltage of 2 V or higher is typically needed to reverse the reactions [66]. The significant difference from the equilibrium value primarily occurs because of the overpotentials of the OER/ORR at the air cathode [71,72]. In addition, the difference may be attributed to activation loss and dendritic formation in the air cathode and zinc anode, respectively [73].

2.2.2 Oxygen Reduction and Oxygen Evolution Reactions

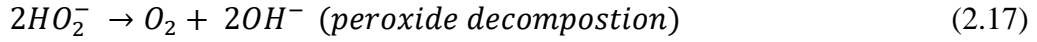
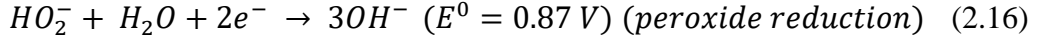
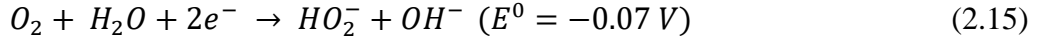
As mentioned in Section 2.2.1, the fundamental electrochemical reactions that take place at the air cathode are the ORR and OER during the discharge and charge of the Zn-air battery, respectively. During the discharge of Zn-air batteries, the air cathode continuously takes oxygen from the surrounding air for oxygen reduction. The ORR typically follows two primary pathways in alkaline electrolytes. It can proceed by four electron ($4e^-$) or two electron pathways ($2e^-$) [74]. The ORR pathway is influenced by the configurations of oxygen adsorption on the active sites of the catalyst. Two types of oxygen adsorption are observed for ORR which are side-on O_2 adsorption, where both oxygen atoms are coordinated to the catalyst, and end-on O_2 adsorption, where only one oxygen atom is coordinated to the catalyst. Side-on bidentate adsorption promotes the direct $4e^-$ pathway, while end-on coordination favors the $2e^-$ pathway with intermediate peroxide formation [75–77].

In the $4e^-$ pathway, firstly, a bidentate oxygen molecule adsorbs onto the active site of the catalyst surface (M^*). Then, electrons are transferred from the anode to the adsorbed oxygen molecule and the $O=O$ bond weakens and breaks, leading to the generation of OH^- ions. The $4e^-$ pathway of ORR is as follows:





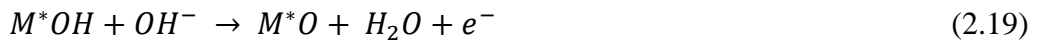
In the $2e^-$ pathway for ORR, a catalyst coordinated with only one oxygen atom and peroxide species is produced. Then, OH^- is formed through the reduction of peroxide (Reaction 2.16) or decomposition of peroxide (Reaction 2.17). The pathway involving reactions 2.15 and 2.16 or 2.17 is termed a serial $2 \times 2e^-$ pathway. ORR with $2e^-$ pathway is as follows:

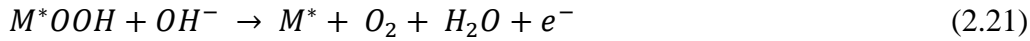


Peroxide species generated during the $2e^-$ pathway are corrosive and detrimental to Zn-air battery stability. Therefore, in practical rechargeable Zn-air battery applications, catalysts that facilitate ORR with a direct four-electron reduction pathway are strongly favored [78].

During the charging of Zn-air batteries, the electrochemical reactions that take place in the air cathode in ORR are reversed, resulting in oxygen evolution at the air cathode. Like ORR, OER involves multiple electron transfers. OER can occur with two different pathways which are adsorbed evolution mechanism (AEM) and lattice-oxygen mediated mechanism (LOM) [79].

AEM is extensively studied in alkaline electrolytes and it involves the adsorption of OH^- on an oxide surface, coordinating with an active metal site (M^*) of catalyst to form the M^*OH . M^*OH group then reacts with OH^- , leading to the formation of intermediates M^*O and M^*OOH . Eventually, O_2 is released [80]. The steps of the AEM pathway for OER are as follows:





The LOM pathway is different from the traditional AEM pathway since it avoids the proton-electron transfer steps. Instead, it directly links to the O–O bond to produce oxygen without the formation of M*OOH intermediates [81]. The reactions for the LOM pathway for OER are as follows:



The overpotential needed for oxygen evolution depends on the kinetic barriers related to each step. Typically, the thermodynamic barrier of reaction 2.24 is higher than the reactions 2.20 and 2.21. Therefore, the AEM pathway is thermodynamically more advantageous. However, the reaction pathway and the step that determines the rate of OER depend on the catalytic material and the conditions of the OER reaction. The equilibrium potential of ORR and OER is 1.23 V vs. the reversible hydrogen electrode (RHE) [82]. However, significant overpotentials are required to facilitate these reactions because of the complicated mechanisms and slow kinetics of the 4e⁻ pathways. High overpotentials in ORR and OER reduce the overall energy efficiency of rechargeable Zn-air batteries. Therefore, efficient bifunctional electrocatalysts for OER/ORR with low overpotentials must be used in the air cathode.

2.3 Components of Rechargeable Zinc-Air Batteries

As discussed in Section 2.2.1 main components of rechargeable Zn-air batteries are Zn-anode, electrolyte, separator, and catalysts coated GDL which creates the air cathode. In this section, the main components of the rechargeable Zn-air batteries will be detailed in terms of the materials used, the challenges encountered, and the latest advancements.

2.3.1 Zinc Anode

An effective zinc anode needs to have a significant amount of active material, it should facilitate efficient recharging, and maintain its capacity over a long time and many charge-discharge cycles. The Pourbaix diagram in Figure 2.3 demonstrates the regions of corrosion, passivation, and stability for Zn within the electrolyte [83]. The unstable transition between Zn and ZnO creates problems such as corrosion, dendrite formation, and HER as mentioned before. Therefore, the performance and long-term stability of the Zn anode is mainly limited [84].

The shape, structure, and surface characteristics of Zn play a crucial role to determine the performance of Zn-air batteries [85–88]. These factors affect interparticle connections, internal electrical resistance, and overall electrochemical behavior. The surface structure of Zn is important for improving reaction rates in an alkaline electrolyte. Apart from traditional bulk Zn, different forms of Zn anode materials such as powders, flakes, and fibers with larger surface areas have been investigated [89,90]. A higher surface area is suitable for applications which require high discharge currents. In addition, Zn anodes with three-dimensional (3D) porous structures to increase surface area and prevent dendrite formation by creating direct contact with the electrolyte have been used recently in rechargeable Zn-air batteries. However, a higher surface area may increase the corrosion rate, which decreases the lifespan of the battery and reduces zinc efficiency [91].

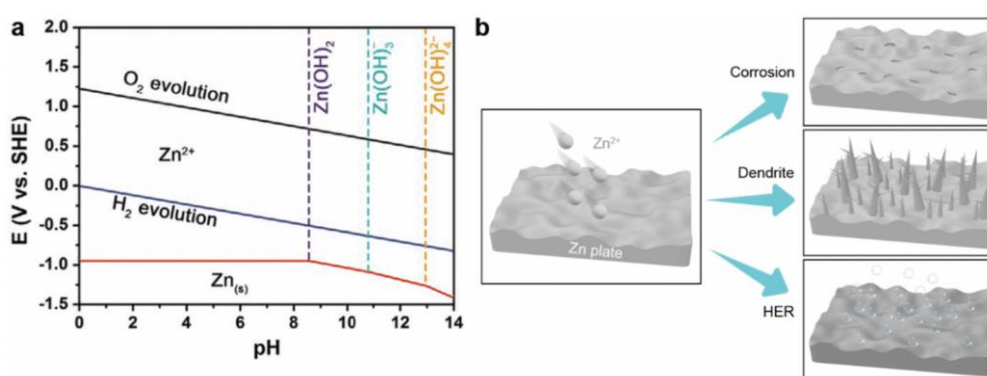


Figure 2.3 (a) Pourbaix diagram of oxygen and zinc (b) Schematic illustration of corrosion, dendrite growth, and HEO on Zn [40]

Alloying Zn with other metals like lead (Pb), cadmium (Cd), bismuth (Bi), tin (Sn), and indium (In) has been shown to improve the stability of the Zn anode [92–94]. Additionally, using additives such as silicates, surfactants, and polymers can modify Zn's electrochemical properties and reduce hydrogen gas production [95,96]. Moreover, applying coatings onto Zn metal is an effective method to enhance the overall performance of the Zn anode. Organic anode coatings are advantages since they are cost-effective, easy to fabricate, environmentally friendly, and controllable as compared to inorganic coatings. Many research has focused on organic additives such as polyvinyl alcohol (PVA), polyacrylonitrile (PAN), and polyaniline (PANI) hydrogels to mitigate the self-discharge and corrosion issues in Zn-air batteries [97,98].

2.3.2 Electrolyte

Efficient electrolyte must have high conductivity and low viscosity. Currently, in rechargeable Zn-air batteries, alkaline electrolytes such as KOH, NaOH, LiOH, and neutral NH_4Cl electrolytes are commonly used. While near-neutral chloride electrolytes are safer and more resilient options as compared to traditional ones, KOH is the primary choice in Zn-air batteries. This is due to KOH's superior ionic conductivity, higher oxygen diffusion coefficient, and lower viscosity [99]. Additionally, the side reaction products of KOH with CO_2 are more soluble than their sodium counterparts. Therefore, KOH may potentially address the carbonate precipitation issue in Zn-air batteries. In addition, one method to decrease the electrolyte resistance is to raise the concentration of KOH. However, this can increase the electrolyte viscosity [100]. Moreover, higher KOH concentrations may promote ZnO formation which indirectly raises the viscosity and potentially cause dendrite formation. Therefore, 6 M KOH is commonly used for its sufficient viscosity and ionic conductivity [101].

There are mainly two major problems related to the electrolyte because of Zn-air batteries' open system. Firstly, carbonate precipitation occurs due to atmospheric

CO₂. The alkaline solution reacts with hydroxyl ions, and they can form carbonate (CO₃²⁻ or HCO₃⁻²) which in turn reduces OH⁻ concentration and thus electrolyte conductivity. Moreover, carbonate crystal formation can block the porous air electrode. Hence, it leads to a decrease in cell capacity and reduces the lifetime of the battery [102,103]. Secondly, water leakage may occur in the Zn-air battery. Air cathode can indirectly allow water to escape into the environment as a gas. Gelling the electrolyte is a potential solution to minimize water loss and, therefore; improve battery performance.

2.3.3 Air Cathode and Bifunctional Electrocatalysts for OER and ORR

A bifunctional air cathode consumes oxygen during discharge and produces oxygen during charging as mentioned in Section 2.2. Electrically rechargeable Zn-air batteries depend heavily on air cathode, which should be bifunctionally active and durable to achieve high power performance. Air cathodes must tolerate the harsh conditions of repetitive discharge and charge cycles in alkaline electrolytes. Both the ORR and OER take place in an air cathode and exhibit significantly high overpotentials, therefore; developing a bifunctionally active air cathode is challenging. A bifunctional electrocatalyst is required to accelerate both processes (OER/ORR) efficiently. Additionally, the cathode materials must be stable in highly oxidative (OER) and strongly reducing (ORR) conditions at high potentials. The working potential range changes from ≈ 0.6 V (vs. RHE at pH = 14) during discharge to ≈ 2.0 V (vs. RHE) during charge for rechargeable Zn-air batteries.

In general, the bifunctional air cathode consists of a hydrophobic gas diffusion layer (GDL) and a relatively hydrophilic catalyst layer. The GDL offers both physical support and electrical conductivity for the catalysts, and it allows oxygen diffusion during the discharge and charge of the Zn-air battery. In addition, the GDL acts as a wet-proofing electrode backing to prevent electrolyte leakage, and it provides high electrical conductivity for efficient current collection. Hence, GDL should be thin, hydrophobic, and highly porous. This hydrophobicity can be achieved by

impregnating the GDL with hydrophobic agents such as PVDF, PTFE, and fluorinated ethylene propylene (FEP) [104–106]. The hydrophobicity of GDL affects battery polarization behavior, including electrical conductivity (Ohmic resistance) and gas permeability (mass transfer). To optimize Zn-air battery performance, the GDL should inhibit electrolyte evaporation and resist electrolyte flooding under extreme conditions [107]. Additionally, an ideal GDL should facilitate fast air diffusion, maintain its mechanical integrity, exhibit superior electrical conductivity, and present chemical durability in strong alkaline electrolytes. Currently, two types of carbon-based GDLs are commercially available, and they are used in Zn-air batteries generally. They are nonwoven carbon paper (e.g., Toray, Freudenberg, and Sigracet) and woven carbon cloth (e.g., Zoltek, GDL-CT, and ELATTM). As illustrated in Figure 2.4 these carbon-based GDLs typically have a double-layer structure, consisting of a macroporous gas-diffusion backing layer and a thin microporous layer (MPL). The macroporous backing layer is made up of highly hydrophobic graphitized carbon fibers that create large gas-diffusion pores. In contrast, the MPL is a thin, relatively hydrophilic carbon layer, such as carbon black, with fine porosity. This MPL supports the catalytic active materials, efficiently distributes air across the catalyst layer, and reduces contact resistance between the macroporous layer and the catalyst layer. [108].

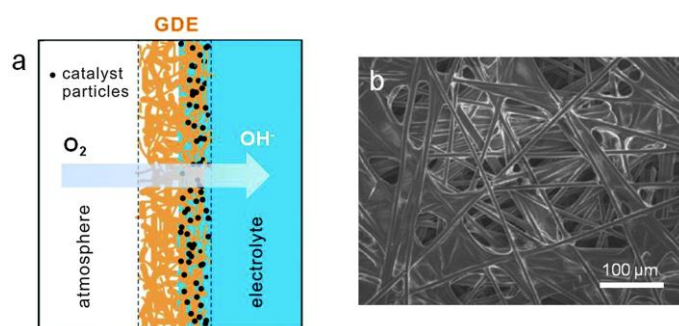


Figure 2.4 (a) Schematic illustration of the catalyst-loaded gas diffusion electrode (GDE) in contact with the liquid electrolyte, designed to facilitate the easy permeation of oxygen from the surrounding atmosphere and its reduction on supported electrocatalysts (b) SEM image of commercial Toray carbon paper treated with hydrophobic PTFE [66].

As mentioned in Section 2.2. the ORR occurs at a three-phase interface which consists of a gaseous oxygen, liquid electrolyte, and solid catalyst, while the OER occurs at a two-phase liquid (electrolyte) and solid (catalyst) interface. As a result, an interface with a high surface area between the three phases is crucial for highly active and efficient air cathodes. Hence, to enhance the catalytic activity and prevent flooding of the catalytic sites, an air cathode with an optimal interfacial structure and hydrophilicity should be designed. The air cathode must facilitate oxygen diffusion while preventing leakage of the electrolyte.

Moreover, the catalytic active layer on the air cathode, where ORR and OER take place, consists of a bifunctional electrocatalyst, carbon materials, and a binder. The bifunctional catalyst is crucial for the performance of the air cathode. As detailed in Section 2.2.2 both ORR and OER involve four fundamental steps. ORR starts with the formation of M^*OOH from adsorbed O_2 on the metal active catalyst site, followed by its reduction to M^*O and M^*OH . OER proceeds in the reverse direction. These reactions have slow kinetics. They require an active bifunctional oxygen electrocatalyst to minimize the required overpotentials [109,110]. Hence, it is important to develop new bifunctional catalysts that are efficient, cost-effective, and environmentally friendly. Recent research efforts in rechargeable Zn-air batteries have primarily aimed to improve the materials and structural design of bifunctional oxygen electrocatalysts. Researchers try to enhance the electrochemical reaction kinetics at the air cathode while increasing the endurance of the bifunctional electrocatalysts during the cyclic operation of Zn-air batteries. Various materials, such as metal oxides, metal hydroxides, metal sulfides, carbon materials, and their composites, have been extensively investigated as potential bifunctional oxygen electrocatalysts [111,112]. However, the lack of cheap, stable, and efficient bifunctional OER/ORR catalysts still inhibits the commercialization of rechargeable Zn-air batteries. Therefore, this thesis mainly focusses on designing effective, and stable bifunctional oxygen catalysts for rechargeable Zn-air batteries that work in alkaline environments. As a result, in the next sections, bifunctional electrocatalysts

that are used commercially and presented in the literature for Zn-air batteries were deeply explained.

2.3.3.1 Platinum Group Metals (PGMs) and Their Alloys

The most efficient oxygen electrocatalysts which are developed and used commercially in the Zn-air batteries are rare and expensive platinum group metals (PGMs) such as platinum (Pt), palladium (Pd), iridium oxide (IrO_2), and ruthenium oxide (RuO_2). RuO_2 , IrO_2 , and Pt are still the benchmark catalysts for estimating new bifunctional oxygen electrocatalyst materials. However, the large-scale application of PGMs in Zn-air batteries is limited by their high costs and scarcity. Additionally, rechargeable Zn-air batteries necessitate bifunctional catalysts capable of simultaneously catalyzing both the ORR during discharge and the OER during charging as mentioned before in the previous sections of this thesis. However, in general, PGMs exhibit poor bifunctional activities. For example, although Pt shows excellent ORR performance, it exhibits low OER performance due to the formation of a low-conductive oxide layer on its surface at OER working potential [113]. On the other hand, noble-metal oxides like IrO_2 or RuO_2 are excellent OER catalysts, but they exhibit lower activity for the ORR [114,115]. This typically requires using a combination of two different PGMs to achieve bifunctionality, which can impact the overall electrocatalytic performance. For instance, Pt catalysts supported on high surface area carbon (Pt/C) are often mixed with OER catalysts like RuO_2 or IrO_2 and used as standard air cathodes for Zn-air batteries. This approach necessitates a higher PGM loading to compensate for the activity loss in these mixed catalysts, thus increasing the cost of Zn-air batteries. The scarcity and high cost of PGMs have motivated researchers to develop methods to enhance their activity and stability while reducing the required amount. These strategies include minimizing Pt dimensions to the nano or atomic scale, modifying Pt's morphology and crystal facets, and alloying Pt with more affordable noble metals such as Pd, heavy metals like Pb, and transition metals including Fe, Ni, Co, Mo, and Cu. [116,117]. However,

despite these efforts, the high cost and scarcity of PGMs severely affect the mass-production of rechargeable Zn-air batteries. Therefore, it is important to decrease PGM usage and develop earth-abundant non-precious materials as bifunctional electrocatalysts for rechargeable Zn-air battery applications.

2.3.3.2 High Entropy Oxides

In 2015, Rost et al. made a noteworthy improve in materials science by introducing High Entropy Oxides (HEOs), a new class of materials that is thermodynamically similar to High Entropy Alloys (HEA) [118]. Since then, HEOs have attracted significant research interest, leading to the development of various compositions, crystal structures, microstructures, and, most notably, customizable properties (Figure 2.5). HEAs are produced by combining five or more elements in equal or nearly equal atomic ratios. Thanks to the high entropy effect in thermodynamics, lattice distortion in structure, delayed diffusion in kinetics, and the cocktail effect in performance, these alloys can easily form solid solution phases, nanostructures, and even amorphous structures with high thermal stability. Hence, HEAs can have superior strength, exceptional wear resistance, and excellent corrosion resistance.

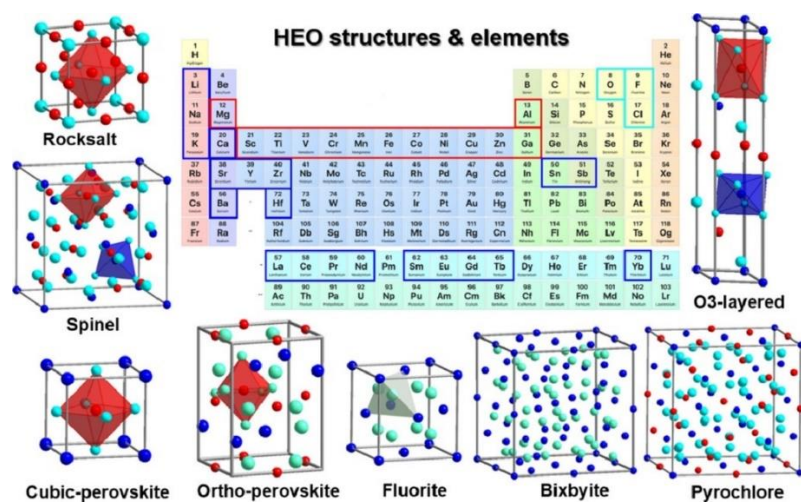


Figure 2.5 Different crystal structures, and elements for HEOs that is researched in the electrochemical applications [119]

HEAs exhibit exceptional physicochemical properties and outstanding structural stability which makes them ideal for electrocatalysis due to the high-entropy stabilization and synergy between various metallic components. Interestingly, the concept of utilizing high configurational entropy to achieve desired catalytic properties has been extended to other material systems, including (oxy)hydroxides, oxides, intermetallics, halides, carbides, nitrides, sulfides, phosphides, and metal-organic frameworks (MOFs). The compositional flexibility of high-entropy materials allows tuning of electrocatalytic activity, while high-entropy mixing ensures structural stability under operational conditions. Consequently, high-entropy materials offer new and exciting opportunities in the development of advanced water-splitting electrocatalysts [120–122].

Unlike HEAs which primarily exhibit single-site occupancies in a face-centered cubic crystal structure, HEOs have independent cation and anion sublattices, leading to greater structural diversity. This structural complexity, combined with the expanded tuning range in both composition and structure, has shifted the focus toward understanding the increased entropic effects on the oxygen component, particularly the activation of lattice oxygen. The capability to create and manipulate oxygen defects within various HEO structures is especially beneficial for enhancing the catalytic activity in a range of oxidation reactions. As a result, HEOs have recently become significant in electrochemical applications. Especially, HEOs containing 3d metals like Fe, Cu, Co, Ni, Mn, Zn, and Cr have shown remarkable electrocatalytic activity for OER and ORR. This enhanced performance is due to their capability to adjust the electronic structure. [123–125]. For instance, Zhang et al. synthesized $(\text{CoNiMnZnFe})_3\text{O}_{3.2}$, which exhibits a 336 mV overpotential and a Tafel slope of 47.5 mV dec^{-1} [126]. Duan et al. synthesized a spinel-structured OER catalyst, $(\text{FeCoNiCrMn})_3\text{O}_4$, which shows a low overpotential of 288 mV [127].

2.3.3.3 Perovskite Oxides

Replacing noble-metal catalysts with first-row transition metal containing perovskite oxides has gathered interest due to their low cost, simple production methods, and high structural and compositional flexibility, which enhance their catalytic activity. Perovskite oxides have the general formula ABO_3 , where A and B are large electropositive cations. They have the structure shown in the center of Figure 2.6. In perovskite-type oxides, cations in the A-site are usually rare-earth or alkaline earth metals (such as Sm, La, Sr) with 12-fold oxygen coordination, while B-site cations are composed of transition metals (such as Fe, Co, Mn, Ni) with 6-fold oxygen coordination. The ideal perovskite oxide, ABO_3 , has a cubic crystal structure with high $Pm\bar{3}m$ symmetry. This structure features a flexible framework composed of chains of corner-sharing $[BO_6]$ octahedra, with A cations filling the resulting cuboctahedral holes. Corner-sharing $[BO_6]$ octahedral building blocks are the primary OER active sites in noble metal-free perovskites. Octahedral sites allow modification of both oxygen anions and B-site metal cations. By doping multiple cations at the A and/or B sites, the electronic structure can be manipulated to enhance electrocatalytic activity. In addition, double perovskite oxides ($A_2BB'O_{5+\delta}$) demonstrate enhanced stability and superior electrocatalytic performance compared to single perovskite oxides [128,129]. These compounds have two octahedral sites, BO_6 and $B'O_6$, consisting of alternating pairs of B and B' atoms bound to oxygen. The arrangement of cations within the B-site and the oxidation state of the transition metal are key factors influencing the electrocatalytic efficiency of double perovskite oxide catalysts [130]. The metal-oxygen covalency, involving the hybridization of metal M 3d and oxygen O 2p orbitals, significantly effects their electrocatalytic performance [131–135]. Additionally, a perovskite oxide structure with a network of oxygen vacancies can enhance oxygen ion transport and conductivity, thereby improving the kinetics of both OER and ORR [29,31,38]. Thus, different strategies have been utilized to modify the surface electronic structure and increase the number of active sites for electrochemical reactions. [136,137]. A simple and fast method to

adjust the electronic characteristics of perovskite oxides is doping [128,138–141]. For example, doping divalent Sr^{2+} cations into LaCoO_3 at the A-site significantly enhances its electrocatalytic activity by increasing oxygen vacancies and promoting higher oxidation states of B-site Co cations, thereby improving Co 3d-O 2p hybridization [142]. Similarly, doping Co into $\text{LaMn}_{1-x}\text{Co}_x\text{O}_3$ at the B-site enhances OER performance by facilitating the conversion of OOH^- to O_2 by mixed $\text{Mn}^{4+}/\text{Mn}^{3+}$ oxidation states [143]. In another study, Kim et al. reported that doping transition-metal oxides such as Fe^{2+} , Ni^{2+} , Cu^{2+} , and Mn^{2+} into the B-sites of the $\text{NdBa}_{0.75}\text{Ca}_{0.25}\text{Co}_2\text{O}_{5+\delta}$ catalyst enhances electron and oxygen-ion mobility by promoting the formation of oxygen vacancies in double perovskite oxides [144]. Moreover, many research suggests that doping both A and B-sites can improve bifunctional activity. For instance, perovskite oxides with Ba and Sr at the A-site demonstrate fast ion transport kinetics, whereas those with increased Co content at the B-site show higher kinetic coefficients as compared to compositions with a higher Fe content. [145]. Merkle et al. reported that incorporating cobalt into $\text{Ba}_{0.5}\text{Sr}_{0.5}\text{Co}_{1-y}\text{Fe}_y\text{O}_{3-y}$ reduces the energy required for O-vacancy formation due to the proximity of the electronic states' density to the Fermi level, making it easier to reduce Co^{4+} to Co^{3+} compared to Fe^{4+} to Fe^{3+} [146].

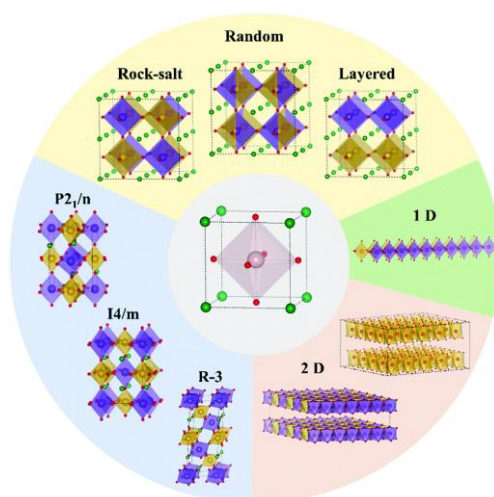


Figure 2.6 Center shows the crystal structure of a cubic perovskite oxide while in the outer circle double perovskite oxides with different crystal structure such as rock-salt, layered etc. are presented.

CHAPTER 3

EXPERIMENTAL PROCEDURE

3.1 Synthesis of $(\text{FeCrCoMnZn})_3\text{O}_{4-\delta}$ Powders in Vacuum and Air Atmosphere

The co-precipitation method was employed to fabricate powders of $(\text{FeCrCoMnZn})_3\text{O}_{4-\delta}$ HEO. Firstly, metal nitrate salts including $\text{FeSO}_4 \cdot 7\text{H}_2\text{O}$ (99.5% purity), $\text{MnSO}_4 \cdot \text{H}_2\text{O}$ (99% purity), $\text{Cr}(\text{NO}_3)_3 \cdot 9\text{H}_2\text{O}$ (99% purity), $\text{CoSO}_4 \cdot 7\text{H}_2\text{O}$ (99% purity), and $\text{Zn}(\text{NO}_3)_2 \cdot 6\text{H}_2\text{O}$ (98% purity) were combined in stoichiometric ratios and dissolved in deionized water ($18.2 \text{ M}\Omega \cdot \text{cm}$). The mixture was gently stirred on a magnetic stirrer to form a 1 M metal-salt solution. Then, a 1 M aqueous potassium hydroxide (KOH) solution which acts as a precipitating agent was slowly added to the metal-salt solution until the pH reached 12.0. Following the precipitation, the resulting powders were filtered and dried in an oven at 110°C for 8 hours. To examine the impact of the synthesis environment on the electrocatalytic activity for water splitting reactions, the powders were subjected to calcination in vacuum and air atmospheres independently at 900°C for 60 minutes. In this study, the $(\text{FeCrCoMnZn})_3\text{O}_{4-\delta}$ synthesized in vacuum and air conditions are denoted as HEO-Vac and HEO-Air, respectively. The experimental procedure to synthesize HEO-Vac powders was shown schematically in Figure 3.1.

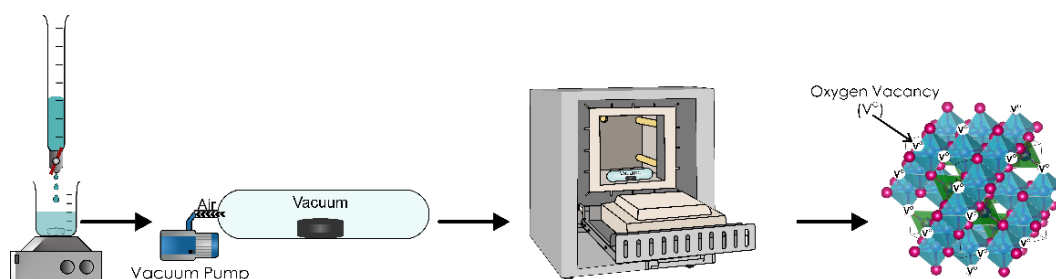


Figure 3.1 Schematic illustrating the sequential procedures in the synthesis of $(\text{FeCrCoMnZn})_3\text{O}_{4-\delta}$ HEO under vacuum conditions.

3.2 Synthesis of Nanoporous (FeCrCoMnZn)₃O_{4-δ} Powders

Nanoporous (FeCrCoMnZn)₃O_{4-δ} powders were synthesized with low-temperature sol-gel method. Metal nitrate salts including FeSO₄·7H₂O (99.5% purity), MnSO₄·H₂O (99% purity), Cr(NO₃)₃·9H₂O (99% purity), CoSO₄·7H₂O (99% purity), and Zn(NO₃)₂·6H₂O (98% purity) were mixed in stoichiometric ratios and dissolved in deionized water (18.2 MΩ·cm). Glycine was then added to the deionized water as a chelator and fuel agent, allowing the metal nitrate mixture to hydrolyze in the liquid phase. After the drying and aging process at approximately 90°C, the sol gradually polymerized to form a gel with a three-dimensional network structure. Finally, nanometer-scale porous HEO materials were produced through a calcination process. To understand the effect of pore size on the electrocatalytic activity, and rechargeable Zn-air battery performance calcination is applied at 500 °C, 600 °C, and 700 °C for 1 hour. In this thesis, (FeCrCoMnZn)₃O_{4-δ} powders calcined at 500 °C, 600 °C, and 700 °C are denoted as GLY500, GLY600, and GLY700, respectively. The experimental procedure to synthesize nanoporous GLY500, GLY600, and GLY700 powders was shown schematically in Figure 3.2.

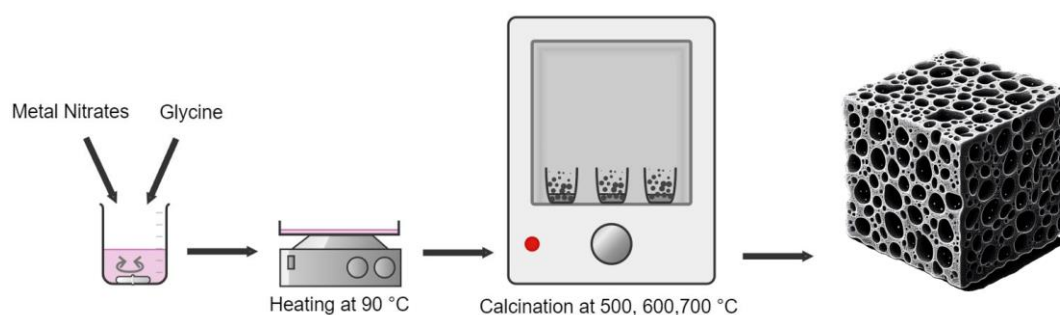


Figure 3.2 Schematic illustrating the sequential procedures in the synthesis of GLY500, GLY600, and GLY700 nanoporous HEOs

3.3 Synthesis of $\text{NdBaCo}_a\text{Fe}_{2-a}\text{O}_{5+\delta}$ ($a= 1.0, 1.4, 1.6, 1.8$) Powders

The $\text{NdBaCo}_a\text{Fe}_{2-a}\text{O}_{5+\delta}$ ($a= 1.0, 1.4, 1.6,$ and 1.8) double perovskite oxides which are designated as NBCF were synthesized with modified sol-gel Pechini method. In this process, firstly, stoichiometric amounts of metal-nitrate salts, $\text{Nd}(\text{NO}_3)_3 \cdot 6\text{H}_2\text{O}$ (Sigma Aldrich), $\text{Ba}(\text{NO}_3)_2$ (Alfa Aesar 99%), $\text{Co}(\text{NO}_3)_2 \cdot 6\text{H}_2\text{O}$ (Alfa Aesar 98.9-102.0%), and $\text{Fe}_3(\text{NO}_3)_9 \cdot 9\text{H}_2\text{O}$ (Sigma Aldrich) were dissolved in ultrapure water ($18.2 \text{ M}\Omega\cdot\text{cm}$) and stirred on a hot plate at 100°C . As chelating agents, citric acid (CA) and acrylamide (AC) were then added to the metal-nitrate salt solution. After evaporation of physically bonded water, the resulting gel was dried at 225°C for approximately 24 hours. Then, the calcination process was applied to the powders at 600°C for 15 hours to eliminate compounds such as CO , CO_2 , and NO_2 . Finally, the calcined powders were annealed at 1300°C to achieve a single-phase double perovskite oxide. The experimental procedure to synthesize NBCF double perovskite oxide powders was shown schematically in Figure 3.3.

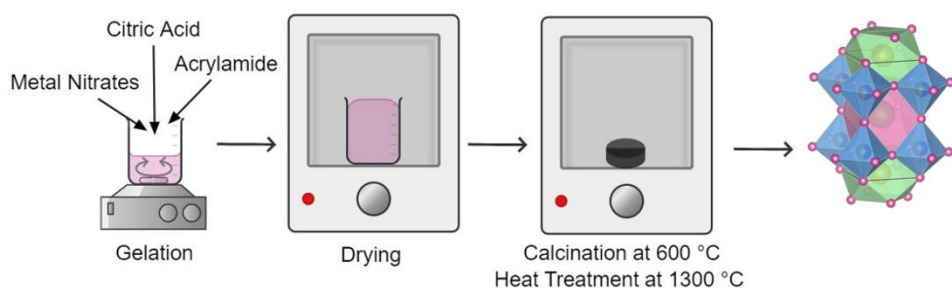


Figure 3.3 Schematic illustrating the sequential procedures in the synthesis of NBCF double perovskite oxides.

3.4 Materials Characterization

The X-ray diffraction (XRD) method was used to explore the crystal structure of synthesized powders. XRD experiments were performed using Ni-filtered $\text{Cu K}\alpha$ radiation ($\lambda = 1.5406 \text{ \AA}$) within a 2θ range of 10° to 80° . The measurements were conducted with a Rigaku DMAX2200 diffractometer operating at 40 kV and 30 mA,

equipped with an Ultima+ theta-theta high-resolution goniometer in Bragg-Brentano geometry. The acquired XRD patterns were refined using the Rietveld Refinement Method with the help of GSAS software and the EXPGUI interface.

The microstructure and morphology of the HEO-Air, HEO-Vac, GLY500, GLY600, and GLY700 powders were examined using a field emission high-resolution transmission electron microscope, JEOL JEM 2100F 200kV. By HRTEM, bright field (BF), high angle annular dark field (HAADF), HRTEM image, and selected area electron diffraction (SAED) patterns were acquired. Moreover, energy dispersive spectroscopy (EDS) elemental mappings of HEO-Air and HEO-Vac were obtained with HRTEM. In addition, to examine the structure and surface characteristics of the synthesized NBCF and nanoporous HEO powders, a scanning electron microscope (SEM), FEI Nova Nano SEM 430, was employed.

The specific surface areas of HEO-Air and HEO-Vac powders were determined using the Brunauer-Emmet-Teller (BET) method across a relative pressure range of $P/P_0 = 0.055-0.30$. Nitrogen (N_2) adsorption-desorption isotherms, achieved by using a Quantachrome Corporation Autosorb-6 instrument, were employed for specific surface area calculations. Before BET analysis, the powders experienced degassing at 300°C for 2 hours under vacuum.

To analyze the electronic characteristics of HEO-Air, HEO-Vac, nanoporous HEO, and NBCF powders, X-ray photoelectron spectroscopy (XPS) was conducted using a PHI 5000 Versa Probe spectrometer with Al K_α radiation. XPS was utilized a standard carbon 1s spectrum at 284.6 eV which serves for peak calibration. To prevent localized charge accumulation during XPS analysis that uses 5 eV electrons and low-energy argon ions, the PHI 5000 charge compensation system was applied. XPS spectra were processed using Avantage software, employing a peak-fitting technique with a Shirley background and symmetrical mixed Gaussian-Lorentzian peak forms within the 70% to 30% range. Additionally, electron paramagnetic resonance spectroscopy (EPR) was conducted using a Bruker ELEXSYS E580 instrument to investigate the oxygen vacancy content of HEO-Air and HEO-Vac

powders. Moreover, Ultraviolet photoelectron spectroscopy (UPS) experiments were conducted on NBCF double perovskite oxide electrocatalysts using the Physical Electronics (PHI), Versa Probe 5000 instrument under high vacuum conditions with a base pressure of 1×10^{-9} mbar. UV light for UPS measurements was provided by a He gas discharge lamp with an energy of 21.22 eV.

3.5 Electrochemical Characterization

The electrochemical performance of synthesized powders was assessed using a Rotating Disc Electrode (RDE) setup from BASI, coupled with a GAMRY Reference 3000 potentiostat/galvanostat/ZRA. A standard three-electrode configuration was used, which has a Pt wire as the counter electrode, Ag/AgCl as the reference electrode, and a glassy carbon electrode (GCE) as the working electrode throughout the experiments. An electrolyte consisting of a 0.1M potassium hydroxide solution, prepared using deionized water and KOH (Alfa, 99.99%), was utilized, during all the experiments unless otherwise specified.

Initially, catalyst inks for HEO-Air, HEO-Vac, GLY500, GLY600, GLY700, and NBCF double perovskite oxide powders were individually prepared, each comprising 8 mg of synthesized powder, 5 mg Super-P carbon, 50 μ L Nafion solution (Sigma-Aldrich, 5 wt %), and 1.8 mL ethanol. Following ultrasonic mixing of the ink components, 10 μ L of the catalyst ink was drop cast onto a GCE and air-dried, resulting in a mass loading of $0.15 \text{ mg}_{\text{powder}} \text{ cm}_{\text{disk}}^{-2}$, thus preparing the working electrode. Before all experiments, the KOH electrolyte was oxygen-saturated for approximately 30 minutes. Additionally, to maintain the $\text{O}_2/\text{H}_2\text{O}$ equilibrium at 1.23 V, oxygen gas was supplied continuously to the system throughout the experiments. Furthermore, unless otherwise specified the rotation speed of the RDE was maintained at 1600 rpm for conducted experiments.

To understand the OER activity of electrocatalysts, surface activation of HEO-Air, HEO-Vac, nanoporous HEOs, and NBCF electrocatalysts was conducted through 10

cycles of cyclic voltammetry (CV) tests at a scan rate of 100 mV s^{-1} , spanning from 0.2 to 1.1 Volt vs. Ag/AgCl. After obtaining reproducible CV data, an assessment of the electrocatalytic performance of synthesized powders was carried out using linear sweep voltammetry (LSV) within the range of 0.2 to 1.1 V vs. Ag/AgCl, employing a scan rate of 10 mV s^{-1} . All the recorded potentials vs. Ag/AgCl were subsequently normalized to the reversible hydrogen electrode (RHE) based on the Nernst equation.

For Tafel analysis under steady-state conditions, chronoamperometry (CA) tests were applied to all of the electrocatalysts within a potential range of 0.40 to 0.65 V vs. Ag/AgCl, with increments of 0.01 V.

Electrochemical impedance spectroscopy (EIS) was conducted using an alternating current (AC) voltage with an amplitude of 10 mV over a frequency range of 10^5 to 10^{-2} Hz. The EIS measurements were recorded at a potential of 1.641 V vs. the RHE.

The electrochemically active surface area (ECSA) was assessed by measuring the double-layer capacitance (C_{dl}). This was derived from CV measurements performed at varying scan rates in the non-faradaic region. [6,147]. CVs were conducted in an oxygen-saturated 1 M KOH solution and scanned 0.2 V to 0.3 V vs. Ag/AgCl, at scan rates of 10, 20, 30, 40, 60, 80, 100, and 120 mV s^{-1} for both HEO and NBCF double perovskite oxide electrocatalysts [148]. Subsequently, at 0.25 V vs. Ag/AgCl, scan rate versus half of the difference between anodic and cathodic current densities ($\Delta J/2 = (J_a - J_c)/2$) plots were generated [149,150]. Following linear fitting, C_{dl} values for synthesized powders were calculated as half of the slope. By dividing C_{dl} by the specific capacitance (C_s), where C_s is equal to 0.040 mF cm^{-2} in 1 M KOH, ECSA was determined [151].

The specific activity ($\text{mA cm}_{\text{powder}}^{-2}$) (SA) of the HEO-Air and HEO-Vac were calculated using the specific BET surface area, whereas for nanoporous HEOs, and NBCF electrocatalysts the SA was calculated with ECSA. The mass activity ($\text{A g}_{\text{powder}}^{-1}$) (MA) of all the electrocatalysts was calculated with mass loading.

A galvanostatic test was performed on HEO-Air and HEO-Vac with GAMRY Interface 1000 potentiostat/galvanostat/ZRA. Carbon paper coated with catalyst ink was air-dried and utilized as the working electrode in a three-electrode cell setup, where platinum is the counter electrode and Hg/HgO is the reference electrode (Figure 3.4). The experiment was conducted using a 0.1 M KOH electrolyte, which remained oxygen-saturated throughout the whole experiment. The test was run with a constant current density of 10 mA cm⁻², and the potential was recorded for 75 hours approximately to evaluate the long-term durability of the electrocatalysts.

Mott-Schottky (MS) analysis was conducted to investigate the band-bending properties of the NBCF electrocatalyst within the OER potential range. The analysis involved conducting EIS measurements across a potential range spanning from -0.5 V to 0.6 V vs. Ag/AgCl, with increments of 50 mV, corresponding to the open circuit voltage (OCP).

To investigate the ORR activity of HEO-Vac, HEO-Air, GLY500, GLY600, GLY700, and NBCF double perovskite oxide electrocatalysts, CV and LSV experiments were carried out in a manner consistent with the procedure outlined earlier for evaluating OER activity. Except, the applied potentials ranged from 0.1V to (-1.2) V vs. Ag/AgCl for the ORR activity. Tafel plots were obtained by plotting overpotential against the logarithm of current density polarization curves. Tafel slopes of the electrocatalysts were determined by fitting the linear portion of the Tafel plots to the Tafel equation. The Koutecky-Levich (K-L) equation (Equation 1) was applied to assess the kinetic current density (J_K) and electron transfer number (n) of all the electrocatalysts. To apply the K-L equation, in an oxygen-saturated 0.1M KOH electrolyte, a sequence of LSV experiments was conducted at a scan rate of 5 mV.s⁻¹, spanning the potential range from 0.2 V to (-0.8) V vs. Ag/AgCl, employing different rotation speeds (400, 800, 1200, 1600, 2000 rpm) [29,152,153].

$$\frac{1}{J} = \frac{1}{J_K} + \frac{1}{J_L} = \frac{1}{nFkC^0} + \frac{1}{0.62nFD_{O_2}^{2/3}v^{-1/6}C^0\omega^{1/2}} \quad (\text{Eqn 1})$$

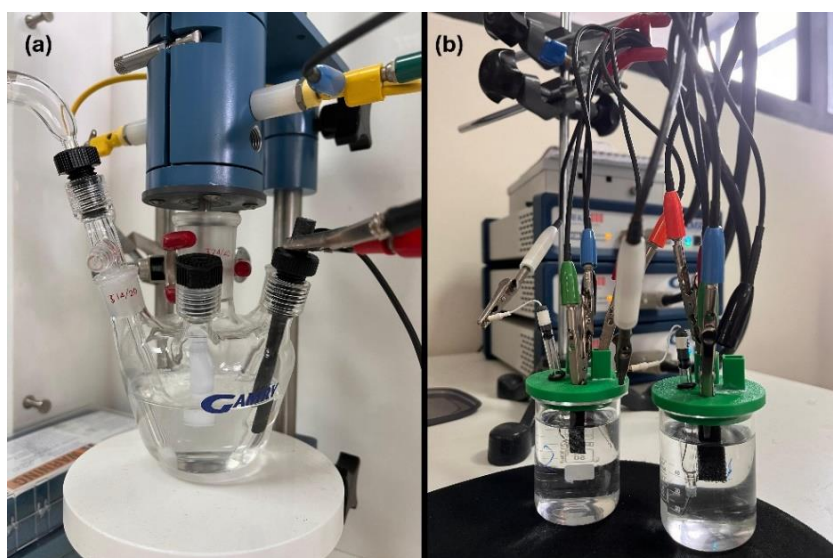


Figure 3.4 (a) RDE set-up (b) Three electrode cell set-up for long-term stability

3.6 Evaluation of the Zn-Air Battery Performance

Zn-air batteries were assembled with zinc foil as the anode, HEO-Vac, HEO-Air, GLY500, GLY600, GLY700, and NBCF double perovskite oxide electrocatalysts as the cathode, with an electrolyte composed of 6.0 M KOH with an additive of 0.2 M Zn(OAC)₂. The air cathodes were created with a gas diffusion layer comprising carbon foam, HEO and NBCF electrocatalysts, and a PTFE film. The air cathode design permits the diffusion of oxygen from the surrounding air into the cell while preventing the leakage of the electrolyte. Following the assembly of the Zn-air batteries, battery performance characteristics were assessed using a GAMRY Interface 1000 potentiostat/galvanostat/ZRA and Neware battery testing system (Figure 3.5).

The discharge and charge polarization curves of Zn-air batteries based on HEO-Vac, HEO-Air, nanoporous HEO, and NBCF double perovskite oxide electrocatalyst on the air cathode, along with their power densities, were evaluated over a current density range of 0 to 200 mA cm⁻².

Full discharge of the batteries was carried out at various current densities to determine specific capacities and specific energies using Equation 2 and Equation 3, respectively. Additionally, for batteries incorporating HEO-Vac, specific capacities, specific energies, and depth of discharge of the Zn foil (DOD_{Zn}) were computed at discharge current densities of 5, 10, 20, and 50 mA cm^{-2} , respectively. In Equation 2 and Equation 3, the symbols denote the following variables: I denotes the applied current, t represents the discharge time, m indicates the consumed zinc mass in grams, and V signifies the voltage observed throughout the discharge plateau. Furthermore, in Equation 4, C denotes the capacity, A represents the area, V indicates the volume, and ρ signifies the zinc foil density.

$$\text{Specific Capacity} = \frac{I \times t}{m} \quad (\text{Eqn 2})$$

$$\text{Specific Energy} = \frac{I \times V \times t}{m} \quad (\text{Eqn 3})$$

$$DOD_{Zn} = \frac{C_{Zn-Air}}{C_{Zn}} = \frac{A \times j \times t}{V_{Zn} \times \rho_{Zn} \times 819.73} = \frac{A_{cathode} \times j \times t}{A_{Zn} \times h_{Zn} \times \rho_{Zn} \times 819.73} \quad (\text{Eqn 4})$$

The capacities of the nanoporous HEO and NBCF-based Zn-air batteries were estimated with a full-discharge of the batteries at 5, 10, 20, and 50 mA.cm^{-2} current densities respectively.

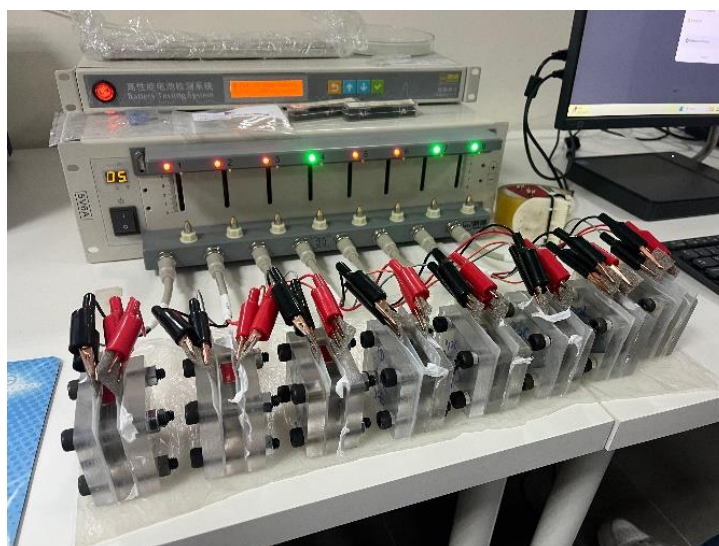


Figure 3.5 Rechargeable Zn-air battery testing with Neware battery testing system

Following the determination of capacities, the cycling stability and rate capability of HEO and NBCF-based Zn-air batteries were assessed by comparing the output voltage of the Zn-Air batteries as they were cycled from 0 to 20 mA cm⁻² and then back to 0 mA cm⁻².

Subsequently, the cyclic charge-discharge performance of the Zn-Air batteries was estimated at a current density of 5 mA cm⁻², with discharge and charge durations of 5 minutes each.

To calculate the coulombic efficiencies of the Zn-air batteries with HEO-Vac and HEO-Air, cyclic charge-discharge tests were applied. Throughout these tests, the batteries were charged for 5 minutes at 5 mA cm⁻², discharged for 5 minutes at 165 ohms, and coulombic efficiencies were determined using equation 5.

$$\text{Coulombic Efficiency} = \frac{Q_{\text{discharge}}}{Q_{\text{charge}}} \text{ where } Q = I \times t \text{ (Eqn 5)}$$

CHAPTER 4

RESULTS AND DISCUSSION FOR $(\text{FeCrCoMnZn})_3\text{O}_{4-\delta}$ ELECTROCATALYSTS SYNTHESIZED IN AIR AND VACUUM ATMOSPHERES

“This chapter contains information used with the permission of JOHN/WILEY & SONS LTD. from “Engineering Oxygen Vacancies in $(\text{FeCrCoMnZn})_3\text{O}_{4-\delta}$ High Entropy Spinel Oxides Through Altering Fabrication Atmosphere for High-Performance Rechargeable Zinc-Air Batteries”, Cagla Ozgur, Tuncay Erdil, Uygur Geyikci, Can Okuyucu, Ersu Lokcu, Yunus Eren Kalay, Cigdem Toparli, Global Challenges 8.1 (2024): 2300199.”

4.1 Crystal Structure and Morphology of the HEO-Air and HEO-Vac Electrocatalysts

The crystal structure of HEO-Air and HEO-Vac electrocatalysts were investigated with the XRD method. Figure 4.1 displays the XRD patterns for both HEO-Air and HEO-Vac. The analysis of these patterns indicated that both samples are single-phase, with no detectable peaks corresponding to impurities such as hydroxides or oxides of Fe, Cr, Co, Mn, and Zn. Then, to investigate the impact of the synthesis environment on the crystal structure Rietveld Refinement analysis was performed both for HEO-Air and HEO-Vac respectively, as seen in Figure 4.1(b) and Figure 4.1(c). The confirmation of the space groups for HEO-Air and HEO-Vac samples was achieved through Rietveld refinement analysis, yielding notably low χ^2 values, as depicted in Table 4.1 and Table 4.2. Both HEO-Air and HEO-Vac exhibit spinel cubic crystal structures with a space group of $Fd\bar{3}m$ (ICDD #04-024-0120) [154,155]. The lattice parameters for HEO-Air and HEO-Vac were determined to be 8.3621 and 8.3520 Å, respectively. Consequently, a decrease in the lattice parameter and cell volume is evident in the HEO electrocatalyst synthesized under a vacuum

atmosphere compared to its counterpart synthesized in air which is attributable to the formation of oxygen vacancies in HEO-Vac's crystal structure.

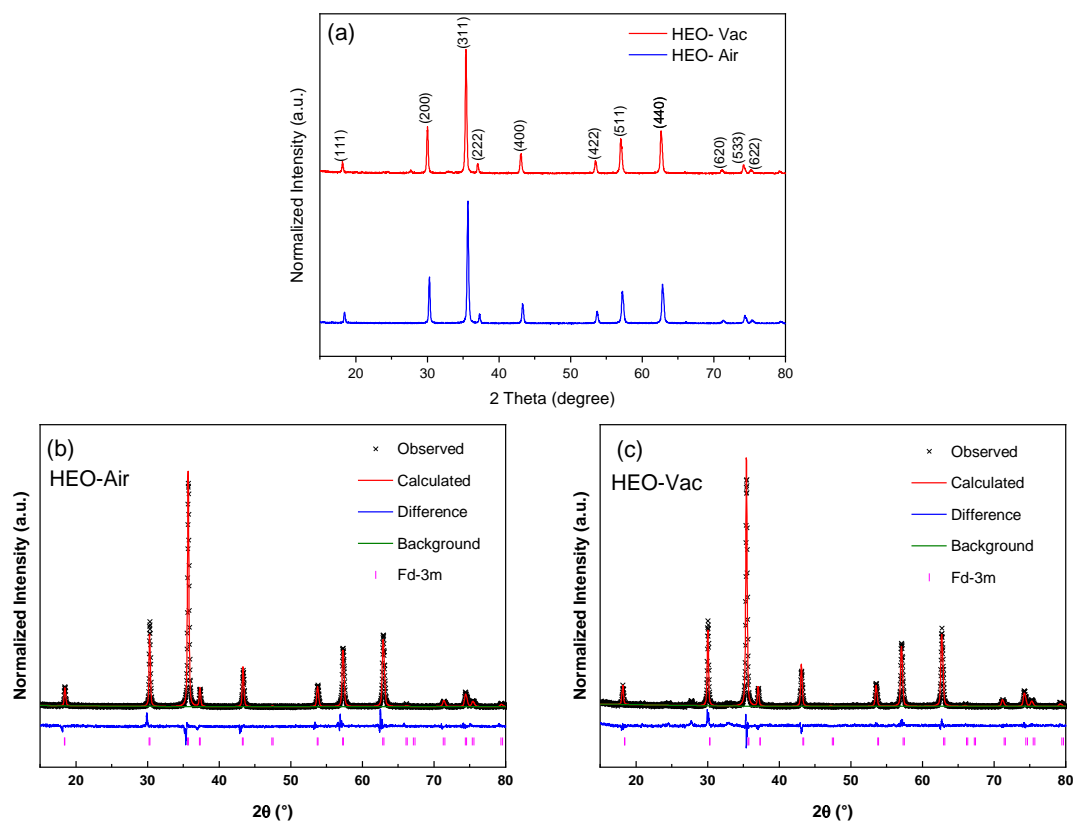


Figure 4.1 (a) XRD patterns of HEO-Air and HEO-Vac. Rietveld refinement analysis performed for (b) HEO-Air (c) HEO-Vac

Table 4.1 Rietveld refinement data for HEO-Air

Sample ID				HEO-Air		
Phase				Spinel		
χ^2				1.358		
Space Group				Fd-3m		
Cell Volume (\AA^3)				584.73		
Crystal Density (g cm^{-3})				5.3668		
Lattice parameter				8.3621		
Label	Wyckoff site	x	y	z	Atom	Occupation
Anion	3m(111)	0.2551	0.2551	0.2551	O	1
Oct.	-3m(111)	0.5	0.5	0.5	Fe	0.2
					Co	0.2
					Cr	0.2
					Mn	0.2
					Zn	0.2
Tetr.	-43m	0.125	0.125	0.125	Fe	0.2
					Co	0.2
					Cr	0.2
					Mn	0.2
					Zn	0.2

Table 4.2 Rietveld refinement data for HEO-Vac

Sample ID				HEO-Vac		
Phase				Spinel		
χ^2				1.913		
Space Group				Fd-3m		
Cell Volume (\AA^3)				582.61		
Crystal Density (g cm^{-3})				5.3864		
Lattice parameter				8.3520		
Label	Wyckoff site	x	y	z	Atom	Occupation
Anion	3m(111)	0.2555	0.2555	0.2555	O	1
Oct.	-3m(111)	0.5	0.5	0.5	Fe	0.2
					Co	0.2
					Cr	0.2
					Mn	0.2
					Zn	0.2
Tetr.	-43m	0.125	0.125	0.125	Fe	0.2
					Co	0.2
					Cr	0.2
					Mn	0.2
					Zn	0.2

To further investigate the crystal structure of the HEOs, we performed several characterizations by HRTEM. Figure 4.2(a) displays a BF TEM image alongside the subsequent SAED pattern from the $\langle 211 \rangle$ zone axis for HEO-Vac. The observed HEO-Vac particle in this image exhibits an approximate size of 400 nm. Examination of the HEO-Vac crystal from the $\langle 211 \rangle$ zone axis further confirms HEO-Vac's spinel cubic crystal structure. HRTEM analysis reveals lattice fringes consistent with the crystalline structure. Fast Fourier transform (FFT) data obtained from this crystal in the $\langle 211 \rangle$ zone axis corresponds to the $Fd\bar{3}m$ (227) space group, with a d-spacing of 0.147 nm for the (440) plane (Figure 4.2(b)). The integration of these findings with the Rietveld analysis conducted on the XRD data confirms the spinel structure of HEO-Vac. Furthermore, the spatial distribution of elements within the HEO-Vac was investigated using HAADF imaging and EDS elemental mapping for Fe, Cr, Co, Mn, Zn, and O in scanning transmission electron microscopy (STEM) mode. The results are presented in Figure 4.2(c). EDS mapping showed a homogeneous distribution of elements within the structure of HEO-Vac. Additionally, the consistent bright contrast observed throughout the HEO-Vac particle in the HAADF image signifies the uniform distribution of elements. Collectively, HRTEM analyses conducted on HEO-Vac confirm the XRD findings, indicating a single-phase homogeneous solid solution with a spinel cubic crystal structure (227).

The HEO-Air powders underwent the same analyses using HRTEM. Figure 4.2(d) displays the BF TEM image and the SAED pattern from the $\langle 211 \rangle$ zone axis for the HEO-Air. The particle size measures approximately 200 nm. For HEO-Air, the SAED pattern confirms the $Fd\bar{3}m$ (227) symmetry established through Rietveld refinement of the XRD results. Furthermore, Figure 4.2(e) showcases the HRTEM image and the subsequent FFT pattern from the $\langle 211 \rangle$ zone axis, confirming the spinel cubic structure with a d-spacing of 0.149 nm for the (440) plane. The homogeneous distribution of Fe, Cr, Co, Mn, Zn, and O elements is evident in the HAADF image, while in Figure 4.2(f) the EDS elemental mapping results are presented.

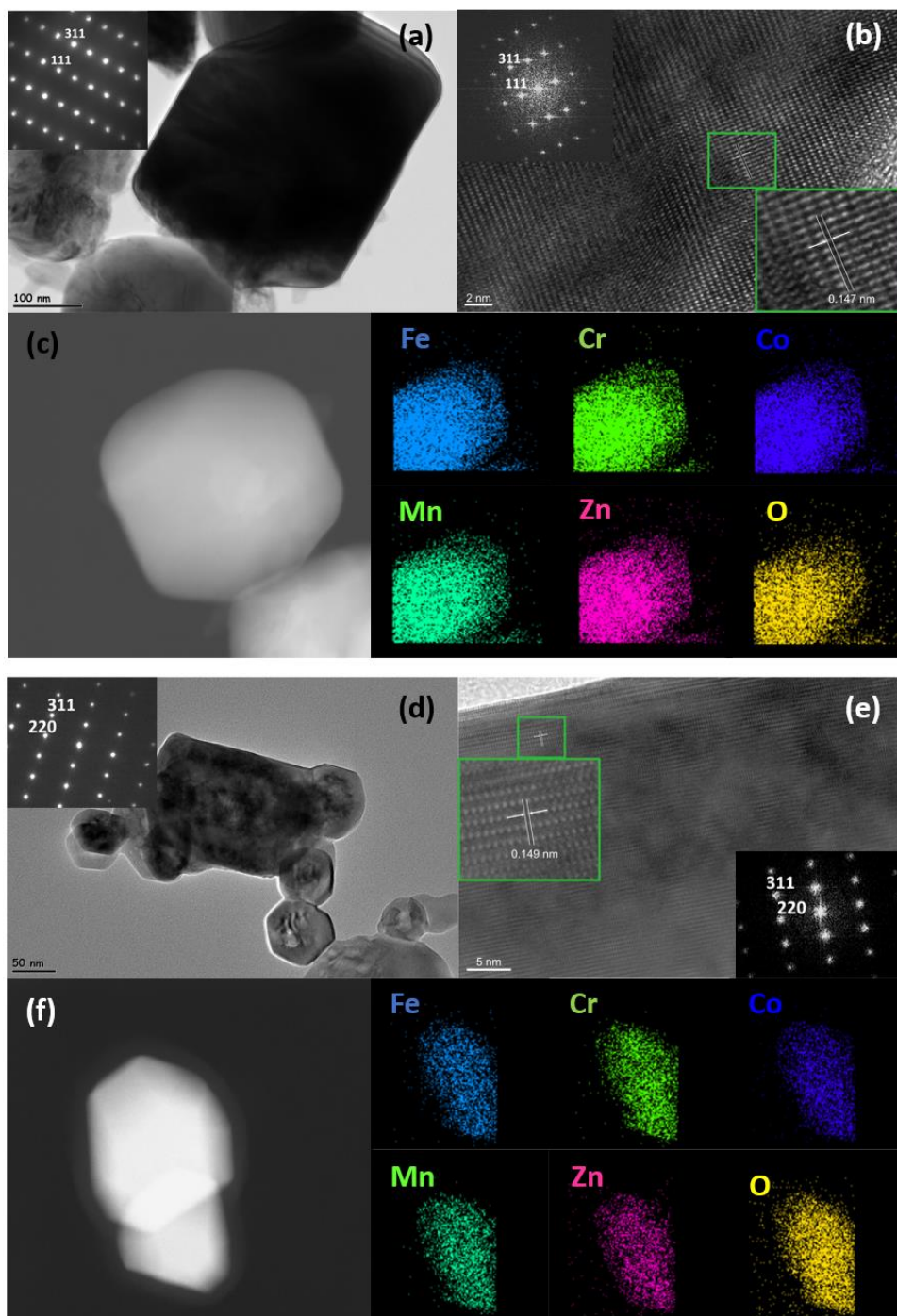


Figure 4.2 HEO-Vac's (a) BF TEM image and the inset displays the SAED pattern from $\langle 211 \rangle$ zone axis (b) HRTEM image and the inset shows the FFT pattern (c) HADDF image and corresponding EDS element mapping of Fe, Cr, Co, Mn, Zn, and O. HEO-Air's (d) BF TEM and the inset displays the SAED pattern from the $\langle 211 \rangle$ zone axis (e) HRTEM image and inset shows the FFT pattern (f) HADDF image and corresponding EDS element mapping of Fe, Cr, Co, Mn, Zn, and O

4.2 Electronic Structure of the HEO-Air and HEO-Vac Electrocatalysts

Figure 4.3 illustrates the deconvolution of XPS core level spectra for Fe 2p, Cr 2p, Co 2p, Mn 2p, and Zn 2p. The Co LMM peak overlaps with the deconvolution of Fe 2p due to the Co LMM peak's interference in the Fe 2p region, presenting challenges in Fe 2p spectra deconvolution. Nonetheless, in Figure 4.3(a), peaks corresponding to Fe 2p_{3/2}, Fe 2p_{3/2} satellite, Fe 2p_{1/2}, and Fe 2p_{1/2} satellite are evident at 711 eV, 718 eV, 724 eV, and 732 eV binding energies, respectively. The satellite indicates Fe⁺³ is observable in the sample calcined in air, but it is absent in the spectra of vacuum-synthesized HEO [11]. The Cr 2p spectra in Figure 4.3(b), display peaks positioned at 586 eV and 576 eV, corresponding to the Cr 2p_{1/2} and Cr 2p_{3/2} signals, respectively. These peaks indicate the presence of Cr in the +3 oxidation state in both vacuum and air-synthesized HEO electrocatalysts. In Figure 4.3(c), the Co 2p spectra display Co 2p_{3/2}, Co 2p_{3/2} satellite, Co 2p_{1/2}, and Co 2p_{1/2} satellite peaks positioned at binding energies of 780, 786, 796, and 802 eV, respectively. Co 2p XPS core level spectra of HEO-Vac and HEO-Air show a prominent Co⁺² satellite, suggesting that both HEO-Air and HEO-Vac exhibit the same state of Co. Figure 4.3(d) show the Mn 2p XPS core level spectra, featuring peaks positioned at binding energies of 641 eV, 645 eV, and 653 eV, corresponding to Mn 2p_{3/2}, MnO satellite, and Mn 2p_{1/2}, respectively. The Mn 2p XPS core level spectra indicate the presence of MnO in both HEO-Air and HEO-Vac samples, although Mn₂O₃ may also be present in the vacuum-synthesized HEO [156]. The Zn 2p XPS core level spectra presented in Figure 4.3(e) suggest the presence of the Zn⁺² state in all samples, with Zn 2p_{3/2} and Zn 2p_{1/2} peaks observed at binding energies of 1021 eV and 1045 eV, respectively [157].

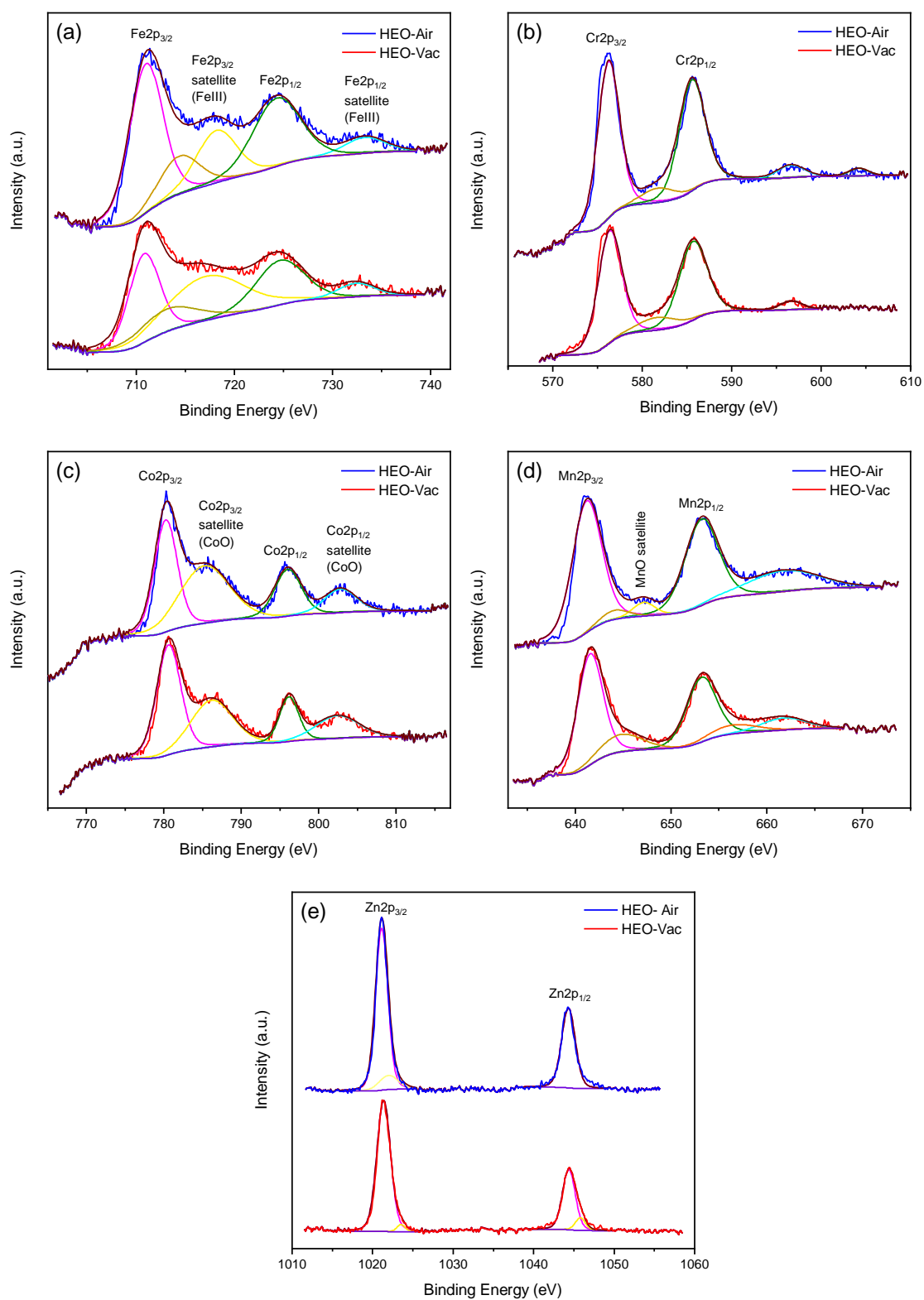


Figure 4.3 Deconvolution of XPS core level spectra for (a) Fe 2p (b) Cr 2p (c) Co 2p (d) Mn 2p, and (e) Zn 2p

Figure 4.4(a) displays fitted O 1s XPS core level spectra of HEO-Air and HEO-Vac, showing the presence of lattice oxygen (O_L) and oxygen vacancies (O_V) at binding energies of 529 eV and 532 eV, respectively. For HEO-Vac, the oxygen vacancy peak accounts for 43.58% of the total O 1s spectra, whereas for HEO-Air, it represents 26.13% of the overall area. Thus, a decrease in the oxygen content in the synthesis environment correlates with an increase in the quantity of oxygen vacancies within the structure, as observed in the O 1s XPS core level spectra. EPR was utilized to investigate and compare the oxygen vacancy content of HEO-Air and HEO-Vac further. The oxygen vacancy content of the electrocatalysts was assessed based on the EPR signal at $g = 2.005$ (Figure 4.4(b)). The EPR peak intensity of HEO-Vac is notably higher as compared to HEO-Air, indicating a higher oxygen vacancy content in HEO-Vac.

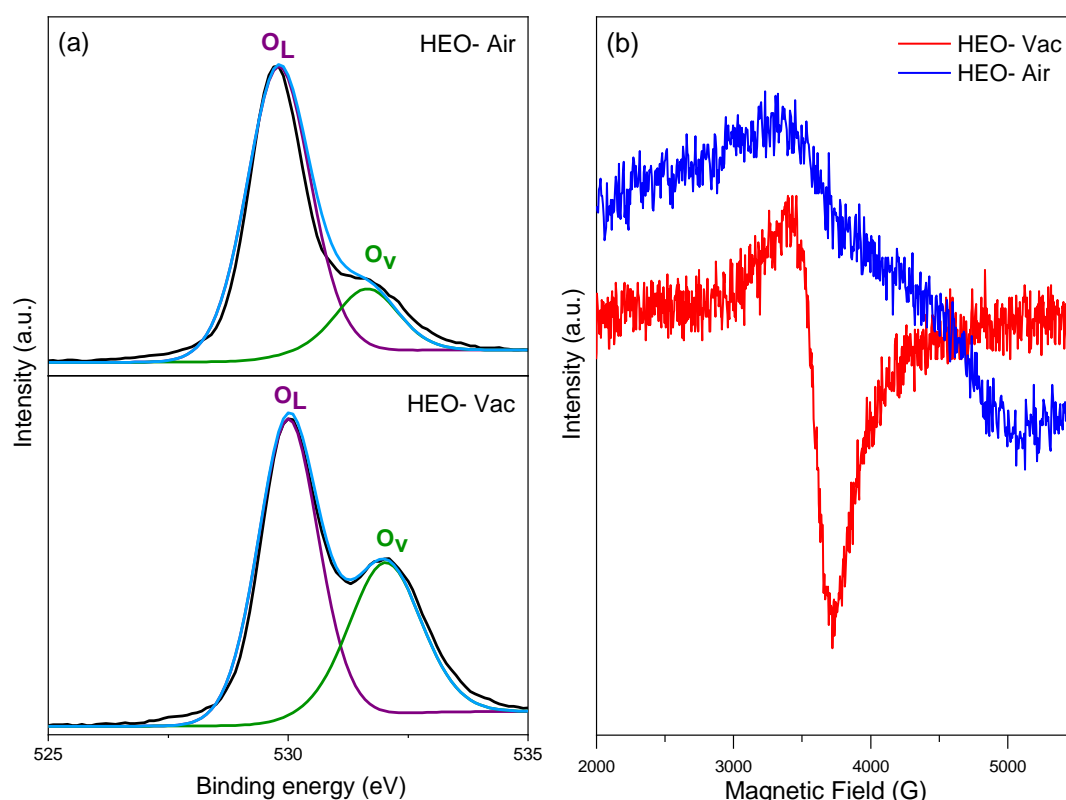


Figure 4.4 HEO-Air and HEO-Vac electrocatalyst's (a) O 1s XPS core level spectra (b) EPR spectrum

4.3 OER/ORR Performance of the HEO-Air and HEO-Vac Electrocatalysts

The primary objective of this thesis is to explore the influence of the synthesis environment on the bifunctional OER/ORR activity of $(\text{FeCrCoMnZn})_3\text{O}_{4-\delta}$ powders. To achieve this aim, an extensive investigation was conducted, beginning with the successful synthesis of our powders under both air and vacuum atmospheres. Following the synthesis, a comprehensive characterization of the powders was performed employing a range of advanced techniques including XRD, TEM, XPS, and EPR. Once the powders were characterized, the bifunctional electrocatalytic OER/ORR performance of HEO-Air and HEO-Vac was systematically evaluated. This evaluation was carried out utilizing a standard three-electrode system incorporated within the RDE setup. As explained in the experimental chapter before, a three-electrode setup consists of an Ag/AgCl as a reference electrode, Pt as a counter electrode, and catalyst ink dropped glassy carbon as a working electrode. During the tests, oxygen-saturated 0.1 M KOH solution was used unless otherwise stated. LSV was conducted on both HEO-Air and HEO-Vac utilizing a reference electrode of Ag/AgCl, with the obtained potentials converted to the RHE scale. Moreover, the LSV curves were normalized based on the geometric area of the GCE, which is 0.0707 cm^2 . The LSV curves both for HEO-Air and HEO-Vac are presented in Figure 4.5(a) At a current density of 10 mA cm^{-2} , which is a significant value to understand the electrocatalytic OER activity of a catalyst according to the literature, the overpotential values were measured. As a result, the overpotential values for HEO-Air and HEO-Vac were determined to be 404 mV and 329 mV, respectively. Hence, the overpotential of the HEO-Air and HEO-Vac are comparable with the previously reported benchmark electrocatalysts such as IrO_2 , Pt/C, and RuO_2 . Notably, the considerably lower overpotential observed for HEO-Vac compared to HEO-Air can be attributed to the elevated oxygen vacancy content of HEO-Vac [30,158].

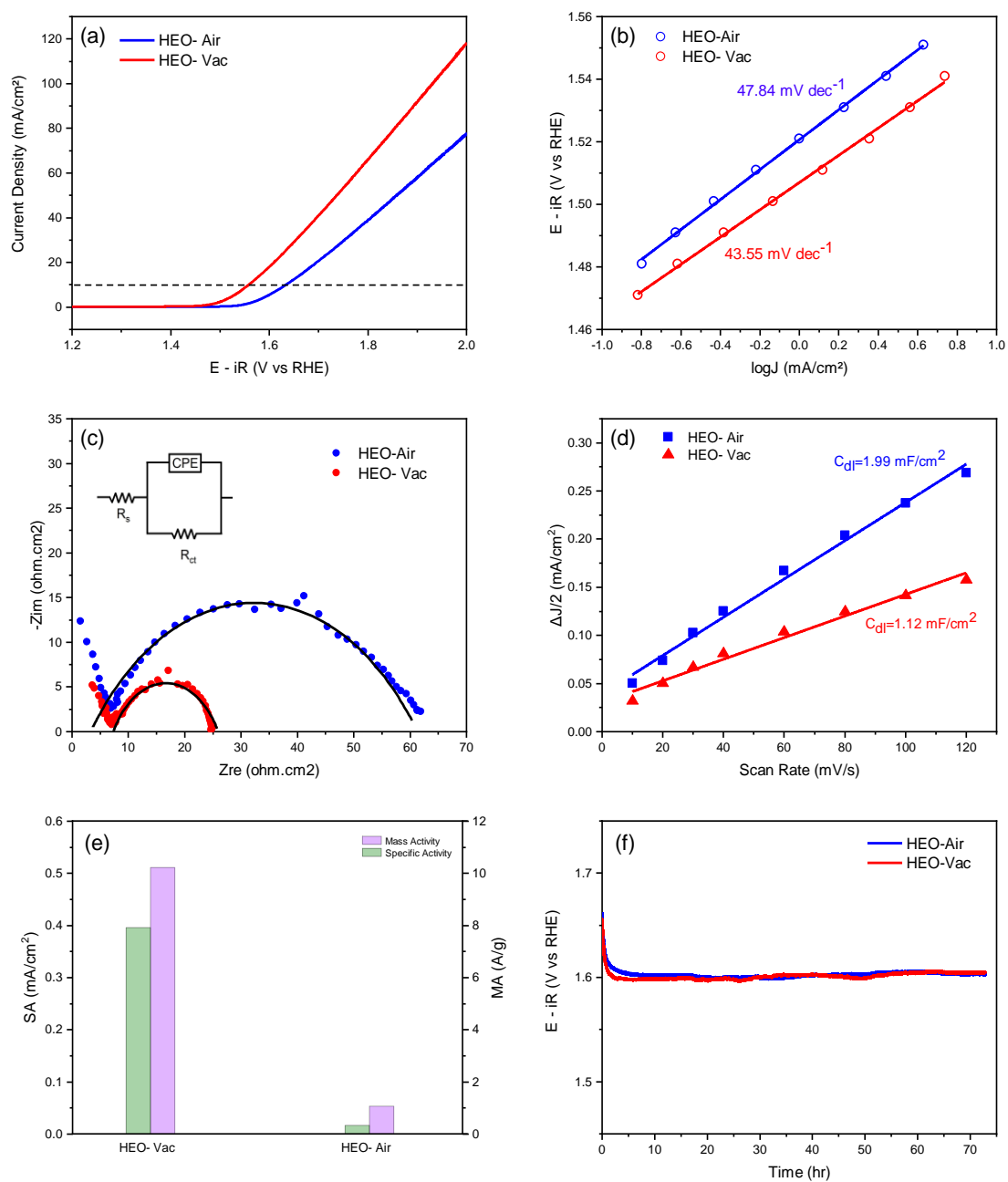


Figure 4.5 HEO- Air and HEO-Vac electrocatalyst's (a) LSV curves at OER region (b) Tafel plots (c) EIS data (d) Electric double layer capacitance analysis (e) Mass activity and specific activity calculations (f) Galvanostatic stability curve recorded at a current density of 10 mA cm^{-2}

To explore and compare the electrochemical reaction kinetics of the samples, Tafel slopes were determined using the multistep chronoamperometry (CA) method, considering steady-state current variables. To ensure that the specimen was in a steady-state current condition for a comprehensive understanding of its kinetic behavior, we employed the multistep chronoamperometry method with incremental voltage steps. This chronoamperometry test was conducted within the potential range of 0.40 – 0.65 V vs. Ag/AgCl, with a step increment of 0.01 V, as depicted in Figure 4.6. This potential range was specifically selected as it corresponds to the region where the water splitting and OER primarily occur for HEO-Air and HEO-Vac electrocatalysts. The graph showing steady-state current density versus potential serves as the counterpart to the LSV curve, with the key distinction being that the current is measured over longer durations, ultimately reaching a steady-state in the multistep chronoamperometry approach. As depicted in Figure 4.5(b), the Tafel slopes are calculated as 47.84 and 43.55 mV dec⁻¹, respectively for HEO-Air and HEO-Vac by multistep chronoamperometry method. Consequently, HEO-Vac demonstrates faster reaction kinetics, characterized by a lower Tafel slope as compared to HEO-Air.

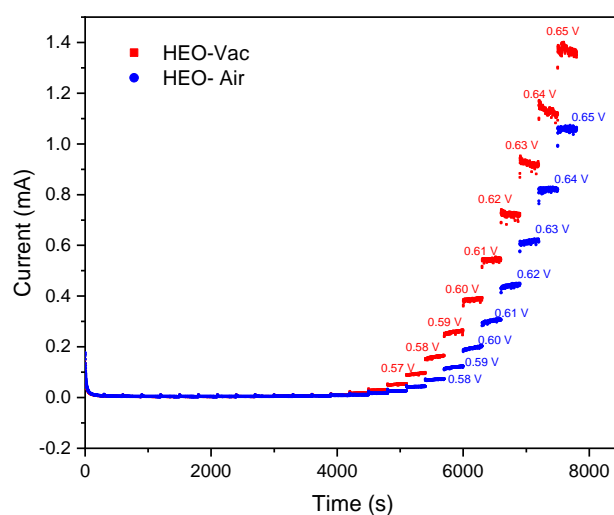


Figure 4.6 Multistep chronoamperometry to determine the Tafel slopes for HEO-Air and HEO-Vac.

Electrochemical impedance spectroscopy (EIS) was utilized to assess the charge transfer rate of the electrocatalysts. Figure 4.5(c) displays the fitted EIS data, including the charge-transfer resistance (R_{ct}), the solution resistance (R_s), and a constant-phase element (CPE). The charge transfer resistance of HEO-Air is measured at 56.3Ω , while HEO-Vac exhibits a resistance of 18.34Ω . This finding suggests that HEO-Vac possesses superior electrocatalytic activity for the OER due to its higher conductivity and faster charge transfer compared to HEO-Air. As explained in the experimental section, ECSA is calculated with the C_{dl} , obtained from CV measurements conducted across various scan rates within the non-faradaic region. CVs were performed in a 1 M KOH solution saturated with oxygen, scanning between 0.2 V and 0.3 V vs. Ag/AgCl, at scan rates ranging from 10 to 120 mV s^{-1} for both HEO-Air and HEO-Vac electrocatalysts, as depicted in Figure 4.7, C_{dl} values for HEO-Air and HEO-Vac were computed as 1.99 mF cm^{-2} and 1.12 mF cm^{-2} , respectively (Figure 4.5(d)). Given the superior electrocatalytic activity of HEO-Vac compared to HEO-Air, it is probable to attribute the enhanced performance of HEO-Vac to its superior intrinsic activity instead of ECSA [159].

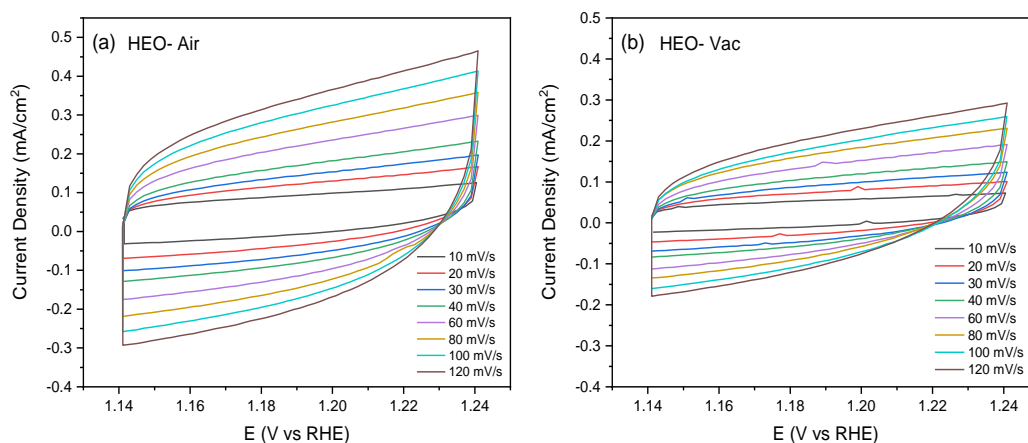


Figure 4.7 Cyclic Voltammetry (CV) scans were conducted for (a) HEO-Air (b) HEO-Vac at scan rates of 10, 20, 30, 40, 60, 80, 100, and 120 mV s^{-1}

To evaluate the intrinsic activity, we determined the MA and SA of both HEO-Air and HEO-Vac. MA was estimated based on the mass loading of the electrocatalysts, while SA was determined using the BET specific area analysis. The BET data for HEO-Air and HEO-Vac is represented in the Table 4.3 and Table 4.4. Notably, the MA and SA of HEO-Vac were significantly greater than those of HEO-Air, as illustrated in Figure 4.5(e). Specifically, the MA of HEO-Vac (10.19 A g^{-1}) and SA of HEO-Vac ($0.39456 \text{ mA cm}^{-2}$) surpassed those of the benchmark electrocatalyst RuO_2 , which recorded an MA of 8.87 A g^{-1} and an SA of $0.06224 \text{ mA cm}^{-2}$ [160].

Table 4.3 Bet analysis data for HEO-Air

Area		7.01 m^2/g
Slope		485.9
Y-Intercept		10.95
Correlation Coefficient		0.998366
C		45.36
P/P₀	Volume [cc/g]	$1/(W((P_0/P)-1))$
0.055183	1.3273	35.21
0.087283	1.4311	53.47
0.11243	1.5133	66.97
0.16212	1.6408	94.35
0.21037	1.918	111.1
0.26148	2.091	135.5
0.31204	2.2184	163.6

Table 4.4 Bet analysis data for HEO-Vac

Area		2.58 m ² /g
Slope		1256
Y-Intercept		92.47
Correlation Coefficient		0.992367
C		14.58
P/P₀	Volume [cc/g]	1/(W((P₀/P)-1))
0.061216	0.3399	153.5
0.087886	0.3746	205.8
0.11292	0.4002	254.5
0.21155	0.6115	351.1
0.2624	0.6751	421.6

To explore HEO-Air and HEO-Vac electrocatalysts' long-term stability galvanostatic tests were carried out while applying a constant current density of 10 mA cm⁻². The experimental setup involved subjecting the electrocatalysts to continuous current flow to evaluate their performance over an extended period. The results depicted in Figure 4.5(f) indicate that both HEO-Air and HEO-Vac exhibit exceptional stability, suggesting their potential suitability for prolonged electrochemical applications. Both HEO-Air and HEO- Vac does not lose their electrocatalytic activity even after 75 hours. Hence, their catalytic activity is exceedingly higher than the state-of-the-art electrocatalysts such as IrO₂, which lost its stability after 2 hours.

To gain insights into the bifunctional OER/ORR performance of the electrocatalysts, the oxygen reduction reaction activity of the HEO-Air and HEO-Vac was evaluated, as illustrated in Figure 4.8. First, we generated LSV curves, like the approach adopted for the OER activity analysis as explained in the experimental section (Figure 4.8(a)). At a current density of -1 mA cm^{-2} , the potentials recorded for HEO-Air and HEO-Vac were 0.63 V and 0.67 V , respectively. Consequently, it is evident that the ORR activity of HEO-Vac surpasses that of HEO-Air. Then, as shown in Figure 4.8(b) Tafel plots were utilized to determine the Tafel slopes. Tafel slopes were calculated as -141 mV dec^{-1} for HEO-Air and -155 mV dec^{-1} for HEO-Vac.

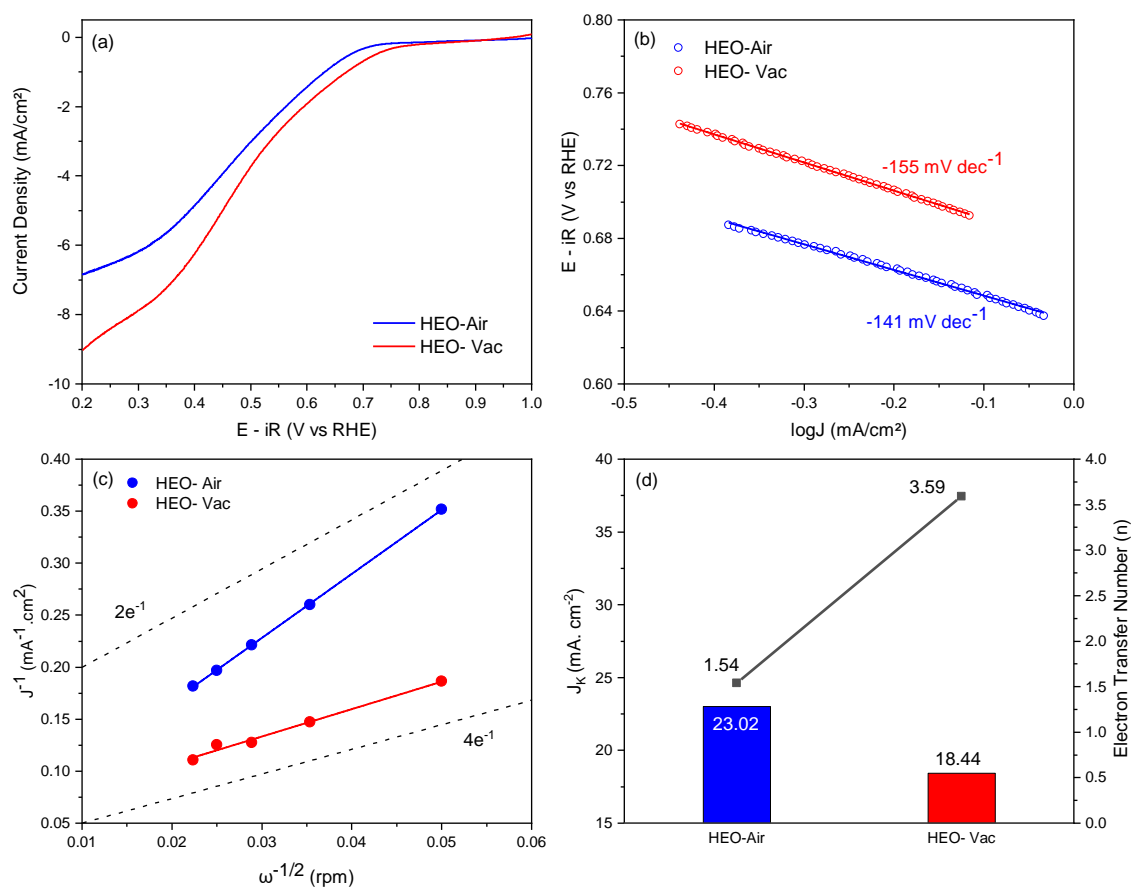


Figure 4.8 HEO- Air and HEO- Vac electrocatalysts' (a) ORR activity curves (b) Tafel plots (c) Koutecky-Levich plots at 0.15V (d) Kinetic current density (J_k) and electron transfer number (n).

To further investigate the electrocatalytic activity and kinetics of HEO-Air and HEO-Vac, calculations were performed to determine the electron transfer number and kinetic current densities using the K-L equation. As seen in Figure 4.8(c), Koutecky-Levich (K-L) plots were constructed through LSV experiments employing an RDE. These experiments spanned a potential range from 1.2 V to 0.14 V vs. RHE at various rotation speeds of 400, 800, 1200, 1600, and 2000 rpm, with a scan rate of 5 mV s⁻¹. As the rotational speed of the working electrode rises, there is a corresponding increase in the reduction current, attributed to the improvement of mass transport at the surface of the working electrode (Figure 4.9(a) and Figure 4.9(b)). The acceleration in rpm increases the oxygen diffusion from the electrolyte to the electrocatalyst surface. Consistently, HEO-Vac demonstrates a superior reduction current density under both constant potential and rotational speed conditions as compared to HEO-Air. The K-L plots for HEO-Air and HEO-Vac at 0.50, 0.40, 0.30, 0.25, 0.20, and 0.15 V vs. RHE reduction potentials are depicted in Figure 4.9(c) and Figure 4.9(d). These plots exhibit linearity which indicates that the ORR follows first-order kinetics. At a low voltage of 0.15 V vs. RHE, the electron transfer number was determined to be 3.59 for HEO-Vac and 1.54 for HEO-Air, as shown in Figure 4.8(c). The electron transfer number of HEO-Vac which is closer to 4, indicates a predominance of the 4-electron ORR process, whereas, for HEO-Air, the 2-electron ORR process is dominant [161,162]. Consequently, the HEO synthesized in a vacuum environment demonstrates improved electrocatalytic activity due to its four-electron ORR process, attributed to its elevated oxygen vacancy content compared to HEO-Air. These oxygen vacancies may facilitate easier charge transfer and oxygen gas adsorption, thus improving the ORR performance of HEO-Vac. Additionally, to further elucidate the reaction kinetics of HEO-Air and HEO-Vac, kinetic current densities were determined to be 23.02 mA cm⁻² for HEO-Air and 18.44 mA cm⁻² for HEO-Vac as illustrated in Figure 4.8(d).

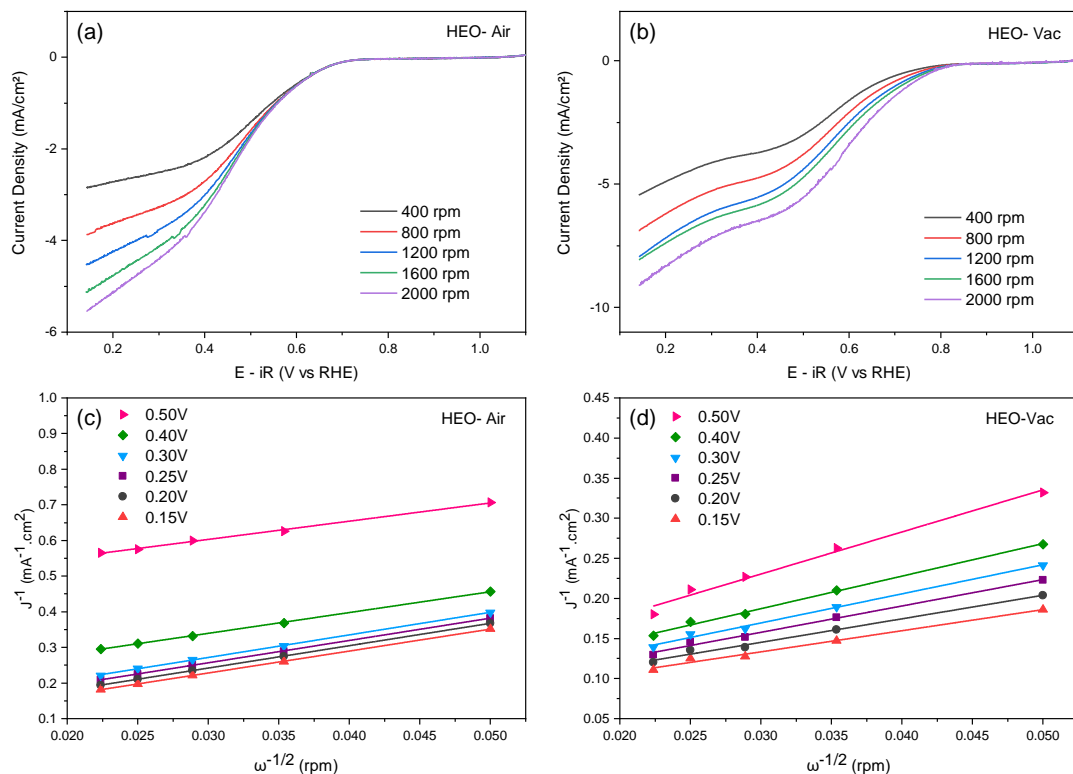


Figure 4.9 At 400, 800, 1200, 1600, 2000 rpm rotation speeds (a) LSV experiments for HEO-Air and (b) LSV experiments HEO-Vac. At potentials ranging from 0.50 to 0.15 V, Koutecky-Levich (K-L) for (c) HEO-Air and (d) HEO-Vac

The bifunctional index (BI) serves as a metric to assess the electrocatalysts' proficiency in both the OER and ORR within an alkaline environment. It is calculated with the potential difference between -1 mA cm^{-2} and 10 mA cm^{-2} current densities. A lower BI indicates superior performance in both OER and ORR. In this thesis, the BI for HEO-Air is determined to be 1.0 V, whereas for HEO-Vac, it is found to be 0.89 V. Consequently, the BI of HEO-Vac is notably lower (and hence, better) compared to HEO-Air. This signifies that HEO-Vac exhibits significantly enhanced electrocatalytic activity in both the OER and ORR processes.

4.4 Materials Characterization after Galvanostatic Stability Test

Following the galvanostatic stability experiments, additional XRD and HRTEM characterizations were conducted to study possible changes in the structure and composition of the HEO-Vac and HEO-Air particles. The XRD analyses depicted in Figure 4.10(a) provide an overview of any structural modifications. The noticeable presence of graphite, nickel, and foam peaks in the XRD data can be attributed to the utilization of carbon foam-coated nickel during the galvanostatic stability experiments. This foam facilitated the adherence of the particles to the electrodes, making them inseparable post-tests, thereby necessitating XRD analyses on the HEO particles remained to this foam. Upon the removal of these peaks, the remaining peaks demonstrated a consistent alignment with the $Fd\bar{3}m$ (227) spinel cubic structure. Consequently, it can be inferred that no phase transformations occurred for the HEO-Air and HEO-Vac particles throughout the stability assessments.

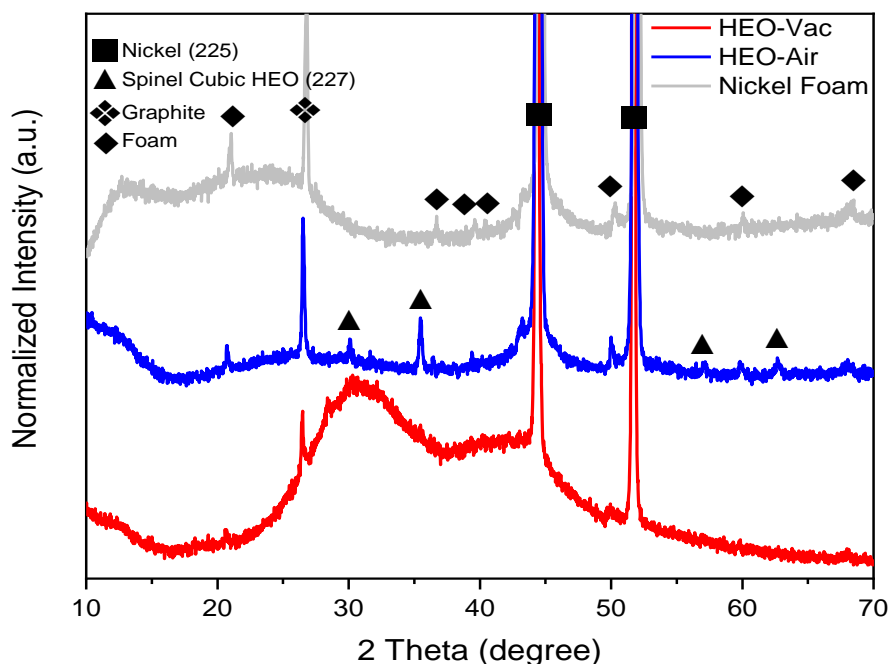


Figure 4.10 XRD patterns of the HEO-Air, HEO-Vac and the carbon foam-coated nickel after the galvanostatic stability test

The BF TEM image of the HEO-Vac powder in Figure 4.11(a) shows an average particle size of 200 nm, consistent with experimental measurements before the stability experiments. Its SAED pattern from $\langle 110 \rangle$ zone axis confirms the presence of spinel cubic crystal structure. HRTEM images of HEO-Vac particles after galvanostatic stability show no signs of structural alterations or amorphization following the electrochemical tests (Figure 4.11(b) and Figure 4.11(c)). The crystallinity of the particles remains, as evidenced by FFT signals validating the spinel cubic structure with space group $Fd\bar{3}m$ (227). STEM mode gives information about the possible chemical changes. HAADF imaging as illustrated in Figure 4.11(d), indicates no visible chemical changes, with consistent single bright contrast observed inside the particles. EDS mapping confirms these findings, illustrating a uniform distribution of elements. Thus, it is evident that the single-phase spinel cubic crystal structure, along with homogeneous elemental distribution, remains unchanged after galvanostatic stability experiments.

The examination for any changes in the HEO-Air particles after electrochemical stability tests followed a similar procedure with HEO-Vac particles. BF TEM images of HEO-Air in Figure 4.11(e) and Figure 4.11(f) illustrate unchanged morphology compared to HEO-Air particles before galvanostatic stability tests, indicating the single-phase crystal structure. HRTEM analysis in Figure 4.11(g) confirms the unchanged crystalline nature of HEO-Air particles after stability tests, with FFT signals from $\langle 211 \rangle$ zone axis validating the conservation of the $Fd\bar{3}m$ (227) spinel cubic structure during electrochemical activity. Chemical distribution analysis via HAADF and EDS elemental mapping in Figure 4.11(h) reveals no element segregation after the galvanostatic stability experiment, emphasizing the structural integrity and homogeneity of HEO-Air particles throughout stability tests.

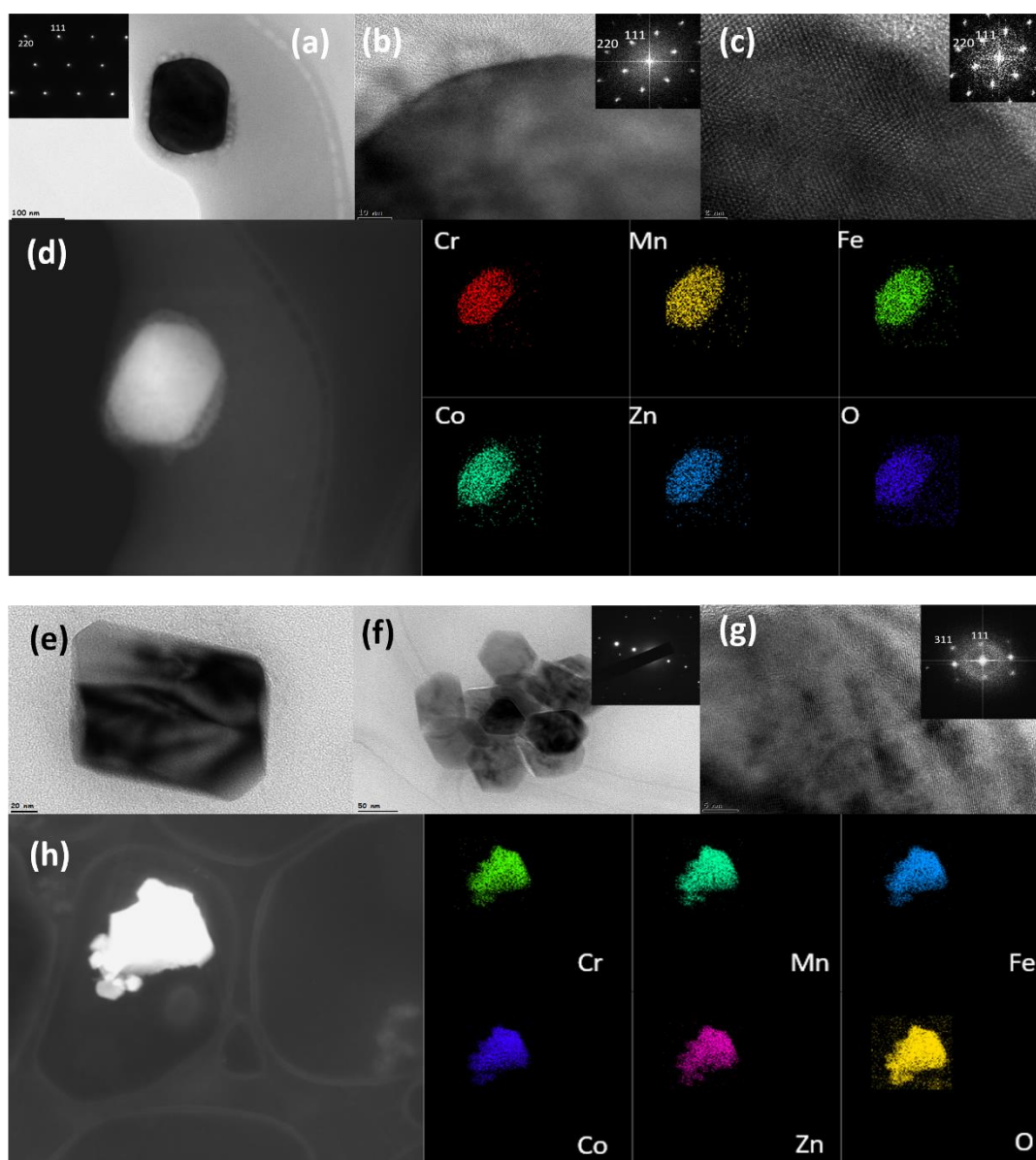


Figure 4.11 HRTEM after the galvanostatic stability test for HEO-Vac and HEO-Air. HEO-Vac's (a) BF TEM image, with the SAED pattern inside (b,c) HRTEM images, with the insets showing the FFT signals (d) HAADF image and subsequent EDS elemental mapping. HEO-Air's (e,f) BF TEM images, with the inset displaying the SAED pattern (g) HRTEM analysis, with the inset showing the FFT signal (h) HAADF image and EDS elemental mapping.

4.5 Evaluation of Zinc-Air Battery Performance of HEO-Air and HEO-Vac Electrocatalysts

The Zn-air battery consists of a Zn plate serving as the anode, a high entropy spinel oxide cathode, and a 6 M KOH electrolyte containing 0.2 m Zn(OAc)₂ additive. Comparing the open-circuit potential (OCP) values, the OCP of HEO-Vac is slightly higher than that of HEO-Air.

Figure 4.12(a) illustrates the discharge and charge polarization curves of the Zn-air battery using HEO-Vac and HEO-Air catalysts in the air cathodes. The HEO-Vac based Zn-air battery shows a lower charging voltage and higher discharge voltage compared to the HEO-Air based Zn-air battery. This indicates that the HEO-Vac catalyst has a reduced voltage difference between the OER and ORR during the charge and discharge cycles, enhancing the battery's rechargeability. Specifically, at a current density of 10 mA cm⁻², the HEO-Vac cathode requires 1.279 V for charging and 1.165 V for discharging. In contrast, the HEO-Air cathode needs 1.838 V for charging and 1.059 V for discharging (Figure 4.12(a)). The HEO-Vac based Zn-air battery achieves a significant peak power density of 102 mW cm⁻² at a current density of 180 mA cm⁻², better than the 82 mW cm⁻² power density of the HEO-Air based Zn-air battery and comparable to the power densities reported for catalysts in earlier studies.

The specific capacities of the Zn-air battery with HEO-Vac at various current densities, ranging from 5 to 50 mA cm⁻², alongside the specific capacity of the Zn-air battery with HEO-Air at 5 mA cm⁻² current density are presented in Figure 4.12(b). The Zn-air battery with the HEO-Vac catalyst attains a maximum specific capacity of 576.07 mA h g_{Zn}⁻¹, approximately 70% of the theoretical Zn capacity (820 mA h g_{Zn}⁻¹), at 5 mA cm⁻², along with a specific energy of 662.46 W h kg⁻¹. Notably, the HEO-Vac-based Zn-air battery demonstrates excellent high-rate capability, delivering specific capacities of 479.89, 376.76, and 225.31 g_{Zn}⁻¹ at current densities of 10, 20, and 50 mA cm⁻², respectively. In comparison, the Zn-air

battery with the HEO-Air cathode achieves a specific capacity of only 190.77 mA h g_{Zn}⁻¹ at a discharge rate of 5 mA cm⁻².

Moreover, meeting the technologically significant benchmark of 100 W h kg⁻¹ necessitates a minimum depth of discharge of zinc (DOD_{Zn}) of 0.20 within a Zn-air battery [163]. In this study, the DOD_{Zn} values were computed for HEO-Vac-based Zn-air batteries at current densities of 5, 10, 20, and 50 mA cm⁻², resulting in 0.70, 0.59, 0.46, and 0.27, respectively. In contrast, the DOD_{Zn} of HEO-Air based Zn-air battery is equal to 0.23.

Figure 4.12(c) provides a comparative analysis of the rate capabilities and cycling stabilities between Zn-air batteries utilizing HEO-Vac and HEO-Air cathodes. The discharge rates were adjusted stepwise from 0 to 20 mA cm⁻² and back to 0 mA cm⁻² to measure the output voltage. The HEO-Vac based Zn-air battery demonstrates superior rate capability and stability. After 400 minutes of operation, the output voltage remains at 1.336 V, maintaining 98.45% of the initial output voltage of 1.357 V. In contrast, the Zn-air battery with the HEO-Air cathode shows an output voltage of 1.229 V, which is 94.54% of its initial output voltage of 1.30 V after the same duration.

To evaluate the electrochemical durability of Zn-air batteries, cyclic charge-discharge tests were conducted at a constant current density of 5 mA cm⁻². The Zn-air battery with HEO-Vac cathode demonstrates a charge voltage of 2.0 V and a discharge voltage of 1.1 V throughout the cycling process, maintaining a voltage gap of 0.9 V, as depicted in Figure 4.12(d). Notably, the discharge and charge voltages of the HEO-Vac based Zn-air battery stay constant over 300 hours of cycling, featuring its exceptional rechargeability and durability. This suggests that the HEO-Vac catalyst effectively catalyzes OER/ORR during both discharge and charge cycles, even after 300 hours of operation. In contrast, during the initial cycles the HEO-Air based Zn-air battery exhibits a charge voltage of 2.5 V and a discharge voltage of 1.0 V, with a wider voltage gap compared to the Zn-air battery with HEO-Vac cathode. Additionally, the stability of the HEO-Air based Zn-air battery was lost

after approximately 75 hours of operation, as expected. This outcome aligns with the lower bifunctional electrocatalytic activity of HEO-Air discussed in Section 4.3 of this thesis. Therefore, the Zn-air battery utilizing the HEO-Vac electrocatalyst outperforms the one employing the HEO-Air electrocatalyst, primarily owing to the superior bifunctional OER/ORR performance of HEO-Vac, attributed to its higher oxygen vacancy content.

To gain deeper insights into the cycling behavior of Zn-air batteries utilizing HEO-Vac and HEO-Air cathodes, the Coulombic efficiency of the batteries was evaluated. This involved charging the batteries at a 5 mA cm^{-2} steady current density for 5 minutes, followed by discharging them under a constant load of $165 \text{ } \Omega$ (equivalent to an average discharge current density of 5 mA cm^{-2}) for 5 minutes, repeated over 350 cycles. Figure 4.12(e) illustrates that the Coulombic efficiency of the HEO-Vac-based Zn-air battery consistently remained above 87%, peaking at 96% at its highest point. In contrast, the HEO-Air-based Zn-air battery's Coulombic efficiency fluctuated below 87%, dropping to 80% at its lowest point over the 350 cycles. Furthermore, the durability performance of both HEO-Air and HEO-Vac based Zn-air batteries during the initial seven cycles of cyclic charge-discharge is depicted in Figure 4.12(f). This plot highlights the charge-discharge voltages and the difference in voltage gap between the Zn-air batteries with HEO-Air and HEO-Vac electrocatalysts.

Figure 4.12(g) illustrates that the OCP of the Zn-Air battery utilizing the HEO-Vac electrocatalyst is recorded at 1.538 V. Additionally, Figures 4.12(h) and Figure 4.12(i) demonstrate that the Zn-Air battery employing the HEO-Vac electrocatalyst in an air cathode successfully powered a panel featuring red LEDs, marked with the acronym "METU". To emphasize its practical applicability, two Zn-air batteries equipped with HEO-Vac air cathodes were connected in series. These combined batteries achieved an open circuit voltage of 2.952 V and provided continuous and reliable power to illuminate 35 red LEDs (each requiring 2.7 V) for a duration exceeding 48 hours.

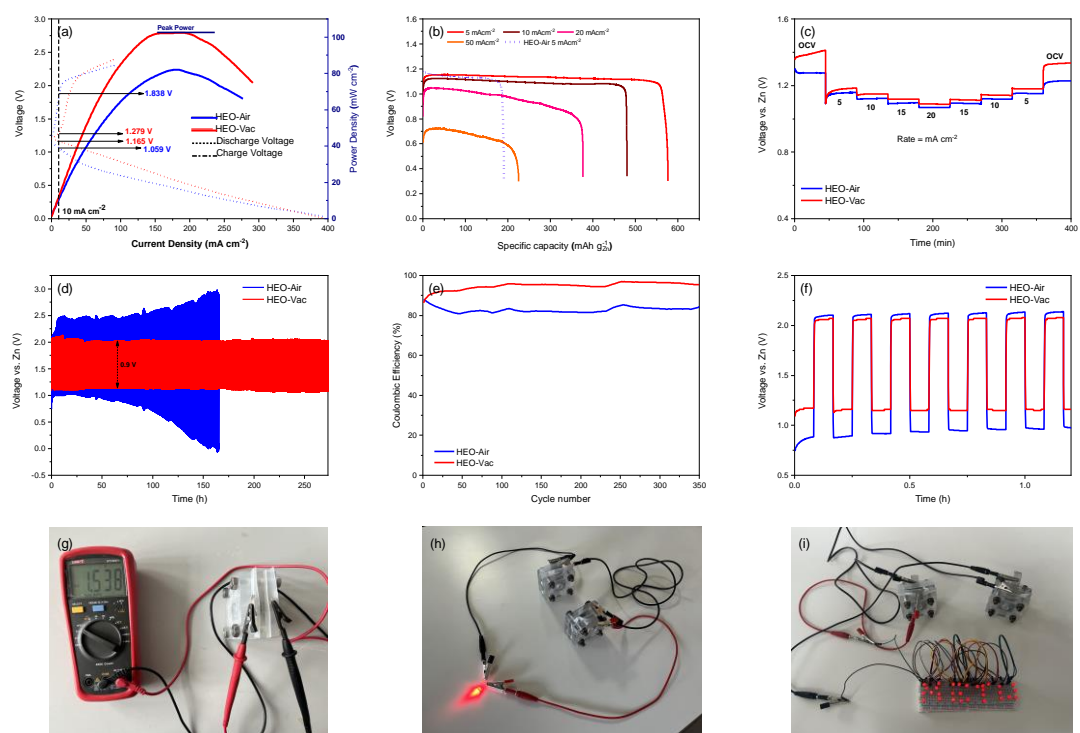


Figure 4.12 HEO-Air and HEO-Vac based Zn-air battery's (a) charge and discharge polarization curves and peak power density plots (b) specific capacities at 5, 10, 20, and 50 mA cm⁻² current densities (c) rate capability study (d) cyclic charge-discharge curves (e) coulombic efficiencies (f) durability performance over the first seven cycles of cyclic charge-discharge (g) open circuit voltage of the HEO-Vac based Zn-air battery, and (h-i) digital photographs of the operating HEO-Vac based Zn-air battery.

CHAPTER 5

RESULTS AND DISCUSSION FOR NANOPOROUS (FeCrCoMnZn)₃O_{4-δ} HIGH ENTROPY OXIDE ELECTROCATALYSTS

5.1 Crystal Structure and Morphology of Nanoporous HEOs

The crystal structures of the nanoporous HEO electrocatalysts were examined with XRD. Figure 5.1 shows the XRD patterns of nanoporous HEO electrocatalysts. The analysis of these patterns shows us that all nanoporous HEOs are single-phase. To further explore the impact of the porosity on the lattice structure, Rietveld Refinement analysis was conducted for GLY500, GLY600, and GLY700, as illustrated in Figures 5.2(b,c,d), respectively. Nanoporous HEOs demonstrate spinel cubic crystal structures with the space group $Fd\bar{3}m$ (ICDD #04-024-0120). The lattice parameters were measured as 8.3721 Å for GLY500, 8.3634 Å for GLY600, and 8.3684 Å for GLY700.

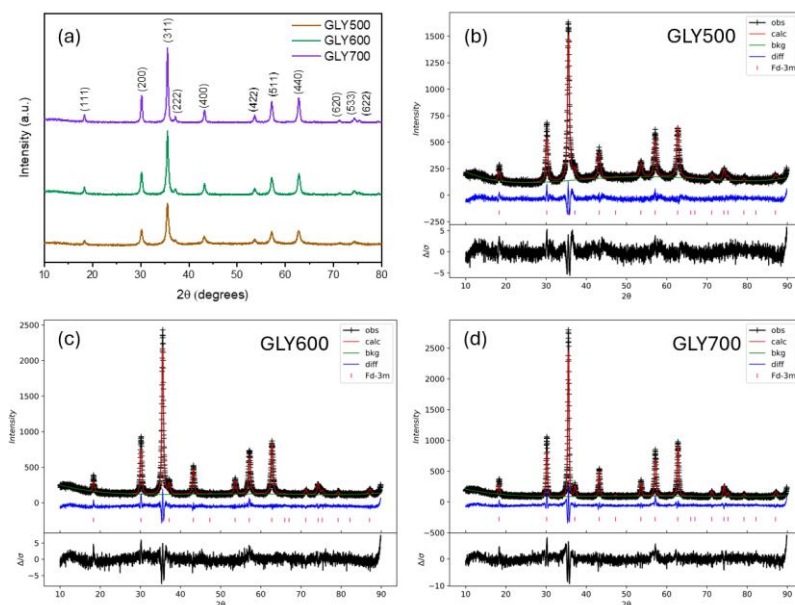


Figure 5.1 (a) XRD patterns of GLY500, GLY600, and GLY700 nanoporous HEOs. Rietveld refinement analysis of (b) GLY500 (c) GLY600 (d)GLY700

The morphology of the synthesized nanoporous HEOs was examined using SEM, as shown in Figure 5.2. It is clearly seen that all the samples have a porous nature, and a distinct network structure in the samples is evident. HEO particles are connected, and they form a large network system with irregular pore sizes and shapes. All samples display a coral-like structure with ranging pore sizes. The pores formed during the low-temperature sol-gel process result from the escape of large quantities of gases such as CO₂, N₂, and H₂O. For GLY500 HEO sample pore sizes ranging from several nanometers to five micrometers (Figure 5.2(a,b,c,)). For the GLY600 sample average pore size is bigger than GLY500 (Figure 5.2(e,f,g)). As the heat treatment temperature increased smaller pores in the structure were eliminated and bigger pores grew in the structure. This can be attributed to elimination of the gaseous in the sample successfully. On the other hand for GLY700, it can be seen that from Figure 5.2(i,j,k), the average pore size decreases but the pore size becomes more homogeneous. This can be attributed to the high sintering rate in the material. At 700 °C, the diffusion rate is higher, therefore; the sintering process may dominate in the structure, and particles in the sample may start to fuse together which eventually decreases the overall pore size and volume. In addition, we examined the elemental distribution within the nanoporous HEOs using EDS mapping. The EDS mapping results for GLY500, GLY600, and GLY700 samples were presented in Figure 5.2(d,h,l). EDS mapping revealed a uniform distribution of all elements which are Fe, Cr, Co, Mn, Zn, and O throughout the particles for all the nanoporous HEO samples.

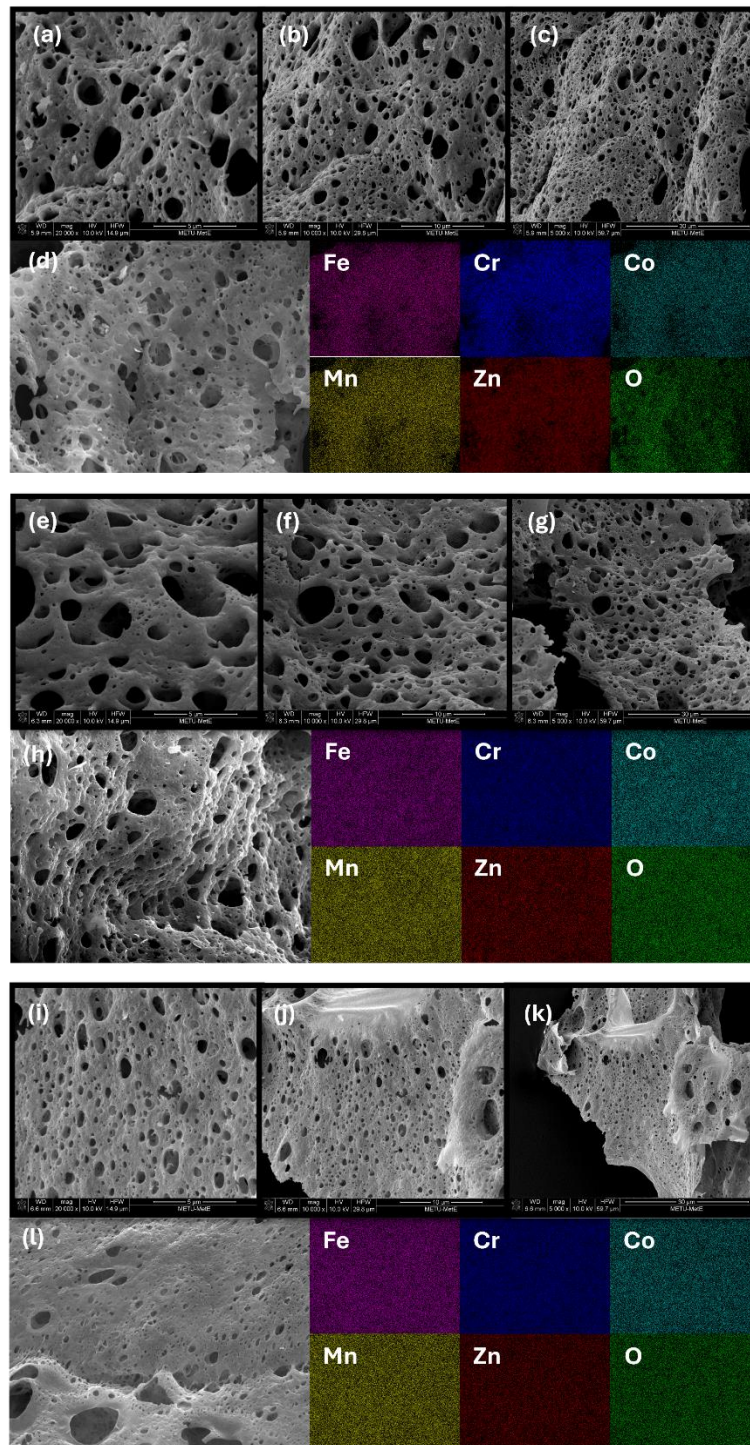


Figure 5.2 SEM images of GLY500 (a) at 20000x magnification (b) at 10000x mag. (c) at 5000x mag. (d) EDS Mapping of GLY500 for Fe, Cr, Co, Mn, Zn, and O. SEM images of GLY600 (e) at 20000x mag. (f) at 10000x mag. (g) at 5000x mag. (h) EDS Mapping of GLY600. SEM images of GLY700 (i) at 20000x mag. (j) at 10000x mag. (k) at 5000x mag. (l) EDS Mapping of GLY700.

We conducted further materials characterizations with HRTEM to examine the crystal structure of the nanoporous HEOs. Figure 5.3(a) shows a BF TEM image and the corresponding SAED pattern from the $\langle 211 \rangle$ zone axis for GLY500 nanoporous HEO. The porous nature of GLY500 particles can be seen clearly in the BF TEM image and the analysis from the $\langle 211 \rangle$ zone axis further confirms GLY500 HEOs spinel cubic crystal structure. In addition, HRTEM analysis reveals lattice fringes which show us the crystalline structure of GLY500 nanoporous HEO. FFT data obtained from this crystal in the $\langle 211 \rangle$ zone axis corresponds to the $Fd\bar{3}m$ (227) space group (Figure 5.3(b)). HRTEM analysis confirms the spinel cubic crystal structure of GLY500 which is comparable with the Rietveld analysis conducted on the XRD data. HRTEM analysis of GLY500 is also comparable with the analysis presented in Chapter 4 Section 4.1 of this thesis. The crystal structure of the $(\text{FeCrCoMnZn})_3\text{O}_{4-\delta}$ HEO doesn't change when it is produced with the pore-forming aging process. The GLY600 powders were subjected to similar analyses using HRTEM. Figure 5.3(c) presents the BF TEM image and the corresponding SAED pattern from the $\langle 211 \rangle$ zone axis for the GLY600 nanoporous HEO powders, revealing a particle size of approximately 450 nm with a porous nature. The SAED pattern for GLY600 verifies the $Fd\bar{3}m$ (227) symmetry determined with Rietveld refinement of the XRD results. Additionally, Figure 5.3(d) displays the HRTEM image and the corresponding FFT pattern from the $\langle 211 \rangle$ zone axis, further confirming the spinel cubic crystal structure. HRTEM analyses were conducted for the GLY700 powders. Figure 5.3(e) presents a BF TEM image with the corresponding SAED pattern from the $\langle 211 \rangle$ zone axis. BF TEM image of GLY700 also shows the porous structure of the HEO powders. The SAED pattern confirms the $Fd\bar{3}m$ (227) symmetry. Figure 5.3(f) displays the HRTEM image and the associated FFT pattern from the $\langle 211 \rangle$ zone axis which further confirms the spinel cubic crystal structure of GLY700 powders. As a result, all of the nanoporous HEO particles have spinel cubic structures, and there is no amorphization due to the pore-forming aging process.

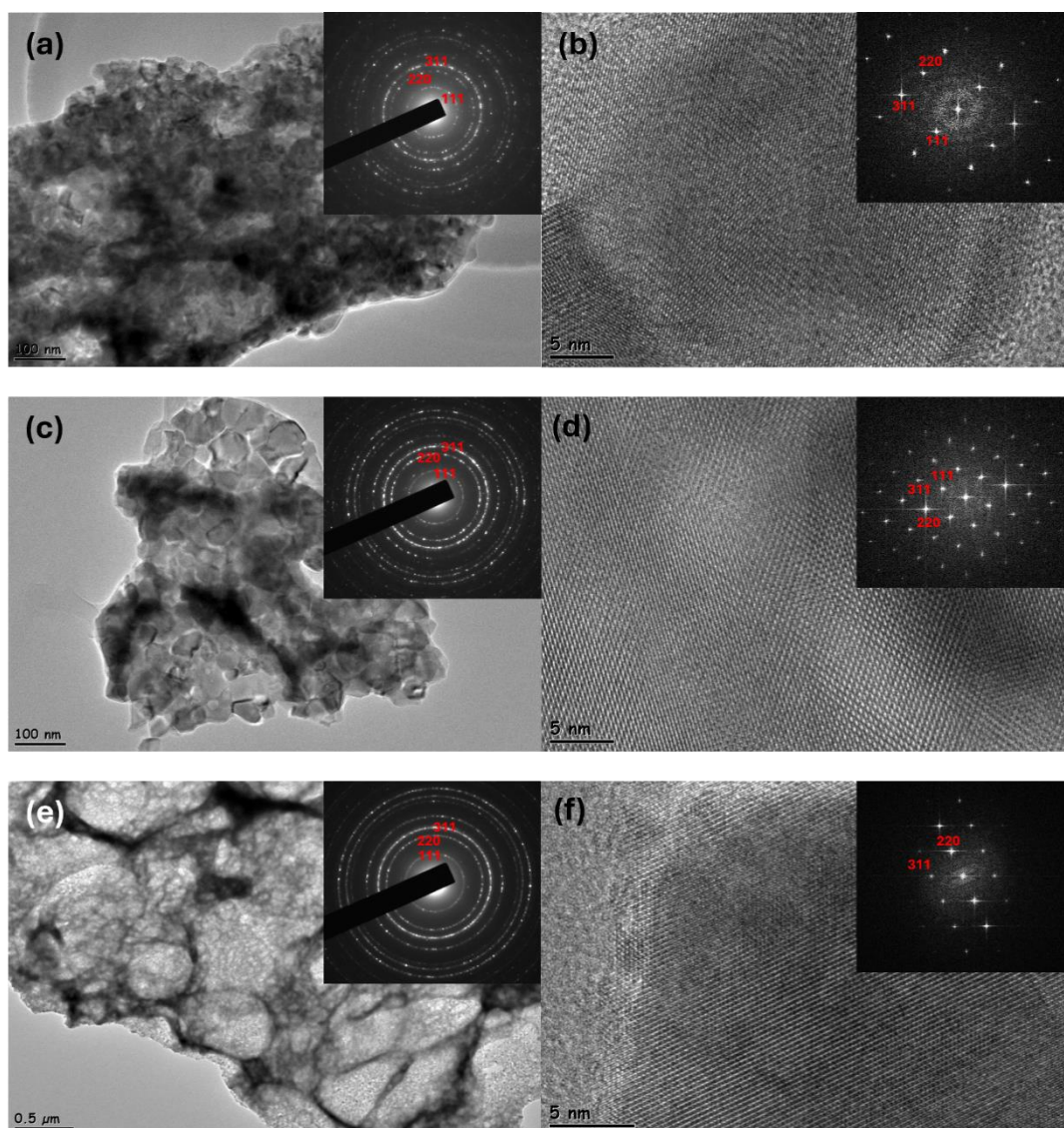


Figure 5.3 (a) BF TEM image of GLY500 and the inset shows the SAED pattern (b) HRTEM image of GLY500 and the inset shows the FFT pattern (c) BF TEM image of GLY600 and the inset shows the SAED pattern (d) HRTEM image of GLY600 and inset shows the FFT pattern (e) BF TEM image of GLY700 and the inset shows the SAED pattern (f) HRTEM image of GLY700 and the inset shows the FFT pattern

5.2 Electronic Structure of Nanoporous HEOs

XPS was employed to analyze the surface chemical composition and the chemical states of the elements in the nanoporous HEO electrocatalysts. Figure 5.2 displays the XPS core level spectra and the corresponding deconvolution of the Fe 2p, Co 2p,

Cr 2p, Mn 2p, and Zn 2p. In the Fe 2p XPS core level spectra for GLY500, GLY600, and GLY700, the presence of the Fe (III) Fe 2p_{3/2} satellite peak located at a binding energy of ≈ 720 eV indicates the presence of Fe₂O₃ (Figure 5.4(a)). Additionally, the Fe 2p XPS core level spectra also display peaks at binding energies of 732 eV, 724 eV, and 711 eV, corresponding to Fe (III) Fe 2p_{1/2} satellite, Fe 2p_{1/2}, and Fe 2p_{3/2}, respectively. This confirms that iron exists in the Fe³⁺ oxidation state in the structure for all samples. Figure 5.4(b) displays the Co 2p XPS core level spectra for nanoporous HEOs. For the GLY500 sample, the Co 2p XPS spectra show Co 2p_{1/2} and Co 2p_{3/2} peaks at binding energies of 795 eV and 780 eV, respectively. These peak positions indicate the presence of Co₃O₄, suggesting that both Co²⁺ and Co³⁺ oxidation states are present in the structure of the GLY500 HEO. On the other hand, in the Co 2p XPS core level spectra for GLY600, and GLY700 peaks at binding energies of 802 eV for the Co 2p_{1/2} satellite, 795 eV for Co 2p_{1/2}, 785 eV for the Co 2p_{3/2} satellite, and 780 eV for Co 2p_{3/2} are observable. Strong satellites in Co 2p XPS spectra indicate that Co is present in the Co²⁺ oxidation state in the GLY600, and GLY700 HEO samples. In Figure 5.4(c), the Cr 2p XPS core level spectra are illustrated. In GLY500 Cr 2p spectra, Cr 2p_{1/2} and Cr 2p_{3/2} peaks located at 585 eV, and 576 eV binding energies are observable. Peak splitting exists in the Cr 2p_{1/2} and Cr 2p_{3/2} peaks, therefore; chromium is present both in Cr³⁺ and Cr⁶⁺ oxidation states in the GLY500 HEO electrocatalyst as shown in the deconvolution in Figure 5.4(c). For GLY600 and GLY700 samples Cr 2p XPS core level spectra show peaks at 585 eV and 576 eV, corresponding to the Cr 2p_{1/2} and Cr 2p_{3/2} signals, respectively. These peaks confirm the presence of Cr³⁺ in the GLY600 and GLY700 HEO electrocatalysts. The XPS results in Figure 5.4(d) show the Mn 2p XPS core level spectra with peaks at binding energies of 653 eV and 641 eV, corresponding to Mn 2p_{1/2} and Mn 2p_{3/2}, respectively, indicating the presence of Mn₂O₃ in all samples. Additionally, the Zn 2p core level spectra in Figure 5.4(e) reveal the Zn²⁺ oxidation state in all samples, with Zn 2p_{1/2} and Zn 2p_{3/2} peaks at binding energies of 1043 eV and 1020 eV, respectively.

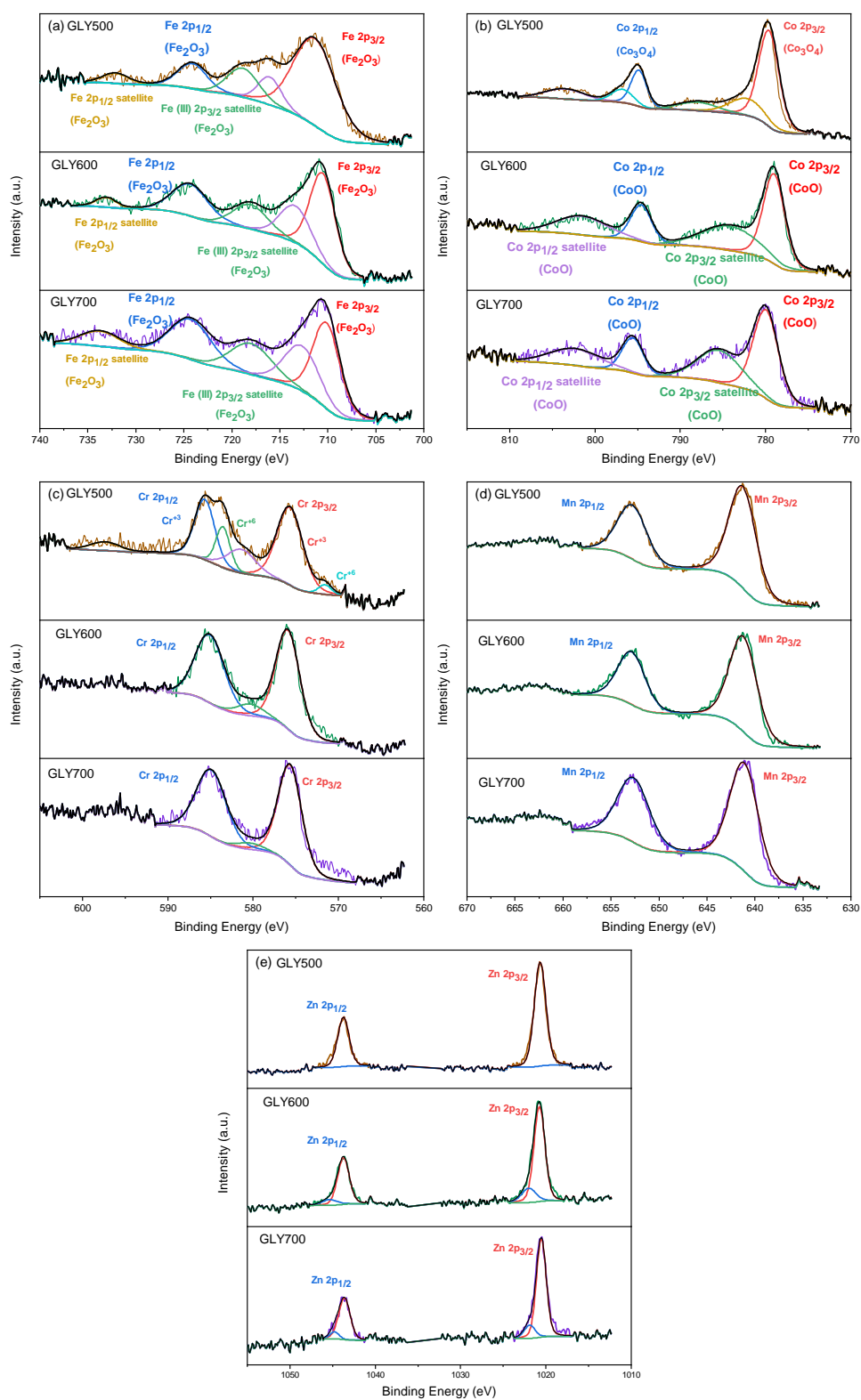


Figure 5.4 XPS core level spectra and corresponding deconvolution of (a) Fe 2p (b) Co 2p (c) Cr 2p (d) Mn 2p, and (e) Zn 2p for GLY500, GLY600, and GLY700

Figure 5.5 shows the fitted O 1s XPS core level spectra for the nanoporous HEO electrocatalysts. The O 1s spectra indicate the presence of oxygen vacancies and lattice oxygen at binding energies of 531 eV and 529 eV, respectively. The oxygen vacancy peak accounts for 23.05%, 38.75%, and 29.10% of the total O 1s XPS spectra peak area for GLY500, GLY600, and GLY700, respectively. In contrast, the lattice oxygen peak constitutes 61.70%, 45.99%, and 57.59% of the total area for GLY500, GLY600 and GLY700, respectively.

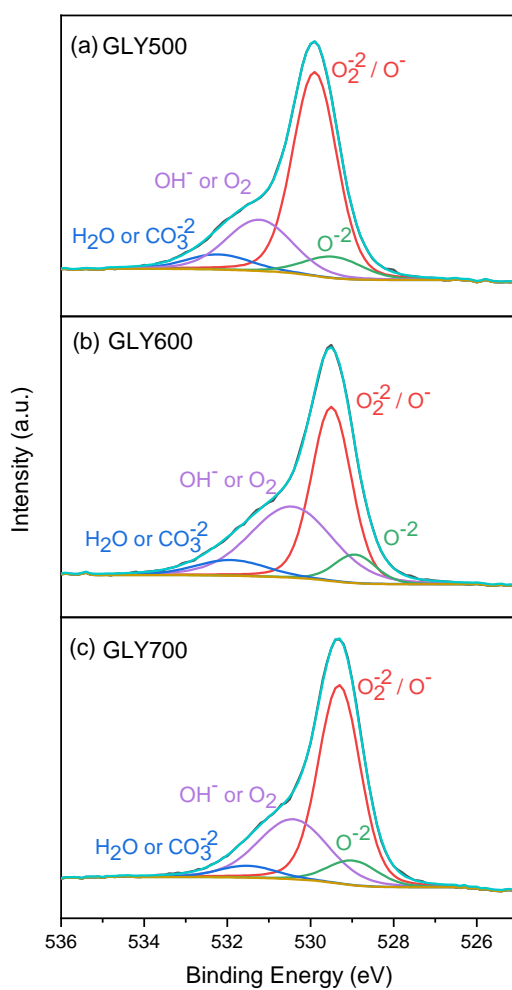


Figure 5.5 O 1s XPS core level spectra for (a) GLY500 (b) GLY600 (c) GLY700

5.3 OER/ORR Performance of Nanoporous HEO Electrocatalysts

To understand the effect of porosity on the bifunctional OER/ORR activity, after the characterization of GLY500, GLY600, and GLY700 HEO powders, a series of electrochemical tests were conducted as discussed in the experimental chapter of this thesis before. Firstly, LSV curves for GLY500, GLY600, and GLY700 powders were obtained. The LSV curves are shown in Figure 5.6(a) At a current density of 10 mA cm^{-2} the overpotential values were measured. The overpotential for GLY500, GLY600, and GLY700 HEO electrocatalysts were found to be 451 mV, 447 mV, and 467 mV, respectively. Therefore, GLY600 has the lowest overpotential among the nanoporous HEO electrocatalysts which can be attributed to its bigger pore size and higher oxygen vacancy content in its structure as compared to others.

To investigate the electrochemical reaction kinetics of the samples, Tafel slopes were determined using the multistep chronoamperometry method. We utilized the multistep chronoamperometry method with incremental voltage steps as we did for HEO-Air and HEO-Vac samples. This test was conducted within the potential range of 0.50 – 0.90 V vs. Ag/AgCl, with an increment of 0.01 V where OER primarily occurs for GLY500, GLY600, and GLY700 HEO electrocatalysts. As shown in Figure 5.6(b), the Tafel slopes for GLY500, GLY600, and GLY700 nanoporous HEO electrocatalysts were calculated as $78.68 \text{ mV dec}^{-1}$, $77.58 \text{ mV dec}^{-1}$, and $81.82 \text{ mV dec}^{-1}$, respectively. Hence, GLY600 has lower Tafel slopes which means its reaction kinetics are faster as compared to GLY500, and GLY700 samples.

EIS was employed to evaluate the charge transfer rate of the electrocatalysts in the same manner we applied to HEO-Air and HEO-Vac electrocatalysts. Figure 5.6(c) presents the fitted EIS data, which includes the R_s , R_{ct} , and CPE (see the series in the index of Figure 5.6(c)). The charge transfer resistance of GLY500, GLY600, and GLY700 are measured at $63.50 \text{ } \Omega$, $73 \text{ } \Omega$ and $107 \text{ } \Omega$.

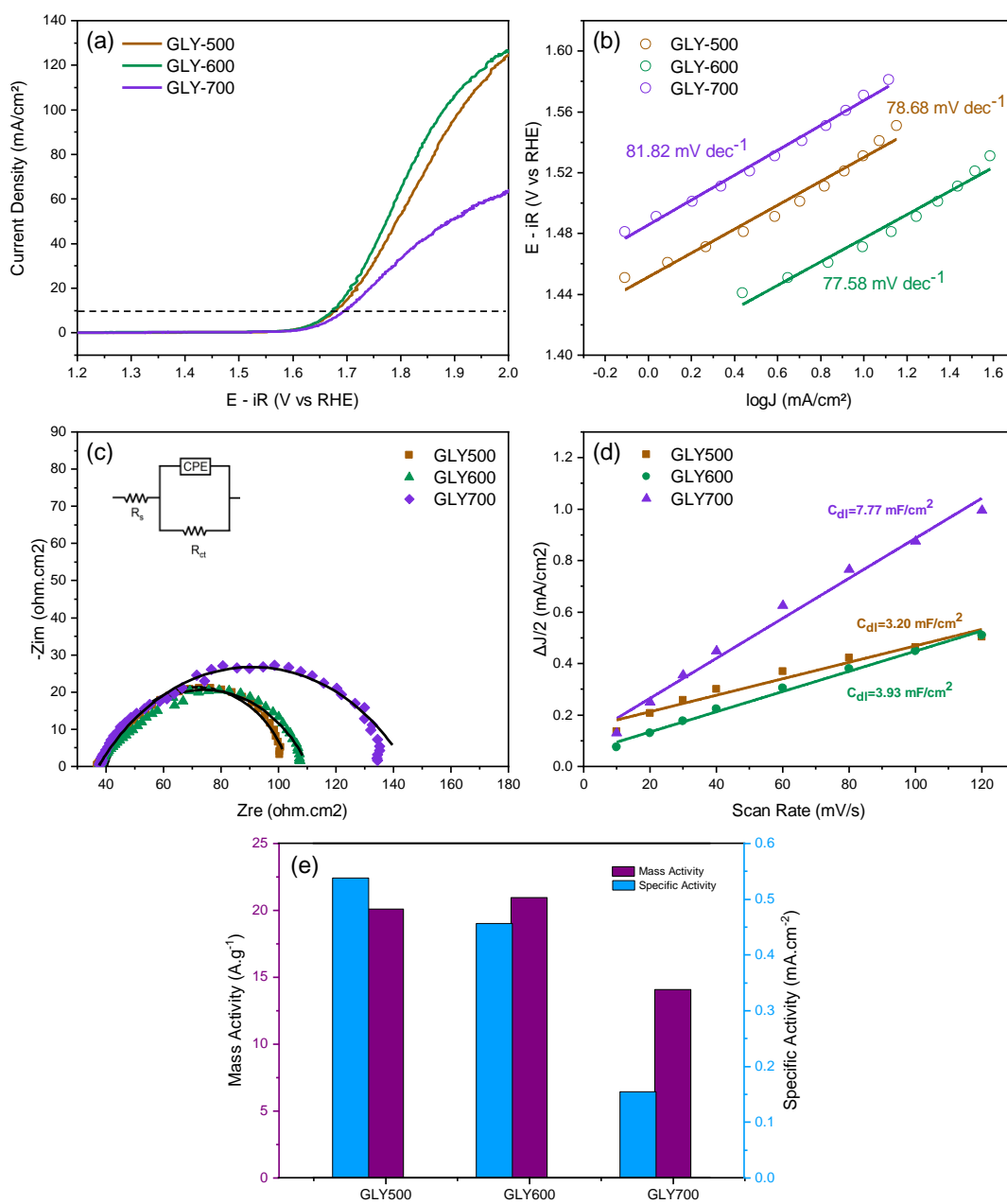


Figure 5.6 GLY500, GLY600 and GLY700 nanoporous HEO electrocatalysts' (a) LSV curves (b) Tafel plots (c) Fitted EIS data (d) Electric double layer capacitance analysis results (e) MA and SA activity calculations

ECSA was calculated using the double-layer capacitance (C_{dl}), obtained from CV measurements conducted at various scan rates within the non-faradaic region as we measured for HEO-Air and HEO-Vac samples explained in the previous chapter. As presented in Figure 5.7, the CVs were performed in a 1 M KOH solution saturated with oxygen, scanning between 0.2 V and 0.3 V vs. Ag/AgCl, at scan rates of 10, 20, 30, 40, 60, 80, 100, and 120 mV s^{-1} for GLY500, GLY600, and GLY700 electrocatalysts. The C_{dl} values for GLY500, GLY600, and GLY700 electrocatalysts were calculated as 3.20 mF cm^{-2} , 3.93 mF cm^{-2} and 7.77 mF cm^{-2} , respectively as shown in Figure 5.6(d). As discussed in Chapter 3.4 of this thesis before, ECSA is determined by dividing C_{dl} by the C_s , where C_s in 1 M KOH is equal to 0.040 mF cm^{-2} . Therefore, for GLY500, GLY600, and GLY700 electrocatalysts ECSA was calculated as 5.6 cm^2 , 6.88 cm^2 , and 13.60 cm^2 , respectively. Hence, the ECSA of the GLY700 is higher than the others.

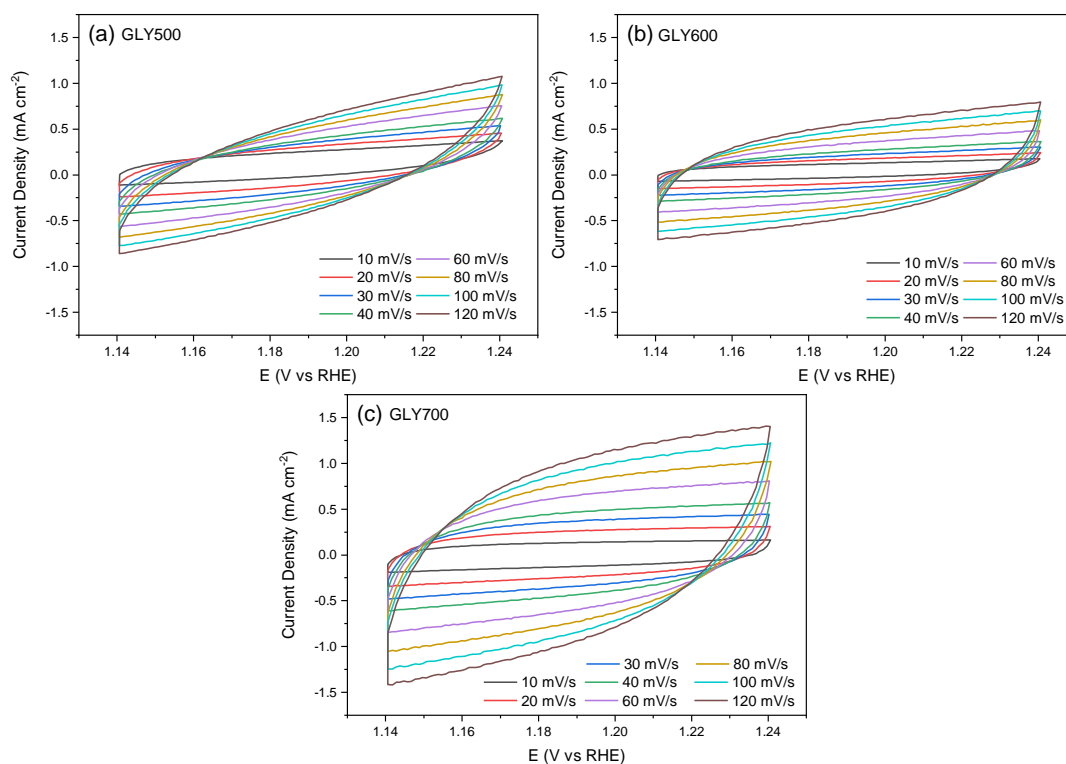


Figure 5.7 CV scans at scan rates 10, 20, 30, 40, 60, 80, 100, and 120 mV s^{-1} for (a) GLY500 (b) GLY600 (c) GLY700

The MA and SA were evaluated to investigate the intrinsic activity of the GLY500, GLY600, and GLY700 electrocatalysts (Figure 5.6(e)). As explained in the experimental section, the mass loading was used to compute the mass activity, while the specific activity was determined using the ECSA. GLY600 nanoporous HEO electrocatalyst demonstrated superior performance compared to the other electrocatalysts in both MA and SA. The MA and SA of GLY600 were quantified at 20.93 A g⁻¹ and 0.46 mA cm⁻², respectively. On the other hand, MAs were calculated as 20.07 and 14.07 A g⁻¹, and SAs were calculated as 0.54 and 0.16 mA cm⁻² for GLY500, and GLY700 respectively.

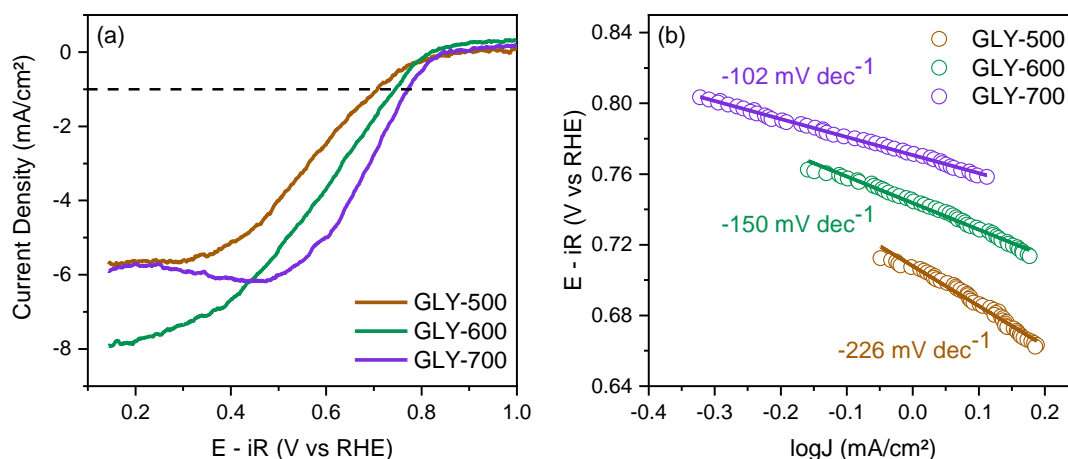


Figure 5.8 GLY500, GLY600 and GLY700 nanoporous HEO electrocatalysts' (a) ORR activity curves (b) Tafel plots

As shown in Figure 5.8, the ORR activity of GLY500, GLY600, and GLY700 was evaluated. From the LSV curves in Figure 5.8(a), the potentials recorded at a current density of -1 mA cm^{-2} for GLY500, GLY600, and GLY700 were 0.71 V, 0.74 V, and 0.77 V, respectively. This indicates that the ORR activity of GLY700 slightly exceeds the ORR activity of GLY600 and GLY500 electrocatalysts. Tafel plots were then used to determine the Tafel slopes, as shown in Figure 5.8(b). The Tafel slopes were calculated as -226 mV dec^{-1} for GLY500, -150 mV dec^{-1} for GLY600, and -102 mV dec^{-1} for GLY700. As discussed in Chapter 4.3, the BI value is calculated based on the potential difference between current densities of -1 mA cm^{-2} and 10 mA cm^{-2} . A lower BI value indicates superior performance in both OER and ORR.

In this thesis, the BI for GLY500, GLY600, and GLY700 were found 0.97, 0.94, and 0.93 respectively. Consequently, the BI of GLY700, and GLY600 are very similar, and they are slightly lower than GLY500 nanoporous HEO electrocatalyst.

5.4 Zn-Air Battery Performance of Nanoporous HEO Electrocatalysts

Rechargeable Zn-Air batteries were assembled with a zinc plate as the anode, GLY500, GLY600, and GLY700 nanoporous HEO's as the air cathodes, and a 6 M KOH electrolyte with 0.2 M Zn(OAc)₂.

Polarization curves that demonstrate the charge and discharge characteristics of Zn-air batteries with nanoporous HEOs as air cathodes are shown in Figure 5.9(a). The Zn-air battery with a GLY600 cathode requires 2.095 V for charging and 1.128 V for discharging to achieve a current density of 10 mA cm⁻². Zn-air batteries with GLY500 and GLY700 air cathodes exhibit larger voltage gaps. Specifically, the GLY500 electrocatalyst based Zn-air battery requires 2.173 V for charging and 1.104 V for discharging, and GLY700 based Zn-air battery requires 2.151 V for charging, and 1.103 V for discharging. Additionally, the Zn-air battery with the GLY600 based cathode demonstrates the highest peak power density, reaching 80 mW cm⁻² at a current density of 133 mA cm⁻². Other nanoporous HEO based Zn-air batteries show diminished peak power densities. GLY500 based Zn-air battery reaches its peak power density of 69 mW cm⁻² at a current density of 116 mA cm⁻², whereas GLY700 based Zn-air battery shows the smallest peak power density of 65 mW cm⁻² at a lower current density of 115 mA cm⁻².

The discharge capacities of GLY500, GLY600, and GLY700 based Zn-air batteries at current densities of 5 mA cm⁻², 10 mA cm⁻², and 20 mA cm⁻² are shown in Figure 5.9(b), Figure 5.9(c), and Figure 5.9(d), respectively. The capacities of Zn-air batteries decrease from 5 mA cm⁻² to 20 mA cm⁻², as expected. Specifically, the Zn-air battery with a GLY600 cathode achieves a capacity of 443.34 mA h at 5 mA cm⁻², 399.27 mA h at 10 mA cm⁻², and 345.78 mA h at 20 mA cm⁻². Although the

GLY500 cathode achieves the highest capacity of 461.04 mA h at 5 mA cm⁻², its capacity decreases more as compared to the GLY600 cathode as the discharge current density increases. As a result, at 10 mA cm⁻², and 20 mA cm⁻² discharge current densities it becomes the second-best electrocatalyst with capacities of 390.60 mA h, and 340.51 mA h, respectively. On the other hand, GLY700 based Zn-air batteries demonstrate the lowest capacities among nanoporous HEO electrocatalysts with 423.88 mA h at 5 mA cm⁻², 385.95 mA h at 10 mA cm⁻², and 243.33 mA h at 20 mA cm⁻². Especially at 20 mA cm⁻² discharge current density GLY700 based Zn-air batteries capacity decreased significantly. This can be attributed to GLY700 electrocatalyst's smaller pore sizes as compared to GLY500, and GLY600. With its bigger pore size which effects its OER/ORR performance positively, GLY600 shows high capacity at different current densities. Moreover, GLY600 maintains stable capacity across different current densities, as its capacity retention is less affected by an increase in current density compared to GLY500, and GLY700.

As illustrated in Figure 5.9(e), by varying the discharge rate from 0 to 20 mA cm⁻² and then returning to 0 mA cm⁻², while monitoring the output voltage the cycling stability and rate capability of GLY500, GLY600, and GLY700 nanoporous HEO electrocatalyst based Zn-air batteries were systematically evaluated. Among the nanoporous HEO based Zn-air batteries, the one with the GLY600 electrocatalyst demonstrated superior rate capability and stability. Initially, the output voltage for the GLY600 electrocatalyst was 1.44 V, and after 400 minutes of operation, it decreased to 1.31 V, retaining 90.97% of the initial output voltage. For GLY500 based Zn-air battery initial output voltage was 1.52 V, and final output voltage was 1.35 V. Although for GLY500 based Zn-air battery's initial and final output voltages were higher as compared to GLY600, its voltage decrease was also higher with a voltage retention of 88.82%. In addition, GLY700 based Zn-air battery exhibits an initial output voltage of 1.43 V, after 400 minutes of operation its output voltage decreases to 1.21 V with a retention of 84.6%. As shown in Figure 5.9(e) between 135th to 180th minutes of operation, when the discharge current density is 15 mA cm⁻², GLY700 based Zn-air battery shows nearly 1.10 V output voltage. After a while

between the 225th to 270th minutes of operation, when it is discharged at 15 mA cm⁻² current density again, the output voltage starts from 1.08 V, and it decreases suddenly to 1.01 V. As a result, it can be concluded that GLY700 based Zn-air battery may not be reliable at high current densities, and longer operation times. Notably, the GLY600 electrocatalyst exhibited the least voltage decay after 400 minutes of operation under varying discharge current densities compared to other nanoporous HEO based Zn-air batteries.

The cyclic charge-discharge performance of GLY500, GLY600, and GLY700 based Zn-air batteries are shown in Figure 5.9(g). Cyclic charge-discharge performance was evaluated at a constant current density of 5 mA cm⁻² with 5-minute charge and discharge intervals to evaluate the electrochemical durability of the electrocatalysts. Initially, the GLY700 based Zn-air battery displayed charge and discharge voltages of 2.00 V and 1.19 V, respectively, resulting in a voltage gap of only 810 mV. In comparison, GLY500, and GLY600 had voltage gaps of 840 mV, and 857 mV, respectively, as shown in Figure 5.9(f). Specifically, the initial charge and discharge voltages for the GLY500-based Zn-air battery were 2.03 V and 1.19 V, respectively, while for the GLY600-based Zn-air battery, they were 2.02 V and 1.17 V, respectively. Hence, the GLY700 based Zn-air battery exhibited the smallest voltage gap at the beginning of the cyclic charge-discharge test. However, over time its voltage gap started to increase, and GLY600 based Zn-air battery's voltage gap became the lowest among the other nanoporous HEO based Zn-air batteries. Moreover, after 715 hours of operation GLY700 based Zn-air battery lost its stability. Then, nearly after 768 hours of operation GLY500 based Zn-air battery lost its stability too. However, after more than 1000 hours of cyclic charge-discharge operation, GLY600 based Zn-air battery succeeds in maintaining its stability with minimal increase in its voltage gap. Even after this extended period, the voltage gap of the GLY600 based Zn-air battery increased by only 14% from the initial value after 1030 hours, reaching 970 mV.

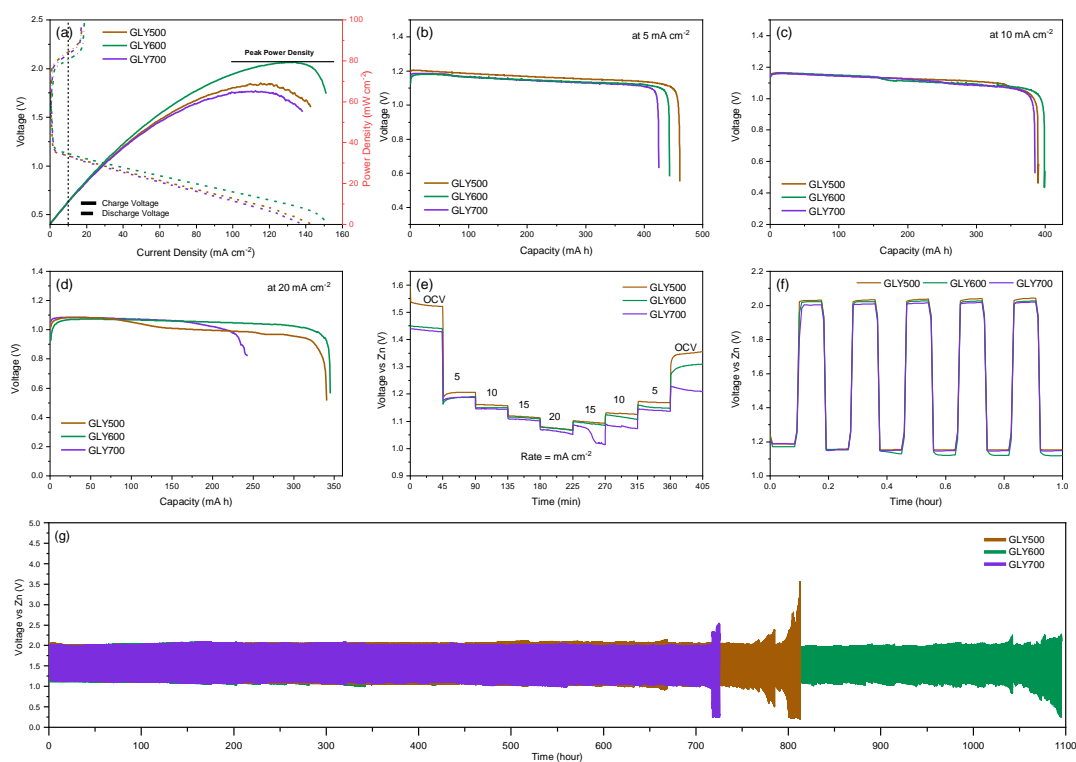


Figure 5.9 Zn-air batteries with nanoporous GLY500, GLY600, and GLY700 HEO electrocatalysts (a) Peak power density plots along with charge and discharge polarization curves (b) Capacities at a current density of 5 mA cm⁻² (c) Capacities at a current density of 10 mA cm⁻² (d) Capacities at a current density of 20 mA cm⁻² (e) Rate capability study from 0 to 20 mA cm⁻² and back to 0 mA cm⁻² (f) Durability performance during the first hour of cyclic charge-discharge (g) Cyclic charge-discharge performance at 5 mA cm⁻²

CHAPTER 6

RESULTS AND DISCUSSION FOR $\text{NdBaCo}_a\text{Fe}_{2-a}\text{O}_{5+\delta}$ ($a = 1.0, 1.4, 1.6, 1.8$) DOUBLE PEROVSKITE OXIDE ELECTROCATALYSTS

“This chapter contains information used with the permission of JOHN/WILEY & SONS LTD. from “B-site Doping Boosts the OER and ORR Performance of Double Perovskite Oxide as Air Cathode for Zinc-Air Batteries”, Cagla Ozgur, Tuncay Erdil, Uygur Geyikci, Ilker Yildiz, Ersu Lokcu, Cigdem Toparli, ChemPhysChem: e202400531”

6.1 Crystal Structure and Morphology of NBCF Electrocatalysts

To investigate the crystal structures of NBCF double perovskite oxides XRD analysis was conducted. Figure 6.1 demonstrates the XRD patterns and the results of the Rietveld Refinement analysis. The XRD patterns in Figure 6.1(a) clearly show that all NBCF double perovskite oxides are single-phased. There were not any evident peaks related to oxides or hydroxides of Nd, Ba, Co, Fe, or any other impurities. Additionally, the structural properties, such as lattice parameters, space groups, and crystal structures, were determined using Rietveld Refinement analysis. The results show that both CoFe and Co_{1.4}Fe_{0.6} have an orthorhombic crystal structure with a space group of *Pmmm*. As the cobalt content increases and the iron content decreases in the NBCF double perovskite oxide's structure, the crystal structure changes to a tetragonal with the space group of *P4/mmm*. In Table 6.1, the lattice parameters and total crystal volumes for the NBCF double perovskite oxides are tabulated. As demonstrated in Table 6.1, CoFe has larger lattice parameters as compared to other double perovskite oxides and a total crystal volume of 118.47 Å³, while Co_{1.8}Fe_{0.2} shows smaller lattice parameters and a volume of 116.17 Å³. The increased iron content in the structure leads to more lattice distortion, attributed to

the larger ionic size of iron, which results in a higher total crystal volume for the Co_{1.8}Fe_{0.2} double perovskite oxide.

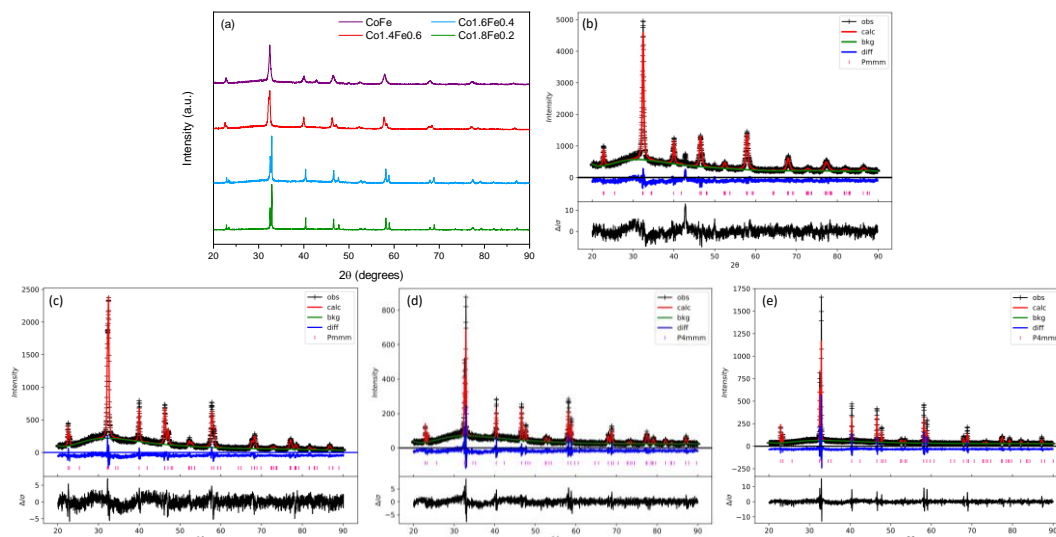


Figure 6.1 (a) XRD patterns of NBCF double perovskite oxides. Rietveld refinement analysis for (b) CoFe (c) Co_{1.4}Fe_{0.6} (d) Co_{1.6}Fe_{0.4} and (e) Co_{1.8}Fe_{0.2}

Table 6.1 Lattice parameters, crystal volume, crystal structure and space group for CoFe, Co_{1.4}Fe_{0.6}, Co_{1.6}Fe_{0.4} and Co_{1.8}Fe_{0.2}

	a	b	c	Crystal Volume	Crystal Structure	Space Group
CoFe	3.90908	3.90284	7.76516	118.47	Orthorhombic	Pmmm
Co_{1.4}Fe_{0.6}	3.90752	3.90533	7.68501	117.27	Orthorhombic	Pmmm
Co_{1.6}Fe_{0.4}	3.90198	3.90198	7.64396	116.38	Tetragonal	P4/mmm
Co_{1.8}Fe_{0.2}	3.90304	3.90304	7.62614	116.17	Tetragonal	P4/mmm

We analyzed the morphology of the synthesized NBCF double perovskite oxides using scanning electron microscopy (SEM), as illustrated in Figure 6.2. The SEM images revealed particles at the submicron scale, typically ranging in size from several hundred nanometers. Although there was some variation in particle shape

and size, overall consistency was observed across all perovskite oxides. This suggests that any potential influence of particle size and morphology on electrocatalytic activity is likely insignificant. Additionally, we investigated the elemental distribution within the double perovskite oxides using energy-dispersive X-ray (EDX) mapping. The results of the EDX mapping for NBCF double perovskite oxides, shown in Figure 6.2, demonstrated a uniform distribution of all elements (Nd, Ba, Co, Fe, and O) throughout the particles.

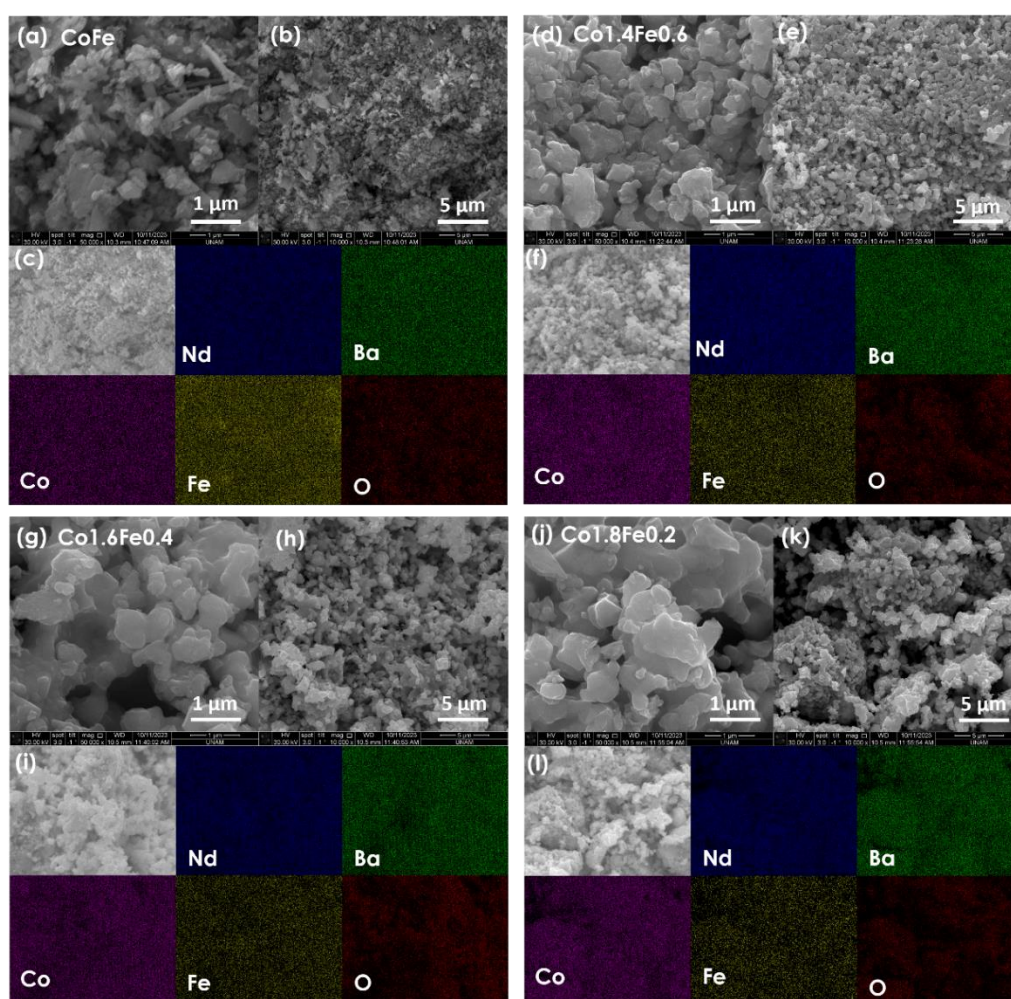


Figure 6.2 SEM images of CoFe (a) at 50000x magnification (b) at 10000x mag. (c) EDS Mapping of CoFe for Nd, Ba, Co,Fe, and O. SEM images of Co_{1.4}Fe_{0.6} (d) at 50000x mag. (e) at 10000x mag. (f) EDS Mapping of Co_{1.4}Fe_{0.6}. SEM images of Co_{1.6}Fe_{0.4} (g) at 50000x mag. (h) at 10000x mag. (i) EDS Mapping of Co_{1.6}Fe_{0.4} SEM images of Co_{1.8}Fe_{0.2} (j) at 50000x mag. (k) at 10000x mag. (l) EDS Mapping of Co_{1.8}Fe_{0.2}

6.2 Electronic Structure of NBCF Electrocatalysts

X-ray Photoelectron Spectroscopy (XPS) was utilized to investigate the surface chemical composition and chemical states of the elements within the NBCF double perovskite oxide electrocatalysts. The XPS core level spectra and the corresponding deconvolution of Fe 2p and Co 2p peaks are shown in Figure 6.3. In Figures 6.3(a) and 6.3(c), the presence of the Fe (III) 2p_{3/2} satellite is evident which indicates Fe₂O₃. Therefore, for CoFe and Co_{1.4}Fe_{0.6}, iron is present in both Fe⁺² and Fe⁺³ oxidation states in the structure [16]. However, in the Fe 2p XPS core level spectra of Co_{1.6}Fe_{0.4} and Co_{1.8}Fe_{0.2} which are shown in Figure 6.3(e) and 6.3(g), the Fe (III) 2p_{3/2} satellite is absent. On the other hand, Fe (II) 2p_{3/2} satellite which indicates FeO is observed in the XPS core level spectra [164]. This suggests a decrease in the oxidation state of iron to Fe⁺² as the iron content in the NBCF double perovskite oxide decreases. Meanwhile, in Figure 6.3(b,d,f,h) the Co 2p XPS core level spectra which have Co 2p_{3/2} and Co 2p_{1/2} peaks located at 780 eV and 796 eV binding energies, respectively are illustrated. The peak locations in Co 2p spectra indicate the existence of Co₃O₄, hence; Co presents both Co⁺² and Co⁺³ oxidation states in the structure of NBCF double perovskite oxides. As a result, Co 2p XPS spectra of NBCF electrocatalysts suggest that all samples have the same Co oxidation state.

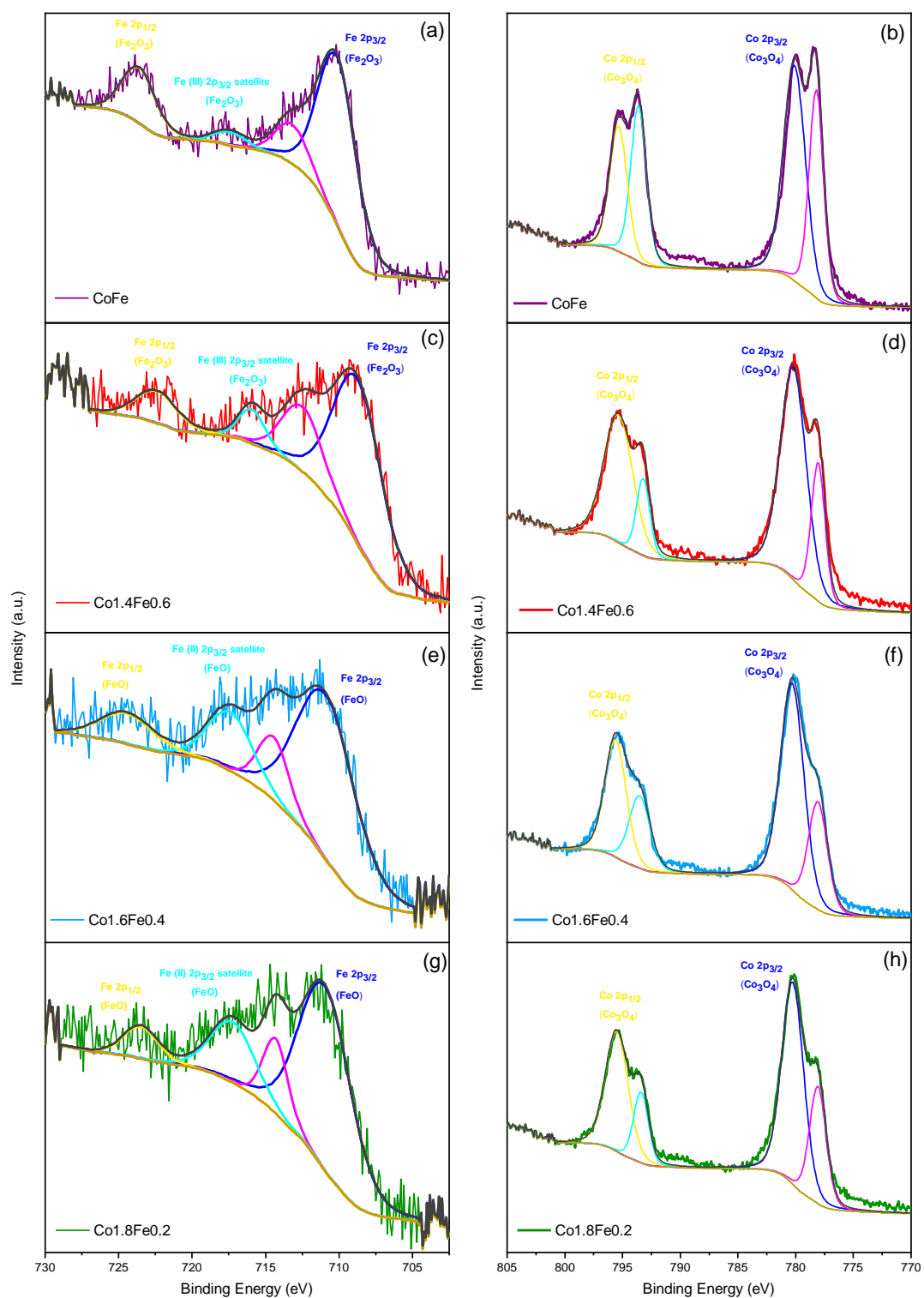


Figure 6.3 XPS core level spectra and corresponding deconvolution of Fe 2p and Co2p respectively for (a,b) CoFe (c,d) Co_{1.4}Fe_{0.6} (e,f) Co_{1.6}Fe_{0.4} (g,h) Co_{1.8}Fe_{0.2}

Figure 6.4 presents the fitted O 1s XPS core level spectra for the NBCF double perovskite oxide electrocatalysts. O 1s spectra reveal the presence of oxygen vacancy and lattice oxygen at binding energies of 531 eV and 529 eV, respectively. The oxygen vacancy peak contributes to 46.57%, 58.40%, 59.78%, and 57.65% of the total O 1s XPS spectra peak area for CoFe, Co_{1.4}Fe_{0.6}, Co_{1.6}Fe_{0.4}, and Co_{1.8}Fe_{0.2}, respectively. In contrast, the lattice oxygen peak covers 37.45%, 26.37%, 23.34%, and 27.51% of the total area for the CoFe, Co_{1.4}Fe_{0.6}, Co_{1.6}Fe_{0.4}, and Co_{1.8}Fe_{0.2}, respectively. Thus, with an increase in the cobalt content in the NBCF double perovskite oxide, the oxidation state of iron shifts from +3 to +2, while the oxidation state of cobalt remains constant. Consequently, there is a rise in the concentration of oxygen vacancies within the structure.

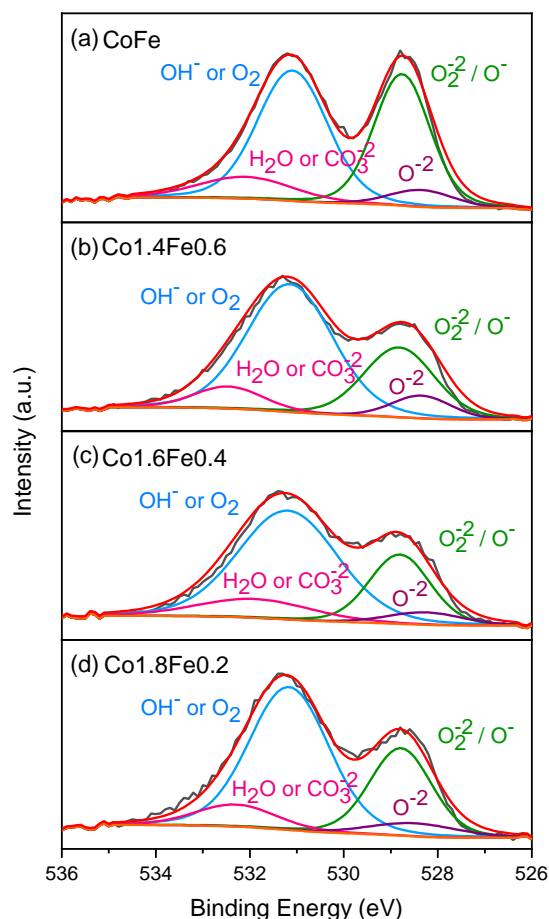


Figure 6.4 O 1s XPS core level spectra for (a) CoFe (b) Co_{1.4}Fe_{0.6} (c) Co_{1.6}Fe_{0.4} (d) Co_{1.8}Fe_{0.2}

6.3 OER/ORR Performance of NBCF Electrocatalysts

To evaluate the electrocatalytic OER/ORR performance of the NBCF electrocatalysts, RDE with a standard three-electrode system was utilized, as detailed in Section 2.3. The electrochemical bifunctional performance of the NBCF electrocatalysts was investigated with the similar procedures that we follow for HEO-Air and HEO-Vac electrocatalysts detailed in Chapter 3. Firstly, LSV tests were performed with an Ag/AgCl reference electrode, and the obtained potentials were converted according to the RHE scale. The geometric area of the glassy carbon electrode is measured as 0.0707 cm^2 and it was used to standardize the LSV profiles (Figure 6.5(a)). Notably, the overpotential values of the NBCF electrocatalysts were found at a current density of $10 \text{ mA}\cdot\text{cm}^{-2}$. The overpotential values for the NBCF electrocatalysts are 439 mV for CoFe, 384 mV for Co_{1.4}Fe_{0.6}, 428 mV for Co_{1.6}Fe_{0.4}, and 444 mV for Co_{1.8}Fe_{0.2}. It is evident from this analysis that Co_{1.4}Fe_{0.6} exhibits the lowest overpotential among the NBCF electrocatalysts. Moreover, the overpotential values for the NBCF electrocatalysts are comparable with the previously reported benchmark bifunctional electrocatalysts [8,160,165,166]. Additionally, Tafel plots were obtained to compare the reaction kinetics of NBCF electrocatalysts, as shown in Figure 6.5(b). The Tafel slopes are determined as 106 mV dec^{-1} for CoFe, 83 mV dec^{-1} for Co_{1.4}Fe_{0.6}, 86 mV dec^{-1} for Co_{1.6}Fe_{0.4}, and 96 mV dec^{-1} for Co_{1.8}Fe_{0.2}. Although Co_{1.4}Fe_{0.6} displays a lower Tafel slope which indicates faster reaction kinetics, it is notable that the Tafel slopes of NBCF electrocatalysts are comparable. It suggests a high degree of similarity in the electrocatalysts' reaction kinetics. Furthermore, the charge transfer rate of the NBCF electrocatalysts was evaluated using EIS. The EIS results in Figure 6.5(c) clearly demonstrate that the conductivity of the Co_{1.8}Fe_{0.2} exceeds the other NBCF electrocatalysts' conductivity. This enhanced conductivity exhibited by the Co_{1.8}Fe_{0.2} highlights its improved charge transfer rate during the OER. Although the Co_{1.8}Fe_{0.2} electrocatalyst shows a slightly higher overpotential than the other NBCF counterparts, its charge transfer rate is a prominent feature.

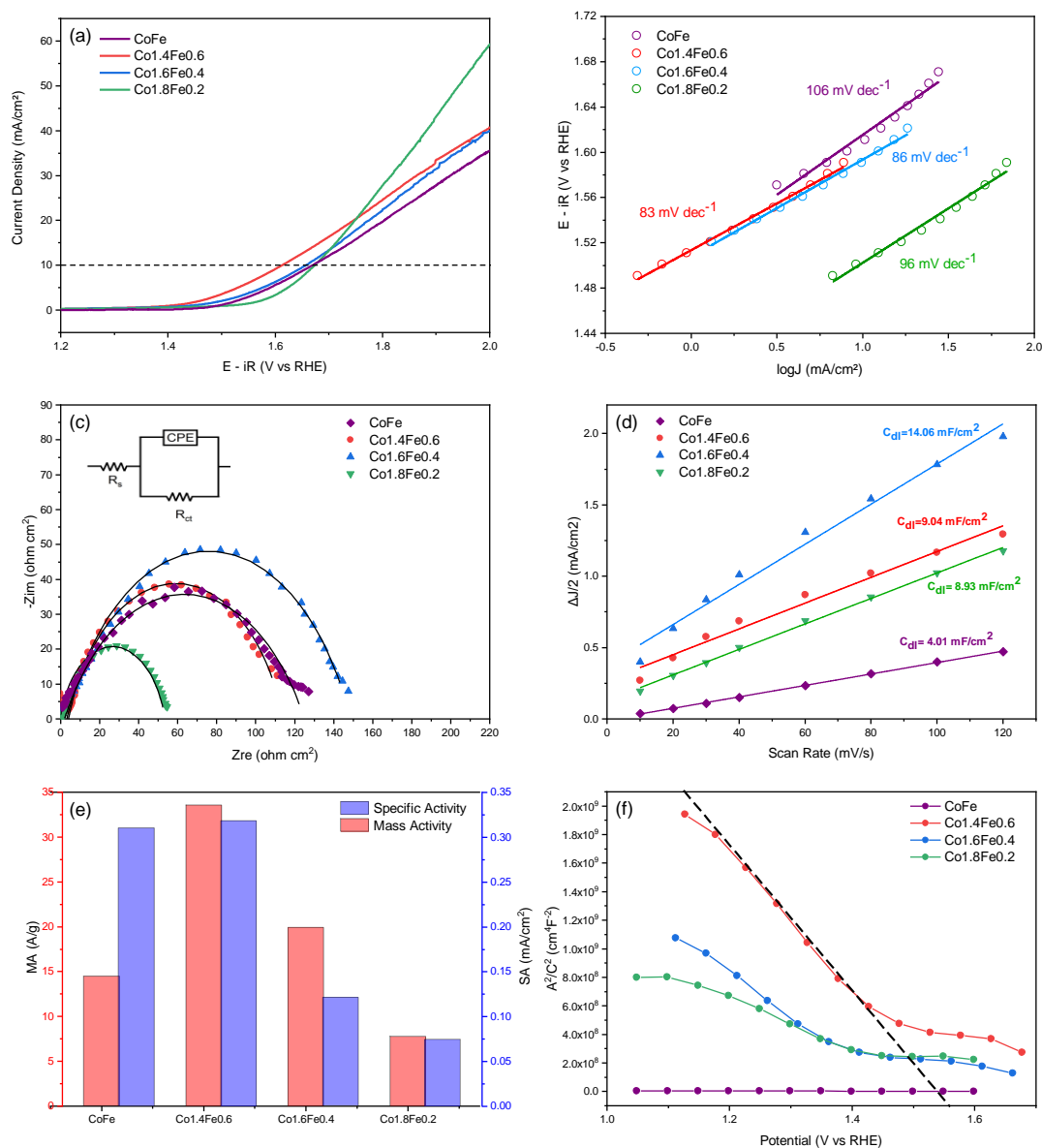


Figure 6.5 For CoFe, Co_{1.4}Fe_{0.6}, Co_{1.6}Fe_{0.4} and Co_{1.8}Fe_{0.2} double perovskite oxide electrocatalysts (a) LSV curves in OER region (b) Tafel plots (c) EIS data with corresponding electrical circuit (d) Electric double layer capacitance measurements (e) MA and SA analysis (f) Mott-Schottky plots

ECSA for NBCF electrocatalysts is determined with the C_{dl} which is calculated from CV experiments conducted at different scan rates from 10 to 120 mV s^{-1} current density. CV measurements are performed in the non-faradaic region between 0.2 V to 0.3 V vs. Ag/AgCl as illustrated in Figure 6.6. The calculated C_{dl} values for CoFe, Co_{1.4}Fe_{0.6}, Co_{1.6}Fe_{0.4}, and Co_{1.8}Fe_{0.2} are determined as 4.01, 9.04, 14.06, and 8.93 mF cm^{-2} , respectively (Figure 6.5(d)). Hence, Co_{1.6}Fe_{0.4} better than the other electrocatalysts in terms of ECSA, indicating its larger electrochemically active surface area. Remarkably, the ECSA analysis implies that the enhanced electrocatalytic performance of Co_{1.4}Fe_{0.6} is not only attributed to its ECSA; rather, it may be correlated to its intrinsic activity.

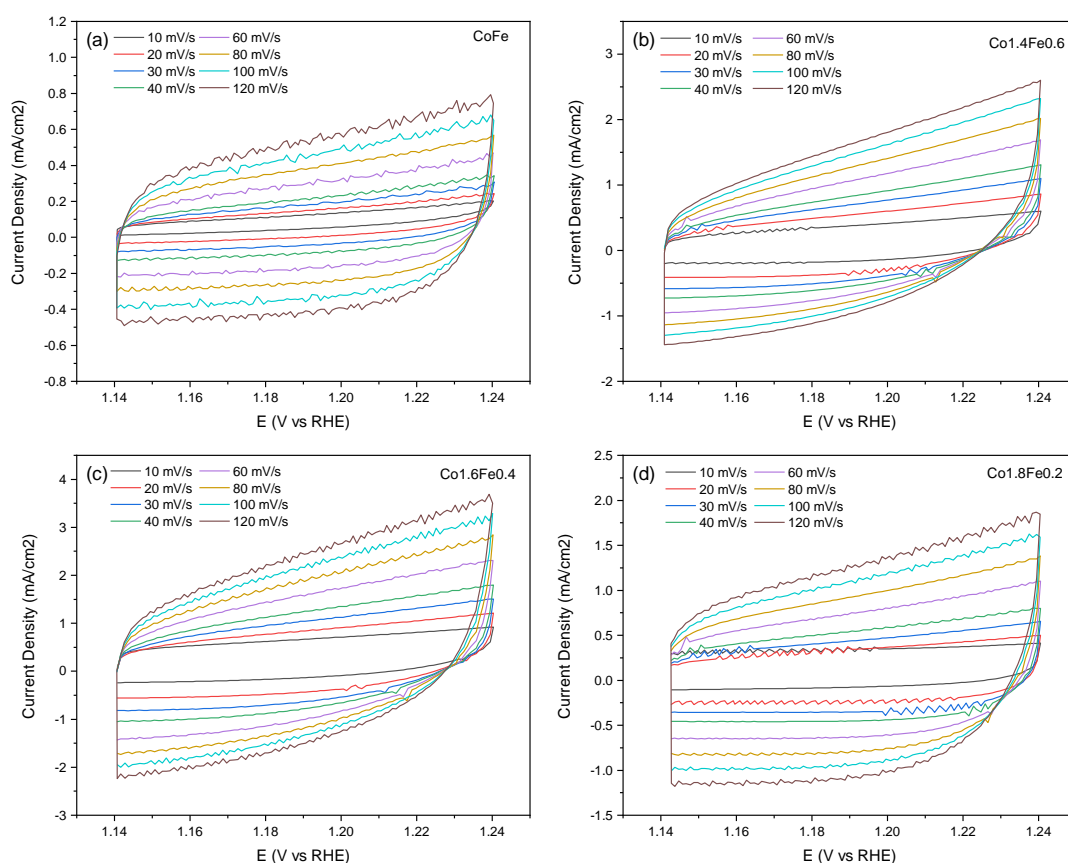


Figure 6.6 CV scans conducted at scan rates of 10, 20, 30, 40, 60, 80, 100, and 120 mV s^{-1} for a) CoFe (b) Co_{1.4}Fe_{0.6} (c) Co_{1.6}Fe_{0.4} (d) Co_{1.8}Fe_{0.2}

To understand the intrinsic activity of the electrocatalysts in OER, the MA and SA were calculated as shown in Figure 6.5(e). MA was calculated with the mass loading of electrocatalysts, while specific activity was found with ECSA. Co_{1.4}Fe_{0.6} demonstrated higher MA and SA as compared to the other electrocatalysts. Co_{1.4}Fe_{0.6} have MA and SA of 33.53 A g⁻¹ and 0.318 mA cm⁻², respectively. Hence, the MA and SA of the Co_{1.4}Fe_{0.6} are higher than the benchmark electrocatalyst RuO₂ (MA= 8.87 A g⁻¹ and SA= 0.06224 mA cm⁻²) [160]. This result shows the exceptional intrinsic activity of Co_{1.4}Fe_{0.6} in OER. Figure 6.5(f) shows the Mott-Schottky plots for NBCF electrocatalysts. All the electrocatalysts display p-type behavior, because of the negative slope after 1.2 V vs RHE, which is the OER working range at 1.23 V vs RHE. In the potential range between 1.2 V and 1.7 V, there is no transition from n-type to p-type semiconductor behavior. The flat-band potential (E_{fb}) values for NBCF double perovskite oxide electrocatalysts were determined with linear extrapolation of the p-type behavior region. A more positively shifted flat-band potential indicates greater limitation on OER activity [167,168]. Among the NBCF double perovskite oxide electrocatalysts, Co_{1.4}Fe_{0.6} exhibits the lowest E_{fb} at 1.53 V vs RHE, comparable with its overpotential value of 384 mV. In contrast, Co_{1.6}Fe_{0.4}, Co_{1.8}Fe_{0.2}, and CoFe show increasing E_{fb} values, respectively. As a result, Co_{1.4}Fe_{0.6} demonstrates superior OER electrocatalytic activity with the lowest flat-band potential. Hence Co_{1.4}Fe_{0.6} is a promising candidate as an OER electrocatalyst due to its lower overpotential and enhanced intrinsic activity combined with lower flat-band potential. On the other hand, the Co_{1.8}Fe_{0.2} electrocatalyst demonstrates a higher charge transfer rate, along with an overpotential and ECSA similar to conventional previously reported OER electrocatalysts.

The analysis of ORR activity for NBCF electrocatalysts is illustrated in Figure 6.7. LSV curves are shown in Figure 6.7(a). The potentials at a current density of -1 mA cm^{-2} for CoFe, Co_{1.4}Fe_{0.6}, Co_{1.6}Fe_{0.4}, and Co_{1.8}Fe_{0.2} were recorded as 0.52, 0.64, 0.65, and 0.73 V, respectively. This indicates that Co_{1.8}Fe_{0.2} exhibits superior ORR activity compared to the other NBCF electrocatalysts. Additionally, the Tafel slopes derived from the Tafel plots were found to be -179 , -234 , -328 , and -281 mV dec^{-1} for CoFe, Co_{1.4}Fe_{0.6}, Co_{1.6}Fe_{0.4}, and Co_{1.8}Fe_{0.2}, respectively (Figure 6.7(b)). It is concluded that the reaction kinetics of the Co_{1.8}Fe_{0.2} electrocatalyst for ORR is comparable to the other NBCF electrocatalysts.

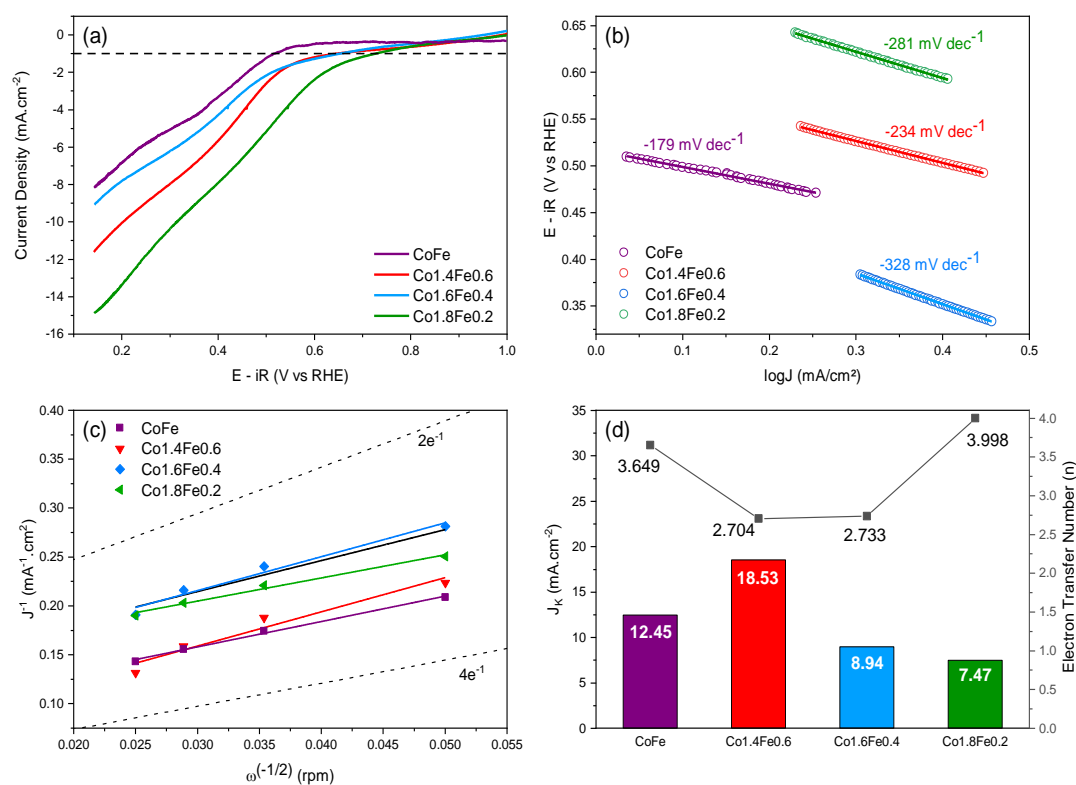


Figure 6.7 For NBCF electrocatalysts (a) ORR activity curves (b) Tafel plots (c) Koutecky-Levich plots at 0.15 V (d) Kinetic current density (J_k) and electron transfer number (n).

The electron transfer number and kinetic current densities of the NBCF electrocatalysts were calculated with the KL equation. As shown in Figure 6.8, KL plots were generated by LSV within a voltage range of 1.2 V to 0.14 V versus RHE at different rotation speeds. As the rotational speed of the working electrode increases, the reduction current increases too which indicates enhanced mass transport at the electrode surface due to improved oxygen diffusion from the electrolyte. Co_{1.8}Fe_{0.2} showed a higher reduction current density at a constant potential and rotational speed as compared to other NBCF electrocatalysts. The linearity observed in the KL plots illustrated in Figure 6.9 suggests that the ORR follows first-order kinetics. At a low voltage of 0.15 V versus RHE, the electron transfer number (*n*) was determined to be 3.649, 2.704, 2.733, and 3.998 for CoFe, Co_{1.4}Fe_{0.6}, Co_{1.6}Fe_{0.4}, and Co_{1.8}Fe_{0.2}, respectively (Figure 6.6(d)). The electron transfer number for Co_{1.8}Fe_{0.2} is closer to 4 so it can be concluded that the 4-electron ORR process dominates in Co_{1.8}Fe_{0.2} [161,162].

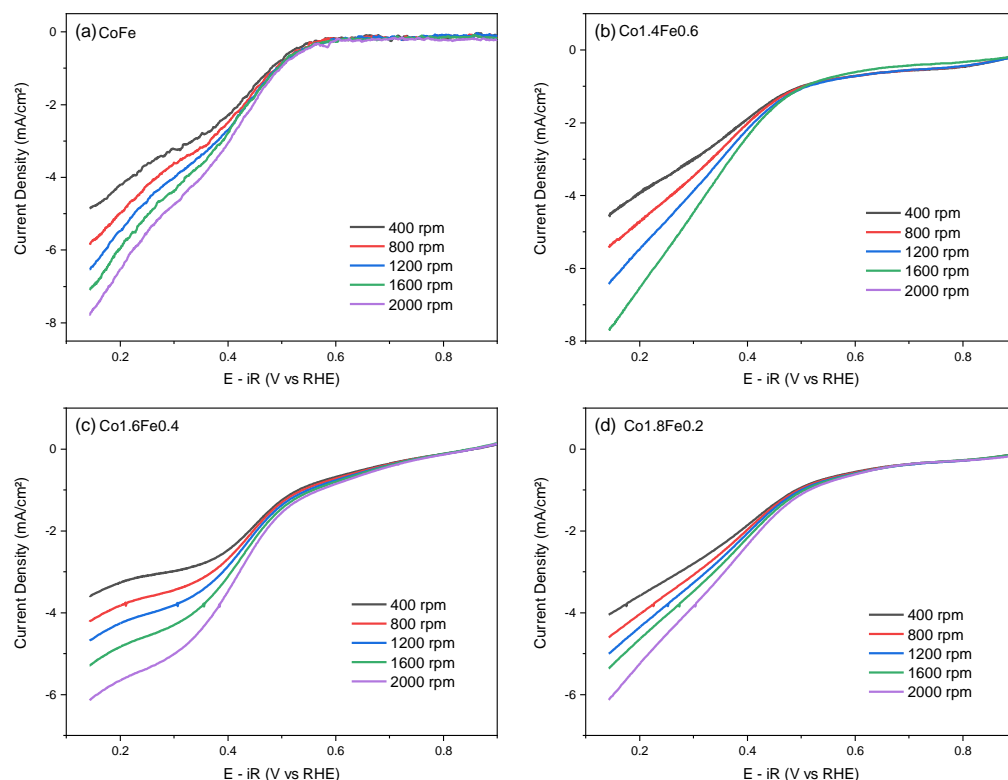


Figure 6.8 LSV curves at 400, 800, 1200, 1600, and 2000 rpm of (a) CoFe (b) Co_{1.4}Fe_{0.6} (c) Co_{1.6}Fe_{0.4} (d) Co_{1.8}Fe_{0.2}

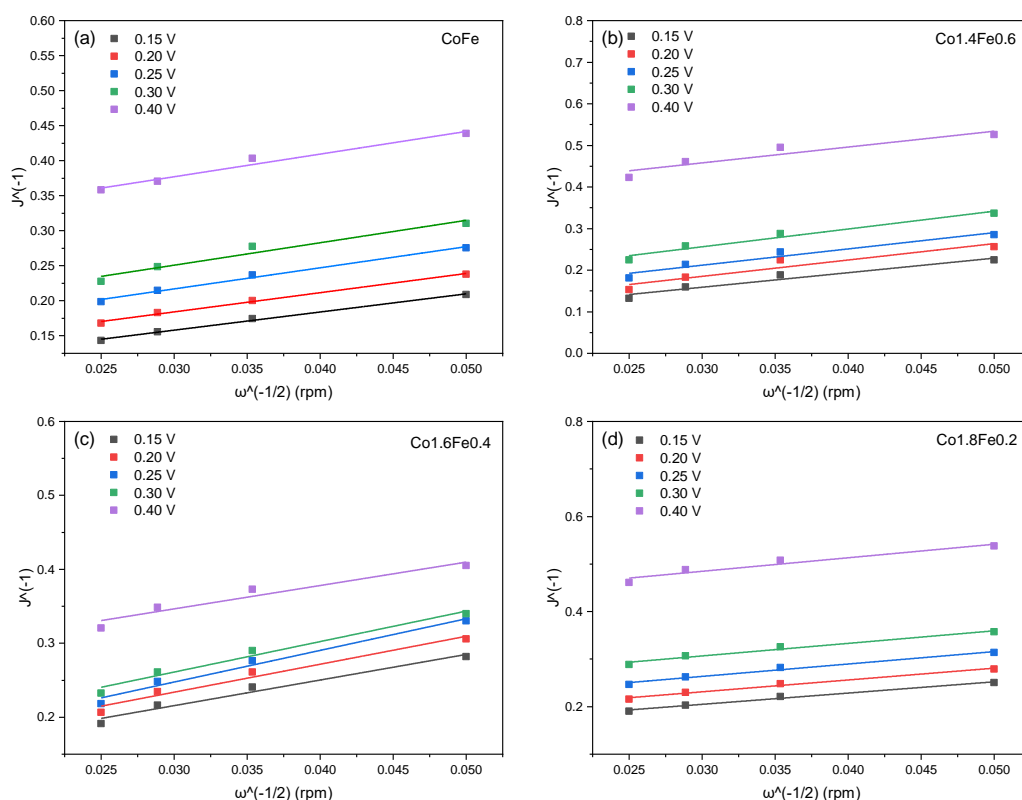


Figure 6.9 KL plots at 0.15, 0.20, 0.25, 0.30, 0.40 V of (a) CoFe (b) Co_{1.4}Fe_{0.6} (c) Co_{1.6}Fe_{0.4} (d) Co_{1.8}Fe_{0.2}

In conclusion, the potential gap between current densities of -1 mA cm^{-2} and 10 mA cm^{-2} was calculated to find the BI. The BI values for NBCF double perovskite oxides are 1.15, 0.97, 1.01, and 0.95 V for CoFe, Co_{1.4}Fe_{0.6}, Co_{1.6}Fe_{0.4}, and Co_{1.8}Fe_{0.2}, respectively. Therefore, among the NBCF double perovskite oxide electrocatalysts, Co_{1.8}Fe_{0.2} showcases superior bifunctional OER/ORR electrocatalytic activity with a low bifunctional index, enhanced charger transfer rate in OER, and 4-electron transfer in ORR.

6.4 Zn-Air Battery Performance of NBCF Electrocatalysts

Rechargeable Zn-Air batteries were constructed with a zinc plate as the anode, NBCF double perovskite oxides as the air cathodes, and a 6 M KOH electrolyte with an addition of 0.2 M Zn(OAc)₂.

Figure 6.10(a) illustrates polarization curves showing the charge and discharge characteristics of Zn-air batteries utilizing NBCF double perovskite oxides as air cathodes. The Zn-air battery with a Co_{1.8}Fe_{0.2} cathode requires 2.086 V for charge and 1.069 V for discharge to achieve a current density of 10 mA cm⁻². As shown in Figure 6.10(a) other NBCF-based Zn-air batteries have larger voltage gaps and CoFe demonstrates the most significant difference between discharging and charging. This difference features the promising compatibility of the Co_{1.8}Fe_{0.2} double perovskite oxide electrocatalyst in both OER and ORR. Additionally, the Co_{1.8}Fe_{0.2}-based Zn-air battery exhibits the highest and notable peak power density, reaching 64 mW cm⁻² at a higher current density of 135 mA cm⁻². On the contrary, the second-best peak power density is observed in the Co_{1.4}Fe_{0.6}-based Zn-air battery at 59 mW cm⁻² with a lower current density of 120 mA cm⁻². CoFe demonstrates the smallest peak power density, observed at the lowest current density of 100 mA cm⁻².

The discharge capacities of NBCF-based Zn-air batteries at 5 mA cm⁻², 10 mA cm⁻², and 50 mA cm⁻² current densities, respectively are illustrated in Figure 6.10(b), Figure 6.10(c), and Figure 6.10(d). The Zn-air batteries exhibit higher capacities at 5 mA cm⁻² compared to 10 mA cm⁻², and 50 mA cm⁻². Co_{1.8}Fe_{0.2} based Zn-air battery achieves a capacity of 443.34 mA h at 5 mA cm⁻², 428.27 mA h at 10 mA cm⁻², and 251.74 mA h at 50 mA cm⁻². This shows that in different current densities, Co_{1.8}Fe_{0.2} maintains a stable capacity since its capacity retention is affected less from an increase in current density as compared to other electrocatalysts. In contrast, the Co_{1.4}Fe_{0.6}-based Zn-air battery is more dependent on changes in current density, with the highest capacity of 477.28 mA h at 5 mA cm⁻², the second-lowest capacity of 324.59 mA h at 10 mA cm⁻², and the lowest capacity of 225.18 mA h at 50 mA cm⁻². This indicates that the capacity of the Co_{1.4}Fe_{0.6}-based Zn-air battery

may not be sustained at higher current densities, while Co_{1.8}Fe_{0.2} maintains a capacity that is not significantly lower even at higher current densities. Consequently, Co_{1.8}Fe_{0.2} demonstrates greater stability, making it a more dependable Zn-air battery electrocatalyst than Co_{1.4}Fe_{0.6}, despite its slightly lower capacity at lower current densities.

The cycling stability and rate capability of NBCF-based Zn-air batteries were evaluated systematically by changing the discharge rate from 0 to 20 mA cm⁻² and then returning to 0 mA cm⁻², while examining the output voltage as shown in Figure 6.10(e). Among NBCF-based Zn-air batteries, the Zn-air battery with Co_{1.8}Fe_{0.2} electrocatalyst exhibited superior rate capability and stability. At the beginning for the Co_{1.8}Fe_{0.2} electrocatalyst, the output voltage was 1.29 V, and after 400 minutes of operation, the output voltage decreased to 1.14 V, which was 87.14% of the initial output voltage. Remarkably, the Co_{1.8}Fe_{0.2} electrocatalyst exhibited the minimum voltage decay after 400 minutes of operation under different discharge current densities compared to other NBCF-based Zn-air batteries.

The cyclic charge-discharge performances of NBCF-based Zn-air batteries were evaluated at a constant current density of 5 mA cm⁻² at 5-minute charge and discharge intervals to comprehend the electrochemical durability of electrocatalysts (Figure 6.10(f)). Initially, the Co_{1.8}Fe_{0.2}-based Zn-air battery displayed charge and discharge voltages of 1.98 V and 1.18 V, respectively, with a voltage gap of only 800 mV. In contrast, other NBCF-based Zn-air batteries, such as Co_{1.6}Fe_{0.4}, Co_{1.4}Fe_{0.6}, Co_{1.2}Fe_{0.8}, and CoFe, had voltage gaps of 822 mV, 846 mV, 840 mV, and 897 mV, respectively as illustrated in Figure 6.10(g). The Co_{1.8}Fe_{0.2}-based Zn-air battery exhibited the smallest voltage gap. Over time, some of the NBCF-based Zn-air batteries experienced a loss of stability. The Co_{1.6}Fe_{0.4}-based Zn-air battery lasted approximately 110 hours, Co_{1.2}Fe_{0.8} lasted about 180 hours, and CoFe lasted about 200 hours before showing a significant increase in their voltage gap. In contrast, the Co_{1.8}Fe_{0.2} and Co_{1.4}Fe_{0.6} batteries endured for more than 350 hours with minimal increases in their voltage gap. Even after this extended period, the voltage gap of the Co_{1.8}Fe_{0.2} ZAB increased by only 41% from the initial voltage

gap after 350 hours, reaching 1.13 V. On the other hand, the voltage gap of the Co_{1.4}Fe_{0.6}-based ZAB increased to 1.37 V.

The performance comparison of NBCF-based Zn-air batteries reveals that while some configurations may outperform Co_{1.8}Fe_{0.2} electrocatalyst under specific conditions, overall, Co_{1.8}Fe_{0.2}-based Zn-air batteries demonstrate the most promising performance among the other NBCF-based rechargeable Zn-air batteries. For example, as compared to Co_{1.8}Fe_{0.2} which maintains its capacity across different discharge current densities Co_{1.4}Fe_{0.6} based Zn-air battery achieves the highest capacity at 5 mA cm⁻² but experiences a capacity decline at 10 mA cm⁻² discharge current density. While Co_{1.4}Fe_{0.6} shows a comparable cyclic charge-discharge time as Co_{1.8}Fe_{0.2}, it demonstrates lower voltage stability and significantly lower rate capability and peak power density as compared to Co_{1.8}Fe_{0.2}-based Zn-air battery. Although CoFe-based Zn-air battery exhibits a rate capability similar to Co_{1.8}Fe_{0.2}, the other experimental results show that it is the least effective cathode for rechargeable Zn-air batteries.

Experimental data indicates that the electrocatalyst with the highest cobalt content which is the Co_{1.8}Fe_{0.2} exhibits the highest peak power density (64 mW cm⁻²), the highest capacity at a 10 mA cm⁻² discharge current density (428.27 mA h), stable capacity retention, the highest rate capability (87.14%), and the longest cyclic charge-discharge time (350 hours), along with the lowest voltage gap after 350 hours. Even though the Co_{1.8}Fe_{0.2} electrocatalyst has moderate OER overpotential and Tafel slope, its distinct advantages lie in its low resistivity and high charge transfer rate compared to other NBCF electrocatalysts. Moreover, Co_{1.8}Fe_{0.2} exhibits better ORR performance as compared to other NBCF electrocatalysts with the lowest onset potential, highest limiting current, low kinetic current density, and efficient ~4-electron transfer processes. The calculated electron transfer number for Co_{1.8}Fe_{0.2}, close to 4, indicates highly efficient ORR performance, which significantly influences discharge-based experiments such as peak power density, capacity measurements, and rate capability tests.

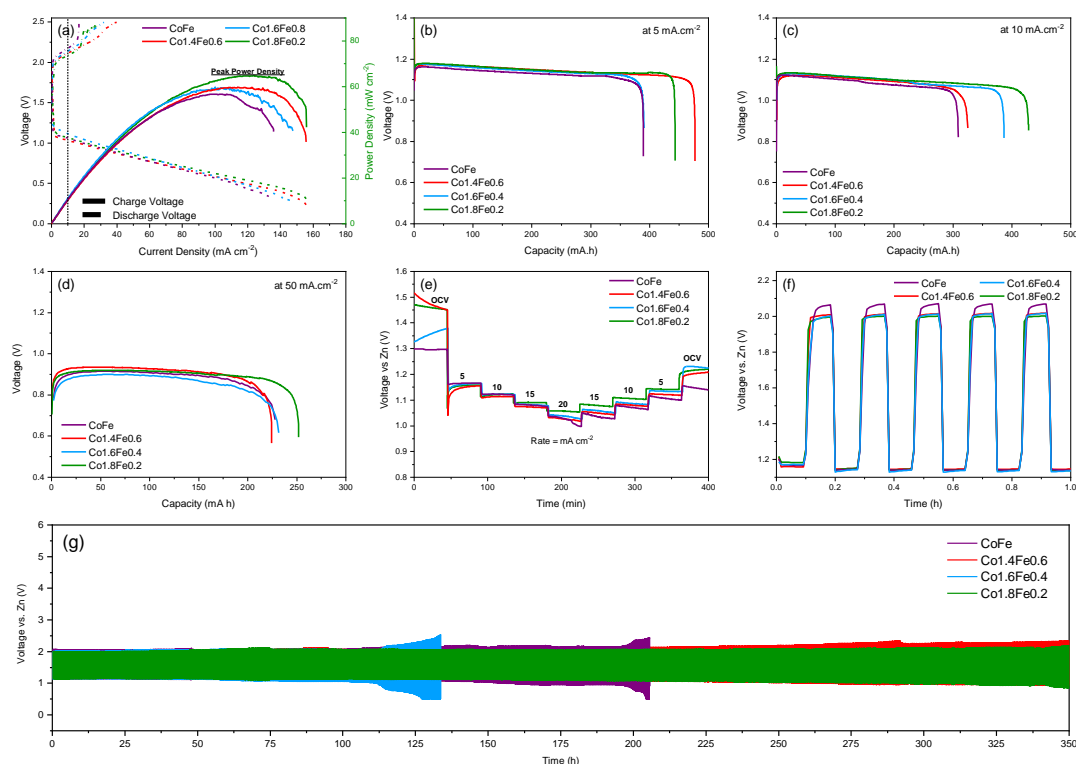


Figure 6.10 Zn-air batteries with NBCF-based air cathodes' (a) Peak power density plots along with charge and discharge polarization curves (b) Capacities at a current density of 5 mA cm^{-2} (c) Capacities at a current density of 10 mA cm^{-2} (d) Capacities at a current density of 50 mA cm^{-2} (e) Rate capability study (f) Durability performance during the first hour of cyclic charge-discharge (g) Cyclic charge-discharge performance at 5 mA cm^{-2}

6.5 Analysis of the Electronic Structure of Co_{1.8}Fe_{0.2} and CoFe

The work functions of Co_{1.8}Fe_{0.2} and CoFe electrocatalysts were determined with UPS by applying a bias voltage of -7 eV , and the UPS spectra are shown in Figure 6.11(a). The work functions (ϕ) were calculated by subtracting the He (I) radiation (21.22 eV) from the high-binding-energy cut-off. To ensure consistency, Fermi edge calibration was conducted with a sputter-cleaned Ag standard, aligning all energies to a common Fermi level (0 eV). Thus, the work function was computed using the equation: $\phi = h\nu - E_{\text{cut-off}}$, where $h\nu$ represents the incident photoelectron energy (21.22 eV), and $E_{\text{cut-off}}$ was determined through linear extrapolation with the baseline

of the secondary electron onset [169]. The work function of Co_{1.8}Fe_{0.2} was found to decrease to 3.06 eV from 3.6 eV for CoFe, indicating the higher intrinsic conductivity of the Co_{1.8}Fe_{0.2} electrocatalyst, consistent with the EIS results.

The positioning of the O p-band center relative to the Fermi energy (E_f) provided an alternative means of characterizing electrocatalytic performance. Consequently, the valence band (VB) spectra of CoFe and Co_{1.8}Fe_{0.2} are presented in Figure 6.11(b). The VB spectrum reveals O 2p electronic states hybridized with Co 3d and Fe 3d derived states, with Co 3d and Fe 3d states labeled as “A and B” in the 0-6 eV region, and O 2p character dominating in the 4-13 eV region farther from E_f marked as “C” in the XPS valence band spectra [170–172]. The XPS valence band spectra confirm that both Co_{1.8}Fe_{0.2} and CoFe exhibit the hybridization of O 2p and Co/Fe 3d orbitals, reducing the charge transfer gap between the electrocatalyst surface and oxygen intermediate species (O_2^* , OH^* , O^* , OOH^*) in the alkaline electrolyte solution. This facilitates the exchange of O_2^{2-}/OH^- on the surface for OH^- regeneration [132].

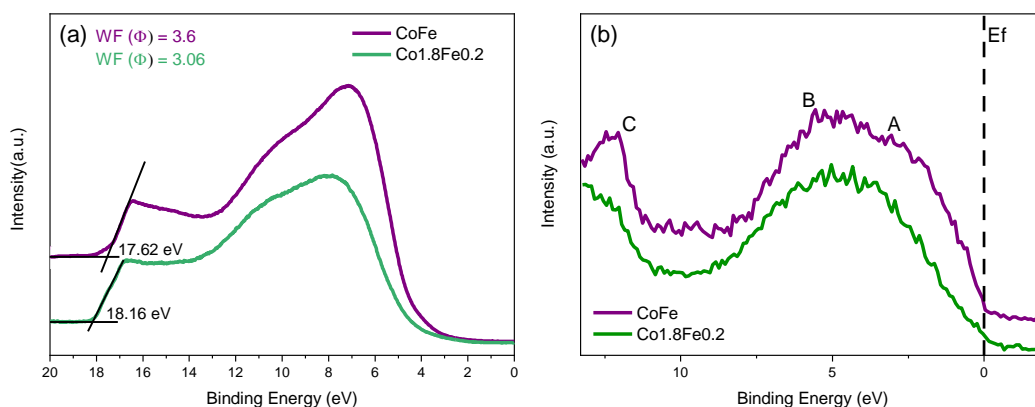


Figure 6.11 (a) UPS spectra and (b) XPS valence band spectra of CoFe, and Co_{1.8}Fe_{0.2}

6.6 Materials Characterization after Cyclic Charge/Discharge Battery Test

XRD analysis was performed on the $\text{Co}_{1.8}\text{Fe}_{0.2}$ air cathode after a 350-hour cyclic charge-discharge test to investigate whether there is a potential change in the crystal structure of the $\text{Co}_{1.8}\text{Fe}_{0.2}$ electrocatalyst or not. Figure 6.12 illustrates the XRD patterns of the $\text{Co}_{1.8}\text{Fe}_{0.2}$ double perovskite oxide before and after the cyclic charge-discharge experiment. XRD analysis of the $\text{Co}_{1.8}\text{Fe}_{0.2}$ air cathode after the cyclic charge-discharge test shows peaks that are consistent with a tetragonal structure with the space group "P4/mmm". In addition, in the XRD pattern, additional peaks corresponding to potassium oxide, potassium peroxide, and potassium hydroxide derivatives are observed, originating from the 6 M KOH electrolyte. Moreover, the presence of zinc oxide peaks in the XRD pattern can be attributed to both the reduction of the Zn anode during the operation of the Zn-air battery or the presence of $\text{Zn}(\text{OAc})_2$ additive in the electrolyte. Therefore, it is concluded that the crystal structure of $\text{Co}_{1.8}\text{Fe}_{0.2}$ remains unchanged even after 350 hours of cyclic charge-discharge testing.

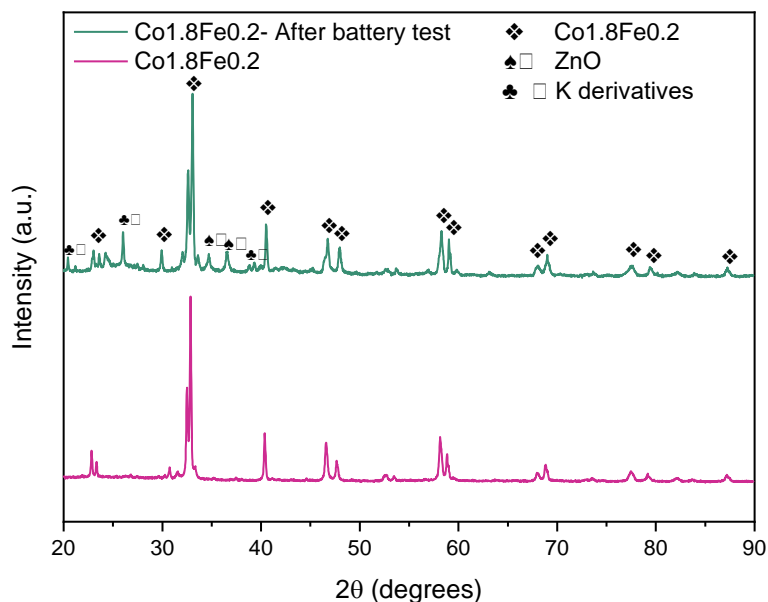


Figure 6.12 XRD patterns of $\text{Co}_{1.8}\text{Fe}_{0.2}$ before and after the cyclic charge-discharge experiment in the Zn-air battery.

CHAPTER 7

CONCLUSIONS

In this thesis, multicomponent oxides were designed as bifunctional oxygen electrocatalysts for use in rechargeable zinc-air battery air cathodes. The study examined the effects of oxygen vacancies and porosity in HEOs, as well as B-site doping in double perovskite oxides, on the electrocatalytic activity and performance of Zn-air batteries.

- In Chapter 4, we successfully synthesized single-phase, spinel crystal-structured $(\text{FeCrCoMnZn})_3\text{O}_{4-\delta}$ in both air and vacuum environments. By altering the calcination atmosphere from air to vacuum, we increased the oxygen vacancy content. HEO-Vac, with its higher oxygen vacancy content, outperforms HEO-Air in OER/ORR activity due to enhanced charge transfer rates and catalytic performance. Remarkably, HEO-Vac exhibits long-term stability and an overpotential of 329 mV at a current density of 10 mA cm^{-2} . The BI of HEO-Vac is 0.89 V, making it competitive with state-of-the-art electrocatalysts. When used in a Zn-air battery, HEO-Vac achieves a peak power density of 102 mW cm^{-2} , a specific capacity of $576.07 \text{ mA h g}^{-1}$, and a specific energy of $662.46 \text{ W h kg}^{-1}$ at a 5 mA cm^{-2} current density. Compared to the HEO-Air based Zn-air battery, the Zn-air battery with HEO-Vac shows improved performance with greater capacity, durability, and efficiency. This study introduces a novel method for modifying the structure of HEOs by manipulating the synthesis environment, offering significant potential for advancing HEOs in electrochemical energy storage applications.
- In Chapter 5, we synthesized nanoporous $(\text{FeCrCoMnZn})_3\text{O}_{4-\delta}$ powders by low-temperature sol-gel method using glycine. We changed the pore size in the HEO structure by applying calcination at $500 \text{ }^\circ\text{C}$, $600 \text{ }^\circ\text{C}$, and $700 \text{ }^\circ\text{C}$. The sample

calcined at 600 °C has a bigger pore size and higher oxygen vacancy content in its structure. As a result, the GLY600 nanoporous HEO sample exhibits the lowest overpotential with 447 mV at a current density of 10 mA cm⁻², faster reaction kinetics with 77.58 mV dec⁻¹ Tafel slope among the other nanoporous HEO electrocatalysts. When GLY600 is applied to a Zn-air battery, it achieves a capacity of 443.34 mA h at a current density of 5 mA cm⁻² and a peak power density of 80 mW cm⁻² at 133 mA cm⁻². The Zn-air battery with nano-porous GLY600 maintains its stability even after 1000 hours of cyclic charge-discharge. This study highlights the effect of porosity on Zn-air battery performance.

- In Chapter 6, we synthesized B-site doped NdBaCo_aFe_{2-a}O_{5+δ} (a= 1.0, 1.4, 1.6, 1.8) electrocatalysts, our results show that increasing the Co content leads to changes in both the crystal and electronic structures, enhancing electrocatalytic performance. The crystal structure shifts from orthorhombic in CoFe to tetragonal in Co_{1.8}Fe_{0.2}. Additionally, the oxidation state of Fe changes from +3 to +2, and the oxygen vacancy content increases with higher Co content. The rise in oxygen vacancies correlates with improved bifunctional electrocatalytic activity. Co_{1.8}Fe_{0.2} demonstrates the fastest charge transfer rate, optimal ORR performance with an approximate 4-electron transfer number, and a bifunctionality value of 0.95 V. In Zn-air batteries, the Co_{1.8}Fe_{0.2} air cathode exhibits remarkable performance, including a peak power density of 64 mW cm⁻², a high capacity of 428.27 mA h at a current density of 10 mA cm⁻², and prolonged cyclic stability exceeding 350 hours with minimal voltage gap increase. Comparative analysis with NBCF electrocatalysts shows the superior performance of the Co_{1.8}Fe_{0.2}-based Zn-air battery with an enhanced capacity, durability, and efficiency, attributed to its lower work function value of 3.06 eV. This study highlights the significant impact of B-site cation ratios on oxygen vacancy generation by modulating the Fe oxidation state while maintaining Co's oxidation state. Our findings emphasize the potential for synthesizing NBCF with controlled cation ratios and oxygen vacancies, leading to improved bifunctional electrocatalytic performance and zinc-air battery efficiency.

REFERENCES

- [1] C. Zhou, X. Chen, S. Liu, Y. Han, H. Meng, Q. Jiang, S. Zhao, F. Wei, J. Sun, T. Tan, R. Zhang, Superdurable Bifunctional Oxygen Electrocatalyst for High-Performance Zinc–Air Batteries, *J Am Chem Soc* 144 (2022) 2694–2704. <https://doi.org/10.1021/jacs.1c11675>.
- [2] Y. Li, M. Gong, Y. Liang, J. Feng, J.-E. Kim, H. Wang, G. Hong, B. Zhang, H. Dai, Advanced zinc-air batteries based on high-performance hybrid electrocatalysts, *Nat Commun* 4 (2013) 1805. <https://doi.org/10.1038/ncomms2812>.
- [3] Y.-P. Deng, Y. Jiang, R. Liang, S.-J. Zhang, D. Luo, Y. Hu, X. Wang, J.-T. Li, A. Yu, Z. Chen, Dynamic electrocatalyst with current-driven oxyhydroxide shell for rechargeable zinc-air battery, *Nat Commun* 11 (2020) 1952. <https://doi.org/10.1038/s41467-020-15853-1>.
- [4] M. Moloudi, A. Noori, M.S. Rahmanifar, Y. Shabangoli, M.F. El-Kady, N.B. Mohamed, R.B. Kaner, M.F. Mousavi, Layered Double Hydroxide Templated Synthesis of Amorphous NiCoFeB as a Multifunctional Electrocatalyst for Overall Water Splitting and Rechargeable Zinc–Air Batteries, *Adv Energy Mater* 13 (2023) 2203002. <https://doi.org/10.1002/aenm.202203002>.
- [5] T. Maiyalagan, K.A. Jarvis, S. Therese, P.J. Ferreira, A. Manthiram, Spinel-type lithium cobalt oxide as a bifunctional electrocatalyst for the oxygen evolution and oxygen reduction reactions, *Nat Commun* 5 (2014) 3949. <https://doi.org/10.1038/ncomms4949>.
- [6] C.C.L. McCrory, S. Jung, J.C. Peters, T.F. Jaramillo, Benchmarking Heterogeneous Electrocatalysts for the Oxygen Evolution Reaction, *J Am Chem Soc* 135 (2013) 16977–16987. <https://doi.org/10.1021/ja407115p>.
- [7] Y. Tong, J. Wu, P. Chen, H. Liu, W. Chu, C. Wu, Y. Xie, Vibronic Superexchange in Double Perovskite Electrocatalyst for Efficient

- Electrocatalytic Oxygen Evolution, *J Am Chem Soc* 140 (2018) 11165–11169. <https://doi.org/10.1021/jacs.8b06108>.
- [8] S. Cherevko, S. Geiger, O. Kasian, N. Kulyk, J.-P. Grote, A. Savan, B.R. Shrestha, S. Merzlikin, B. Breitbach, A. Ludwig, K.J.J. Mayrhofer, Oxygen and hydrogen evolution reactions on Ru, RuO₂, Ir, and IrO₂ thin film electrodes in acidic and alkaline electrolytes: A comparative study on activity and stability, *Catal Today* 262 (2016) 170–180. <https://doi.org/10.1016/j.cattod.2015.08.014>.
- [9] C. Wei, R.R. Rao, J. Peng, B. Huang, I.E.L. Stephens, M. Risch, Z.J. Xu, Y. Shao-Horn, Recommended Practices and Benchmark Activity for Hydrogen and Oxygen Electrocatalysis in Water Splitting and Fuel Cells, *Advanced Materials* 31 (2019) 1806296. <https://doi.org/10.1002/adma.201806296>.
- [10] S. Wang, A. Lu, C.-J. Zhong, Hydrogen production from water electrolysis: role of catalysts, *Nano Converge* 8 (2021) 4. <https://doi.org/10.1186/s40580-021-00254-x>.
- [11] X. Wu, C. Tang, Y. Cheng, X. Min, S.P. Jiang, S. Wang, Bifunctional Catalysts for Reversible Oxygen Evolution Reaction and Oxygen Reduction Reaction, *Chemistry – A European Journal* 26 (2020) 3906–3929. <https://doi.org/10.1002/chem.201905346>.
- [12] C. Ozgur, T. Erdil, U. Geyikci, C. Okuyucu, E. Lokcu, Y.E. Kalay, C. Toparli, Engineering Oxygen Vacancies in (FeCrCoMnZn)₃O_{4-δ} High Entropy Spinel Oxides Through Altering Fabrication Atmosphere for High-Performance Rechargeable Zinc-Air Batteries, *Global Challenges* 8 (2024). <https://doi.org/10.1002/gch2.202300199>.
- [13] T. Li, Y. Yao, B.H. Ko, Z. Huang, Q. Dong, J. Gao, W. Chen, J. Li, S. Li, X. Wang, R. Shahbazian-Yassar, F. Jiao, L. Hu, Carbon-Supported High-Entropy Oxide Nanoparticles as Stable Electrocatalysts for Oxygen

- Reduction Reactions, *Adv Funct Mater* 31 (2021) 2010561.
<https://doi.org/10.1002/adfm.202010561>.
- [14] D. Wang, Z. Liu, S. Du, Y. Zhang, H. Li, Z. Xiao, W. Chen, R. Chen, Y. Wang, Y. Zou, S. Wang, Low-temperature synthesis of small-sized high-entropy oxides for water oxidation, *J Mater Chem A Mater* 7 (2019) 24211–24216. <https://doi.org/10.1039/C9TA08740K>.
- [15] J.-W. Yeh, S.-K. Chen, S.-J. Lin, J.-Y. Gan, T.-S. Chin, T.-T. Shun, C.-H. Tsau, S.-Y. Chang, Nanostructured High-Entropy Alloys with Multiple Principal Elements: Novel Alloy Design Concepts and Outcomes, *Adv Eng Mater* 6 (2004) 299–303. <https://doi.org/10.1002/adem.200300567>.
- [16] D.O. Bayraktar, E. Lökçü, C. Ozgur, T. Erdil, C. Toparli, Effect of synthesis environment on the electrochemical properties of (FeMnCrCoZn) O_4 high-entropy oxides for Li-ion batteries, *Int J Energy Res* 46 (2022) 22124–22133.
<https://doi.org/10.1002/er.8749>.
- [17] E. Lökçü, Ç. Toparli, M. Anik, Electrochemical Performance of (MgCoNiZn) $_{1-x}$ Li $_x$ O High-Entropy Oxides in Lithium-Ion Batteries, *ACS Appl Mater Interfaces* 12 (2020) 23860–23866.
<https://doi.org/10.1021/acsami.0c03562>.
- [18] M. Jiang, J. Li, Y. Zhao, L. Pan, Q. Cao, D. Wang, Y. Du, Double Perovskites as Model Bifunctional Catalysts toward Rational Design: The Correlation between Electrocatalytic Activity and Complex Spin Configuration, *ACS Appl Mater Interfaces* 10 (2018) 19746–19754.
<https://doi.org/10.1021/acsami.8b05353>.
- [19] W.-Y. Huo, S.-Q. Wang, W.-H. Zhu, Z.-L. Zhang, F. Fang, Z.-H. Xie, J.-Q. Jiang, Recent progress on high-entropy materials for electrocatalytic water splitting applications, *Tungsten* 3 (2021) 161–180.
<https://doi.org/10.1007/s42864-021-00084-8>.

- [20] Y. Chen, H. Fu, Y. Huang, L. Huang, X. Zheng, Y. Dai, Y. Huang, W. Luo, Opportunities for High-Entropy Materials in Rechargeable Batteries, *ACS Mater Lett* 3 (2021) 160–170.
<https://doi.org/10.1021/acsmaterialslett.0c00484>.
- [21] A. Sarkar, Q. Wang, A. Schiele, M.R. Chellali, S.S. Bhattacharya, D. Wang, T. Brezesinski, H. Hahn, L. Velasco, B. Breitung, High-Entropy Oxides: Fundamental Aspects and Electrochemical Properties, *Advanced Materials* 31 (2019) 1806236. <https://doi.org/10.1002/adma.201806236>.
- [22] X. Yang, R. Guo, R. Cai, Y. Ouyang, P. Yang, J. Xiao, Engineering high-entropy materials for electrocatalytic water splitting, *Int J Hydrogen Energy* 47 (2022) 13561–13578. <https://doi.org/10.1016/j.ijhydene.2022.02.123>.
- [23] W.-J. Yin, B. Weng, J. Ge, Q. Sun, Z. Li, Y. Yan, Oxide perovskites, double perovskites and derivatives for electrocatalysis, photocatalysis, and photovoltaics, *Energy Environ Sci* 12 (2019) 442–462.
<https://doi.org/10.1039/C8EE01574K>.
- [24] T. Erdil, E. Lokcu, I. Yildiz, C. Okuyucu, Y.E. Kalay, C. Toparli, Facile Synthesis and Origin of Enhanced Electrochemical Oxygen Evolution Reaction Performance of 2H-Hexagonal $\text{Ba}_2\text{CoMnO}_{6-\delta}$ as a New Member in Double Perovskite Oxides, *ACS Omega* 7 (2022) 44147–44155.
<https://doi.org/10.1021/acsomega.2c05627>.
- [25] X. Cheng, E. Fabbri, M. Nachtegaal, I.E. Castelli, M. El Kazzi, R. Haumont, N. Marzari, T.J. Schmidt, Oxygen Evolution Reaction on $\text{La}_{1-x}\text{Sr}_x\text{CoO}_3$ Perovskites: A Combined Experimental and Theoretical Study of Their Structural, Electronic, and Electrochemical Properties, *Chemistry of Materials* 27 (2015) 7662–7672.
<https://doi.org/10.1021/acs.chemmater.5b03138>.
- [26] T. Erdil, C. Toparli, B-Site Effect on High-Entropy Perovskite Oxide as a Bifunctional Electrocatalyst for Rechargeable Zinc–Air Batteries, *ACS Appl*

- Energy Mater 6 (2023) 11255–11267.
<https://doi.org/10.1021/acsaem.3c02149>.
- [27] Y. Gu, A. Bao, X. Wang, Y. Chen, L. Dong, X. Liu, H. Pan, Y. Li, X. Qi, Engineering the oxygen vacancies of rocksalt-type high-entropy oxides for enhanced electrocatalysis, *Nanoscale* 14 (2022) 515–524.
<https://doi.org/10.1039/D1NR07000B>.
- [28] X. Liu, Y. Xing, K. Xu, H. Zhang, M. Gong, Q. Jia, S. Zhang, W. Lei, Kinetically Accelerated Lithium Storage in High-Entropy (LiMgCoNiCuZn)O Enabled By Oxygen Vacancies, *Small* 18 (2022) 2200524. <https://doi.org/10.1002/sml.202200524>.
- [29] S. Yu, Z. Shui, C. Wang, Y. Lei, Y. Liu, W. Zhao, X. Chen, The method of introducing oxygen vacancy into La_{0.8}Sr_{0.2}FeO₃-based catalyst: enhancing the ORR and OER performance, *J Mater Sci* 57 (2022) 12364–12376.
<https://doi.org/10.1007/s10853-022-07359-6>.
- [30] S. Zhang, N. Wei, Z. Yao, X. Zhao, M. Du, Q. Zhou, Oxygen vacancy-based ultrathin Co₃O₄ nanosheets as a high-efficiency electrocatalyst for oxygen evolution reaction, *Int J Hydrogen Energy* 46 (2021) 5286–5295.
<https://doi.org/10.1016/j.ijhydene.2020.11.072>.
- [31] P. Gayen, S. Saha, K. Bhattacharyya, V.K. Ramani, Oxidation State and Oxygen-Vacancy-Induced Work Function Controls Bifunctional Oxygen Electrocatalytic Activity, *ACS Catal* 10 (2020) 7734–7746.
<https://doi.org/10.1021/acscatal.0c01541>.
- [32] W. Du, J. Liu, A. Zeb, X. Lin, Regulating the Electronic Configuration of Spinel Zinc Manganate Derived from Metal–Organic Frameworks: Controlled Synthesis and Application in Anode Materials for Lithium-Ion Batteries, *ACS Appl Mater Interfaces* 14 (2022) 37652–37666.
<https://doi.org/10.1021/acsaami.2c06897>.

- [33] M.T. Greiner, L. Chai, M.G. Helander, W.-M. Tang, Z.-H. Lu, Transition Metal Oxide Work Functions: The Influence of Cation Oxidation State and Oxygen Vacancies, *Adv Funct Mater* 22 (2012) 4557–4568. <https://doi.org/10.1002/adfm.201200615>.
- [34] K. Zhu, F. Shi, X. Zhu, W. Yang, The roles of oxygen vacancies in electrocatalytic oxygen evolution reaction, *Nano Energy* 73 (2020) 104761. <https://doi.org/10.1016/j.nanoen.2020.104761>.
- [35] X. Zhang, X. Liu, Y. Zeng, Y. Tong, X. Lu, Oxygen Defects in Promoting the Electrochemical Performance of Metal Oxides for Supercapacitors: Recent Advances and Challenges, *Small Methods* 4 (2020). <https://doi.org/10.1002/smtd.201900823>.
- [36] M. Asnavandi, Y. Yin, Y. Li, C. Sun, C. Zhao, Promoting Oxygen Evolution Reactions through Introduction of Oxygen Vacancies to Benchmark NiFe–OOH Catalysts, *ACS Energy Lett* 3 (2018) 1515–1520. <https://doi.org/10.1021/acseenergylett.8b00696>.
- [37] G. Zhuang, Y. Chen, Z. Zhuang, Y. Yu, J. Yu, Oxygen vacancies in metal oxides: recent progress towards advanced catalyst design, *Sci China Mater* 63 (2020) 2089–2118. <https://doi.org/10.1007/s40843-020-1305-6>.
- [38] Z. Wang, R. Lin, Y. Huo, H. Li, L. Wang, Formation, Detection, and Function of Oxygen Vacancy in Metal Oxides for Solar Energy Conversion, *Adv Funct Mater* 32 (2022) 2109503. <https://doi.org/10.1002/adfm.202109503>.
- [39] C. Ozgur, T. Erdil, U. Geyikci, I. Yildiz, E. Lokcu, C. Toparli, B-site Doping Boosts the OER and ORR Performance of Double Perovskite Oxide as Air Cathode for Zinc-Air Batteries, *ChemPhysChem* (2024). <https://doi.org/10.1002/cphc.202400531>.

- [40] Q. Wang, S. Kaushik, X. Xiao, Q. Xu, Sustainable zinc–air battery chemistry: advances, challenges and prospects, *Chem Soc Rev* 52 (2023) 6139–6190. <https://doi.org/10.1039/D2CS00684G>.
- [41] T. Li, X. Peng, P. Cui, G. Shi, W. Yang, Z. Chen, Y. Huang, Y. Chen, J. Peng, R. Zou, X. Zeng, J. Yu, J. Gan, Z. Mu, Y. Chen, J. Zeng, J. Liu, Y. Yang, Y. Wei, J. Lu, Recent progress and future perspectives of flexible metal-air batteries, *SmartMat* 2 (2021) 519–553. <https://doi.org/10.1002/smm2.1076>.
- [42] X. Zhong, Y. Shao, B. Chen, C. Li, J. Sheng, X. Xiao, B. Xu, J. Li, H. Cheng, G. Zhou, Rechargeable Zinc–Air Batteries with an Ultralarge Discharge Capacity per Cycle and an Ultralong Cycle Life, *Advanced Materials* 35 (2023). <https://doi.org/10.1002/adma.202301952>.
- [43] X. Lv, Z. Wang, Z. Lai, Y. Liu, T. Ma, J. Geng, Z. Yuan, Rechargeable Zinc–Air Batteries: Advances, Challenges, and Prospects, *Small* 20 (2024). <https://doi.org/10.1002/sml.202306396>.
- [44] X. Chi, M. Li, J. Di, P. Bai, L. Song, X. Wang, F. Li, S. Liang, J. Xu, J. Yu, A highly stable and flexible zeolite electrolyte solid-state Li–air battery, *Nature* 592 (2021) 551–557. <https://doi.org/10.1038/s41586-021-03410-9>.
- [45] J. Lee, S. Tai Kim, R. Cao, N. Choi, M. Liu, K.T. Lee, J. Cho, Metal–Air Batteries with High Energy Density: Li–Air versus Zn–Air, *Adv Energy Mater* 1 (2011) 34–50. <https://doi.org/10.1002/aenm.201000010>.
- [46] J. Chang, G. Wang, Y. Yang, Recent Advances in Electrode Design for Rechargeable Zinc–Air Batteries, *Small Science* 1 (2021). <https://doi.org/10.1002/smsc.202100044>.
- [47] Md.A. Rahman, X. Wang, C. Wen, High Energy Density Metal-Air Batteries: A Review, *J Electrochem Soc* 160 (2013) A1759–A1771. <https://doi.org/10.1149/2.062310jes>.

- [48] J. Fu, R. Liang, G. Liu, A. Yu, Z. Bai, L. Yang, Z. Chen, Recent Progress in Electrically Rechargeable Zinc–Air Batteries, *Advanced Materials* 31 (2019). <https://doi.org/10.1002/adma.201805230>.
- [49] K.W. Leong, Y. Wang, M. Ni, W. Pan, S. Luo, D.Y.C. Leung, Rechargeable Zn-air batteries: Recent trends and future perspectives, *Renewable and Sustainable Energy Reviews* 154 (2022) 111771. <https://doi.org/10.1016/j.rser.2021.111771>.
- [50] B.J. Hopkins, C.N. Chervin, J.W. Long, D.R. Rolison, J.F. Parker, Projecting the Specific Energy of Rechargeable Zinc–Air Batteries, *ACS Energy Lett* 5 (2020) 3405–3408. <https://doi.org/10.1021/acsenerylett.0c01994>.
- [51] Y.-P. Deng, R. Liang, G. Jiang, Y. Jiang, A. Yu, Z. Chen, The Current State of Aqueous Zn-Based Rechargeable Batteries, *ACS Energy Lett* 5 (2020) 1665–1675. <https://doi.org/10.1021/acsenerylett.0c00502>.
- [52] C. Xia, Y. Zhou, C. He, A.I. Douka, W. Guo, K. Qi, B.Y. Xia, Recent Advances on Electrospun Nanomaterials for Zinc–Air Batteries, *Small Science* 1 (2021). <https://doi.org/10.1002/smsc.202100010>.
- [53] J. Fu, Z.P. Cano, M.G. Park, A. Yu, M. Fowler, Z. Chen, Electrically Rechargeable Zinc–Air Batteries: Progress, Challenges, and Perspectives, *Advanced Materials* 29 (2017). <https://doi.org/10.1002/adma.201604685>.
- [54] G.X. Zhang, Zinc as an Energy Carrier for Energy Conversion and Storage, *ECS Trans* 16 (2009) 47–59. <https://doi.org/10.1149/1.3110082>.
- [55] J. Jindra, J. Mrha, M. Musilov□, Zinc-air cell with neutral electrolyte, *J Appl Electrochem* 3 (1973) 297–301. <https://doi.org/10.1007/BF00613036>.
- [56] M.C. Cheiky, L.G. Danczyk, M.C. Wehrey, Rechargeable Zinc-Air Batteries in Electric Vehicle Applications, in: 1990. <https://doi.org/10.4271/901516>.

- [57] A.J. Appleby, J. Jacquelin, J.P. Pompon, Charge-Discharge Behavior of the C.G.E. Circulating Zinc-Air Vehicle Battery, in: 1977. <https://doi.org/10.4271/770381>.
- [58] S. Lee, J. Choi, M. Kim, J. Park, M. Park, J. Cho, Material design and surface chemistry for advanced rechargeable zinc–air batteries, *Chem Sci* 13 (2022) 6159–6180. <https://doi.org/10.1039/D1SC07212A>.
- [59] X.X. Wang, X. Yang, H. Liu, T. Han, J. Hu, H. Li, G. Wu, Air Electrodes for Flexible and Rechargeable Zn–Air Batteries, *Small Struct* 3 (2022). <https://doi.org/10.1002/sstr.202100103>.
- [60] J.-N. Liu, C.-X. Zhao, J. Wang, D. Ren, B.-Q. Li, Q. Zhang, A brief history of zinc–air batteries: 140 years of epic adventures, *Energy Environ Sci* 15 (2022) 4542–4553. <https://doi.org/10.1039/D2EE02440C>.
- [61] A.L. Zhu, D.P. Wilkinson, X. Zhang, Y. Xing, A.G. Rozhin, S.A. Kulinich, Zinc regeneration in rechargeable zinc-air fuel cells—A review, *J Energy Storage* 8 (2016) 35–50. <https://doi.org/10.1016/j.est.2016.09.007>.
- [62] Y. Ma, W. Chen, Z. Jiang, X. Tian, X. WangGuo, G. Chen, Z.-J. Jiang, NiFe nanoparticles supported on N-doped graphene hollow spheres entangled with self-grown N-doped carbon nanotubes for liquid electrolyte/flexible all-solid-state rechargeable zinc–air batteries, *J Mater Chem A Mater* 10 (2022) 12616–12631. <https://doi.org/10.1039/D2TA03110H>.
- [63] Z. Chen, W. Li, X. Yang, C. Ke, H. Chen, Q. Li, J. Guo, Y. He, Z. Guo, X. Liang, Gel polymer electrolyte with MXene to extend cycle lifespan of flexible and rechargeable Zinc–Air batteries, *J Power Sources* 523 (2022) 231020. <https://doi.org/10.1016/j.jpowsour.2022.231020>.
- [64] Z. Chen, W. Li, X. Yang, C. Ke, H. Chen, Q. Li, J. Guo, Y. He, Z. Guo, X. Liang, Gel polymer electrolyte with MXene to extend cycle lifespan of flexible and rechargeable Zinc–Air batteries, *J Power Sources* 523 (2022) 231020. <https://doi.org/10.1016/j.jpowsour.2022.231020>.

- [65] J. Fu, R. Liang, G. Liu, A. Yu, Z. Bai, L. Yang, Z. Chen, Recent Progress in Electrically Rechargeable Zinc–Air Batteries, *Advanced Materials* 31 (2019). <https://doi.org/10.1002/adma.201805230>.
- [66] Y. Li, H. Dai, Recent advances in zinc–air batteries, *Chem. Soc. Rev.* 43 (2014) 5257–5275. <https://doi.org/10.1039/C4CS00015C>.
- [67] S. Zhu, Z. Chen, B. Li, D. Higgins, H. Wang, H. Li, Z. Chen, Nitrogen-doped carbon nanotubes as air cathode catalysts in zinc-air battery, *Electrochim Acta* 56 (2011) 5080–5084. <https://doi.org/10.1016/j.electacta.2011.03.082>.
- [68] H.-I. Kim, E.-J. Kim, S.-J. Kim, H.-C. Shin, Influence of ZnO precipitation on the cycling stability of rechargeable Zn–air batteries, *J Appl Electrochem* 45 (2015) 335–342. <https://doi.org/10.1007/s10800-015-0793-4>.
- [69] J.F. Parker, C.N. Chervin, E.S. Nelson, D.R. Rolison, J.W. Long, Wiring zinc in three dimensions re-writes battery performance—dendrite-free cycling, *Energy Environ. Sci.* 7 (2014) 1117–1124. <https://doi.org/10.1039/C3EE43754J>.
- [70] Z. Zhao, X. Fan, J. Ding, W. Hu, C. Zhong, J. Lu, Challenges in Zinc Electrodes for Alkaline Zinc–Air Batteries: Obstacles to Commercialization, *ACS Energy Lett* 4 (2019) 2259–2270. <https://doi.org/10.1021/acseenergylett.9b01541>.
- [71] J.K. Nørskov, J. Rossmeisl, A. Logadottir, L. Lindqvist, J.R. Kitchin, T. Bligaard, H. Jónsson, Origin of the Overpotential for Oxygen Reduction at a Fuel-Cell Cathode, *J Phys Chem B* 108 (2004) 17886–17892. <https://doi.org/10.1021/jp047349j>.
- [72] Y. Jiao, Y. Zheng, M. Jaroniec, S.Z. Qiao, Origin of the Electrocatalytic Oxygen Reduction Activity of Graphene-Based Catalysts: A Roadmap to Achieve the Best Performance, *J Am Chem Soc* 136 (2014) 4394–4403. <https://doi.org/10.1021/ja500432h>.

- [73] P. Gu, M. Zheng, Q. Zhao, X. Xiao, H. Xue, H. Pang, Rechargeable zinc–air batteries: a promising way to green energy, *J Mater Chem A Mater* 5 (2017) 7651–7666. <https://doi.org/10.1039/C7TA01693J>.
- [74] L. Peng, L. Shang, T. Zhang, G.I.N. Waterhouse, Recent Advances in the Development of Single-Atom Catalysts for Oxygen Electrocatalysis and Zinc–Air Batteries, *Adv Energy Mater* 10 (2020). <https://doi.org/10.1002/aenm.202003018>.
- [75] D.B. Sepa, M.V. Vojnovic, A. Damjanovic, Reaction intermediates as a controlling factor in the kinetics and mechanism of oxygen reduction at platinum electrodes, *Electrochim Acta* 26 (1981) 781–793. [https://doi.org/10.1016/0013-4686\(81\)90037-2](https://doi.org/10.1016/0013-4686(81)90037-2).
- [76] C.F. Zinola, A.J. Arvia, G.L. Estiu, E.A. Castro, A Quantum Chemical Approach to the Influence of Platinum Surface Structure on the Oxygen Electroreduction Reaction, *J Phys Chem* 98 (1994) 7566–7576. <https://doi.org/10.1021/j100082a030>.
- [77] J.S. Spendelow, A. Wieckowski, Electrocatalysis of oxygen reduction and small alcohol oxidation in alkaline media, *Physical Chemistry Chemical Physics* 9 (2007) 2654. <https://doi.org/10.1039/b703315j>.
- [78] X. Ge, A. Sumboja, D. Wu, T. An, B. Li, F.W.T. Goh, T.S.A. Hor, Y. Zong, Z. Liu, Oxygen Reduction in Alkaline Media: From Mechanisms to Recent Advances of Catalysts, *ACS Catal* 5 (2015) 4643–4667. <https://doi.org/10.1021/acscatal.5b00524>.
- [79] P. Anand, M.-S. Wong, Y.-P. Fu, Perovskite oxide composites for bifunctional oxygen electrocatalytic activity and zinc-air battery application—a mini-review, *Energy Storage Mater* 58 (2023) 362–380. <https://doi.org/10.1016/j.ensm.2023.03.033>.
- [80] N.-T. Suen, S.-F. Hung, Q. Quan, N. Zhang, Y.-J. Xu, H.M. Chen, Electrocatalysis for the oxygen evolution reaction: recent development and

- future perspectives, *Chem Soc Rev* 46 (2017) 337–365.
<https://doi.org/10.1039/C6CS00328A>.
- [81] Y. Zhu, H.A. Tahini, Z. Hu, Y. Yin, Q. Lin, H. Sun, Y. Zhong, Y. Chen, F. Zhang, H. Lin, C. Chen, W. Zhou, X. Zhang, S.C. Smith, Z. Shao, H. Wang, Boosting oxygen evolution reaction by activation of lattice-oxygen sites in layered Ruddlesden-Popper oxide, *EcoMat* 2 (2020).
<https://doi.org/10.1002/eom2.12021>.
- [82] L. Peng, Z. Wei, Recent progress of mesoscience in design of electrocatalytic materials for hydrogen energy conversion, *Particuology* 48 (2020) 19–33. <https://doi.org/10.1016/j.partic.2018.08.013>.
- [83] X. Liu, X. Fan, B. Liu, J. Ding, Y. Deng, X. Han, C. Zhong, W. Hu, Mapping the Design of Electrolyte Materials for Electrically Rechargeable Zinc–Air Batteries, *Advanced Materials* 33 (2021).
<https://doi.org/10.1002/adma.202006461>.
- [84] L. Hu, P. Xiao, L. Xue, H. Li, T. Zhai, The rising zinc anodes for high-energy aqueous batteries, *EnergyChem* 3 (2021) 100052.
<https://doi.org/10.1016/j.enchem.2021.100052>.
- [85] J.F. Parker, E.S. Nelson, M.D. Wattendorf, C.N. Chervin, J.W. Long, D.R. Rolison, Retaining the 3D Framework of Zinc Sponge Anodes upon Deep Discharge in Zn–Air Cells, *ACS Appl Mater Interfaces* 6 (2014) 19471–19476. <https://doi.org/10.1021/am505266c>.
- [86] W. Gan, D. Zhou, L. Zhou, Z. Zhang, J. Zhao, Zinc electrode with anion conducting polyvinyl alcohol/poly(diallyldimethylammonium chloride) film coated ZnO for secondary zinc air batteries, *Electrochim Acta* 182 (2015) 430–436. <https://doi.org/10.1016/j.electacta.2015.09.105>.
- [87] S.-M. Lee, Y.-J. Kim, S.-W. Eom, N.-S. Choi, K.-W. Kim, S.-B. Cho, Improvement in self-discharge of Zn anode by applying surface modification

- for Zn–air batteries with high energy density, *J Power Sources* 227 (2013) 177–184. <https://doi.org/10.1016/j.jpowsour.2012.11.046>.
- [88] J.F. Parker, C.N. Chervin, E.S. Nelson, D.R. Rolison, J.W. Long, Wiring zinc in three dimensions re-writes battery performance—dendrite-free cycling, *Energy Environ. Sci.* 7 (2014) 1117–1124. <https://doi.org/10.1039/C3EE43754J>.
- [89] X.G. Zhang, Fibrous zinc anodes for high power batteries, *J Power Sources* 163 (2006) 591–597. <https://doi.org/10.1016/j.jpowsour.2006.09.034>.
- [90] C. Yang, Improvement of high-rate capability of alkaline Zn–MnO₂ battery, *J Power Sources* 112 (2002) 174–183. [https://doi.org/10.1016/S0378-7753\(02\)00354-3](https://doi.org/10.1016/S0378-7753(02)00354-3).
- [91] H. Kim, G. Jeong, Y.-U. Kim, J.-H. Kim, C.-M. Park, H.-J. Sohn, Metallic anodes for next generation secondary batteries, *Chem Soc Rev* 42 (2013) 9011. <https://doi.org/10.1039/c3cs60177c>.
- [92] D.P. Bhatt, R. Udhayan, Electrochemical studies on a zinc-lead-cadmium alloy in aqueous ammonium chloride solution, *J Power Sources* 47 (1994) 177–184. [https://doi.org/10.1016/0378-7753\(94\)80059-6](https://doi.org/10.1016/0378-7753(94)80059-6).
- [93] A.R. Suresh Kannan, S. Muralidharan, K.B. Sarangapani, V. Balaramachandran, V. Kapali, Corrosion and anodic behaviour of zinc and its ternary alloys in alkaline battery electrolytes, *J Power Sources* 57 (1995) 93–98. [https://doi.org/10.1016/0378-7753\(95\)02225-2](https://doi.org/10.1016/0378-7753(95)02225-2).
- [94] C.W. Lee, K. Sathiyarayanan, S.W. Eom, M.S. Yun, Novel alloys to improve the electrochemical behavior of zinc anodes for zinc/air battery, *J Power Sources* 160 (2006) 1436–1441. <https://doi.org/10.1016/j.jpowsour.2006.02.019>.

- [95] J. Vatsalarani, S. Geetha, D.C. Trivedi, P.C. Warriar, Stabilization of zinc electrodes with a conducting polymer, *J Power Sources* 158 (2006) 1484–1489. <https://doi.org/10.1016/j.jpowsour.2005.10.094>.
- [96] Y. Ein-Eli, M. Auinat, D. Starosvetsky, Electrochemical and surface studies of zinc in alkaline solutions containing organic corrosion inhibitors, *J Power Sources* 114 (2003) 330–337. [https://doi.org/10.1016/S0378-7753\(02\)00598-0](https://doi.org/10.1016/S0378-7753(02)00598-0).
- [97] S.-M. Lee, Y.-J. Kim, S.-W. Eom, N.-S. Choi, K.-W. Kim, S.-B. Cho, Improvement in self-discharge of Zn anode by applying surface modification for Zn–air batteries with high energy density, *J Power Sources* 227 (2013) 177–184. <https://doi.org/10.1016/j.jpowsour.2012.11.046>.
- [98] Y.-D. Cho, G.T.-K. Fey, Surface treatment of zinc anodes to improve discharge capacity and suppress hydrogen gas evolution, *J Power Sources* 184 (2008) 610–616. <https://doi.org/10.1016/j.jpowsour.2008.04.081>.
- [99] D.M. See, R.E. White, Temperature and Concentration Dependence of the Specific Conductivity of Concentrated Solutions of Potassium Hydroxide, *J Chem Eng Data* 42 (1997) 1266–1268. <https://doi.org/10.1021/je970140x>.
- [100] F.R. McLarnon, E.J. Cairns, The Secondary Alkaline Zinc Electrode, *J Electrochem Soc* 138 (1991) 645–656. <https://doi.org/10.1149/1.2085653>.
- [101] P. Chen, K. Zhang, D. Tang, W. Liu, F. Meng, Q. Huang, J. Liu, Recent Progress in Electrolytes for Zn–Air Batteries, *Front Chem* 8 (2020). <https://doi.org/10.3389/fchem.2020.00372>.
- [102] J.-F. Drillet, F. Holzer, T. Kallis, S. Müller, V.M. Schmidt, Influence of CO₂ on the stability of bifunctional oxygen electrodes for rechargeable zinc/air batteries and study of different CO₂ filter materials, *Physical Chemistry Chemical Physics* 3 (2001) 368–371. <https://doi.org/10.1039/b005523i>.

- [103] M.A. Al-Saleh, S. Gültekin, A.S. Al-Zakri, H. Celiker, Effect of carbon dioxide on the performance of Ni/PTFE and Ag/PTFE electrodes in an alkaline fuel cell, *J Appl Electrochem* 24 (1994) 575–580.
<https://doi.org/10.1007/BF00249861>.
- [104] H. Sadeghifar, N. Djilali, M. Bahrami, Effect of Polytetrafluoroethylene (PTFE) and micro porous layer (MPL) on thermal conductivity of fuel cell gas diffusion layers: Modeling and experiments, *J Power Sources* 248 (2014) 632–641. <https://doi.org/10.1016/j.jpowsour.2013.09.136>.
- [105] E. Davari, A.D. Johnson, A. Mittal, M. Xiong, D.G. Ivey, Manganese-cobalt mixed oxide film as a bifunctional catalyst for rechargeable zinc-air batteries, *Electrochim Acta* 211 (2016) 735–743.
<https://doi.org/10.1016/j.electacta.2016.06.085>.
- [106] W. YAN, C. HSUEH, C. SOONG, F. CHEN, C. CHENG, S. MEI, Effects of fabrication processes and material parameters of GDL on cell performance of PEM fuel cell, *Int J Hydrogen Energy* 32 (2007) 4452–4458.
<https://doi.org/10.1016/j.ijhydene.2007.02.003>.
- [107] O. Haas, J. Van Wesemael, SECONDARY BATTERIES – METAL-AIR SYSTEMS | Zinc–Air: Electrical Recharge, in: *Encyclopedia of Electrochemical Power Sources*, Elsevier, 2009: pp. 384–392.
<https://doi.org/10.1016/B978-044452745-5.00169-6>.
- [108] J. Park, H. Oh, T. Ha, Y. Il Lee, K. Min, A review of the gas diffusion layer in proton exchange membrane fuel cells: Durability and degradation, *Appl Energy* 155 (2015) 866–880.
<https://doi.org/10.1016/j.apenergy.2015.06.068>.
- [109] J. Zhang, Z. Zhao, Z. Xia, L. Dai, A metal-free bifunctional electrocatalyst for oxygen reduction and oxygen evolution reactions, *Nat Nanotechnol* 10 (2015) 444–452. <https://doi.org/10.1038/nnano.2015.48>.

- [110] T. Ling, D.-Y. Yan, Y. Jiao, H. Wang, Y. Zheng, X. Zheng, J. Mao, X.-W. Du, Z. Hu, M. Jaroniec, S.-Z. Qiao, Engineering surface atomic structure of single-crystal cobalt (II) oxide nanorods for superior electrocatalysis, *Nat Commun* 7 (2016) 12876. <https://doi.org/10.1038/ncomms12876>.
- [111] J.P. Collman, P. Denisevich, Y. Konai, M. Marrocco, C. Koval, F.C. Anson, Electrode catalysis of the four-electron reduction of oxygen to water by dicobalt face-to-face porphyrins, *J Am Chem Soc* 102 (1980) 6027–6036. <https://doi.org/10.1021/ja00539a009>.
- [112] H. Wang, C. Tang, B. Wang, B. Li, Q. Zhang, Bifunctional Transition Metal Hydroxysulfides: Room-Temperature Sulfurization and Their Applications in Zn–Air Batteries, *Advanced Materials* 29 (2017). <https://doi.org/10.1002/adma.201702327>.
- [113] G. Fu, Y. Tang, J. Lee, Recent Advances in Carbon-Based Bifunctional Oxygen Electrocatalysts for Zn–Air Batteries, *ChemElectroChem* 5 (2018) 1424–1434. <https://doi.org/10.1002/celc.201800373>.
- [114] L. Jörissen, Bifunctional oxygen/air electrodes, *J Power Sources* 155 (2006) 23–32. <https://doi.org/10.1016/j.jpowsour.2005.07.038>.
- [115] S. Guo, S. Zhang, S. Sun, Tuning Nanoparticle Catalysis for the Oxygen Reduction Reaction, *Angewandte Chemie International Edition* 52 (2013) 8526–8544. <https://doi.org/10.1002/anie.201207186>.
- [116] G. Wang, Z. Yang, Y. Du, Y. Yang, Programmable Exposure of Pt Active Facets for Efficient Oxygen Reduction, *Angewandte Chemie International Edition* 58 (2019) 15848–15854. <https://doi.org/10.1002/anie.201907322>.
- [117] L. Bu, N. Zhang, S. Guo, X. Zhang, J. Li, J. Yao, T. Wu, G. Lu, J.-Y. Ma, D. Su, X. Huang, Biaxially strained PtPb/Pt core/shell nanoplate boosts oxygen reduction catalysis, *Science* (1979) 354 (2016) 1410–1414. <https://doi.org/10.1126/science.aah6133>.

- [118] C.M. Rost, E. Sachet, T. Borman, A. Moballegh, E.C. Dickey, D. Hou, J.L. Jones, S. Curtarolo, J.-P. Maria, Entropy-stabilized oxides, *Nat Commun* 6 (2015) 8485. <https://doi.org/10.1038/ncomms9485>.
- [119] A. Sarkar, B. Breitung, H. Hahn, High entropy oxides: The role of entropy, enthalpy and synergy, *Scr Mater* 187 (2020) 43–48. <https://doi.org/10.1016/j.scriptamat.2020.05.019>.
- [120] X. Xu, Z. Shao, S.P. Jiang, High-Entropy Materials for Water Electrolysis, *Energy Technology* 10 (2022). <https://doi.org/10.1002/ente.202200573>.
- [121] Z. Wang, J. You, Y. Zhao, R. Yao, G. Liu, J. Lu, S. Zhao, Research progress on high entropy alloys and high entropy derivatives as OER catalysts, *J Environ Chem Eng* 11 (2023) 109080. <https://doi.org/10.1016/j.jece.2022.109080>.
- [122] Y. Sun, S. Dai, High-entropy materials for catalysis: A new frontier, *Sci Adv* 7 (2021). <https://doi.org/10.1126/sciadv.abg1600>.
- [123] B. Talluri, K. Yoo, J. Kim, High entropy spinel metal oxide (CoCrFeMnNi)₃O₄ nanoparticles as novel efficient electrocatalyst for methanol oxidation and oxygen evolution reactions, *J Environ Chem Eng* 10 (2022) 106932. <https://doi.org/10.1016/j.jece.2021.106932>.
- [124] K. Iwase, I. Honma, High-Entropy Spinel Oxide Nanoparticles Synthesized via Supercritical Hydrothermal Processing as Oxygen Evolution Electrocatalysts, *ACS Appl Energy Mater* (2022). <https://doi.org/10.1021/acsaem.2c01751>.
- [125] Z. Ding, J. Bian, S. Shuang, X. Liu, Y. Hu, C. Sun, Y. Yang, High Entropy Intermetallic–Oxide Core–Shell Nanostructure as Superb Oxygen Evolution Reaction Catalyst, *Adv Sustain Syst* 4 (2020) 1900105. <https://doi.org/10.1002/adsu.201900105>.

- [126] Y. Zhang, W. Dai, P. Zhang, T. Lu, Y. Pan, In-situ electrochemical tuning of (CoNiMnZnFe)₃O_{3.2} high-entropy oxide for efficient oxygen evolution reactions, *J Alloys Compd* 868 (2021) 159064. <https://doi.org/10.1016/j.jallcom.2021.159064>.
- [127] C. Duan, X. Li, D. Wang, Z. Wang, H. Sun, R. Zheng, Y. Liu, Nanosized high entropy spinel oxide (FeCoNiCrMn)₃O₄ as a highly active and ultra-stable electrocatalyst for the oxygen evolution reaction, *Sustain Energy Fuels* 6 (2022) 1479–1488. <https://doi.org/10.1039/D1SE02038B>.
- [128] J. Hwang, R.R. Rao, L. Giordano, Y. Katayama, Y. Yu, Y. Shao-Horn, Perovskites in catalysis and electrocatalysis, *Science* (1979) 358 (2017) 751–756. <https://doi.org/10.1126/science.aam7092>.
- [129] D. Liu, P. Zhou, H. Bai, H. Ai, X. Du, M. Chen, D. Liu, W.F. Ip, K.H. Lo, C.T. Kwok, S. Chen, S. Wang, G. Xing, X. Wang, H. Pan, Development of Perovskite Oxide-Based Electrocatalysts for Oxygen Evolution Reaction, *Small* 17 (2021) 2101605. <https://doi.org/10.1002/sml.202101605>.
- [130] A.T. Mulder, N.A. Benedek, J.M. Rondinelli, C.J. Fennie, Turning ABO₃ Antiferroelectrics into Ferroelectrics: Design Rules for Practical Rotation-Driven Ferroelectricity in Double Perovskites and A₃B₂O₇ Ruddlesden-Popper Compounds, *Adv Funct Mater* (2013) n/a-n/a. <https://doi.org/10.1002/adfm.201300210>.
- [131] J. Song, C. Wei, Z.-F. Huang, C. Liu, L. Zeng, X. Wang, Z.J. Xu, A review on fundamentals for designing oxygen evolution electrocatalysts, *Chem Soc Rev* 49 (2020) 2196–2214. <https://doi.org/10.1039/C9CS00607A>.
- [132] P. Anand, M.-S. Wong, Y.-P. Fu, Lanthanum strontium cobaltite-based perovskite as an electrocatalyst for zinc-air battery application, *J Energy Storage* 77 (2024) 109917. <https://doi.org/10.1016/j.est.2023.109917>.

- [133] X. Wang, H. Zhong, S. Xi, W.S.V. Lee, J. Xue, Understanding of Oxygen Redox in the Oxygen Evolution Reaction, *Advanced Materials* 34 (2022). <https://doi.org/10.1002/adma.202107956>.
- [134] Y. Zhu, L. Zhang, B. Zhao, H. Chen, X. Liu, R. Zhao, X. Wang, J. Liu, Y. Chen, M. Liu, Improving the Activity for Oxygen Evolution Reaction by Tailoring Oxygen Defects in Double Perovskite Oxides, *Adv Funct Mater* 29 (2019). <https://doi.org/10.1002/adfm.201901783>.
- [135] J.-W. Zhao, Z.-X. Shi, C.-F. Li, Q. Ren, G.-R. Li, Regulation of Perovskite Surface Stability on the Electrocatalysis of Oxygen Evolution Reaction, *ACS Mater Lett* 3 (2021) 721–737. <https://doi.org/10.1021/acsmaterialslett.1c00018>.
- [136] X. Cao, X. Yan, L. Ke, K. Zhao, N. Yan, Proton-Assisted Reconstruction of Perovskite Oxides: Toward Improved Electrocatalytic Activity, *ACS Appl Mater Interfaces* 13 (2021) 22009–22016. <https://doi.org/10.1021/acсами.1c03276>.
- [137] B. Zhao, L. Zhang, D. Zhen, S. Yoo, Y. Ding, D. Chen, Y. Chen, Q. Zhang, B. Doyle, X. Xiong, M. Liu, A tailored double perovskite nanofiber catalyst enables ultrafast oxygen evolution, *Nat Commun* 8 (2017) 14586. <https://doi.org/10.1038/ncomms14586>.
- [138] X. Xu, Y. Zhong, Z. Shao, Double Perovskites in Catalysis, Electrocatalysis, and Photo(electro)catalysis, *Trends Chem* 1 (2019) 410–424. <https://doi.org/10.1016/j.trechm.2019.05.006>.
- [139] S. She, J. Yu, W. Tang, Y. Zhu, Y. Chen, J. Sunarso, W. Zhou, Z. Shao, Systematic Study of Oxygen Evolution Activity and Stability on $\text{La}_{1-x}\text{Sr}_x\text{FeO}_{3-\delta}$ Perovskite Electrocatalysts in Alkaline Media, *ACS Appl Mater Interfaces* 10 (2018) 11715–11721. <https://doi.org/10.1021/acсами.8b00682>.
- [140] X. Xu, C. Su, W. Zhou, Y. Zhu, Y. Chen, Z. Shao, Co-doping Strategy for Developing Perovskite Oxides as Highly Efficient Electrocatalysts for

- Oxygen Evolution Reaction, *Advanced Science* 3 (2016).
<https://doi.org/10.1002/advs.201500187>.
- [141] H. Sun, X. Xu, Y. Song, W. Zhou, Z. Shao, Designing High-Valence Metal Sites for Electrochemical Water Splitting, *Adv Funct Mater* 31 (2021) 2009779. <https://doi.org/10.1002/adfm.202009779>.
- [142] J.T. Mefford, X. Rong, A.M. Abakumov, W.G. Hardin, S. Dai, A.M. Kolpak, K.P. Johnston, K.J. Stevenson, Water electrolysis on $\text{La}_{1-x}\text{Sr}_x\text{CoO}_{3-\delta}$ perovskite electrocatalysts, *Nat Commun* 7 (2016) 11053. <https://doi.org/10.1038/ncomms11053>.
- [143] Y. Lv, Z. Li, Y. Yu, J. Yin, K. Song, B. Yang, L. Yuan, X. Hu, Copper/cobalt-doped LaMnO_3 perovskite oxide as a bifunctional catalyst for rechargeable Li-O₂ batteries, *J Alloys Compd* 801 (2019) 19–26. <https://doi.org/10.1016/j.jallcom.2019.06.114>.
- [144] N.-I. Kim, S.-H. Cho, S.H. Park, Y.J. Lee, R.A. Afzal, J. Yoo, Y.-S. Seo, Y.J. Lee, J.-Y. Park, B-site doping effects of $\text{NdBa}_{0.75}\text{Ca}_{0.25}\text{Co}_2\text{O}_{5+\delta}$ double perovskite catalysts for oxygen evolution and reduction reactions, *J Mater Chem A Mater* 6 (2018) 17807–17818. <https://doi.org/10.1039/C8TA06236F>.
- [145] Z. Gao, L. V. Mogni, E.C. Miller, J.G. Railsback, S.A. Barnett, A perspective on low-temperature solid oxide fuel cells, *Energy Environ Sci* 9 (2016) 1602–1644. <https://doi.org/10.1039/C5EE03858H>.
- [146] R. Merkle, Y.A. Mastrikov, E.A. Kotomin, M.M. Kuklja, J. Maier, First Principles Calculations of Oxygen Vacancy Formation and Migration in $\text{Ba}_{1-x}\text{Sr}_x\text{Co}_{1-y}\text{Fe}_y\text{O}_{3-\delta}$ Perovskites, *J Electrochem Soc* 159 (2011) B219–B226. <https://doi.org/10.1149/2.077202jes>.
- [147] S. Anantharaj, S. Noda, Appropriate Use of Electrochemical Impedance Spectroscopy in Water Splitting Electrocatalysis, *ChemElectroChem* 7 (2020) 2297–2308. <https://doi.org/10.1002/celec.202000515>.

- [148] C. Wei, S. Sun, D. Mandler, X. Wang, S.Z. Qiao, Z.J. Xu, Approaches for measuring the surface areas of metal oxide electrocatalysts for determining their intrinsic electrocatalytic activity, *Chem Soc Rev* 48 (2019) 2518–2534. <https://doi.org/10.1039/C8CS00848E>.
- [149] J. Dai, Y. Zhu, Y. Zhong, J. Miao, B. Lin, W. Zhou, Z. Shao, Enabling High and Stable Electrocatalytic Activity of Iron-Based Perovskite Oxides for Water Splitting by Combined Bulk Doping and Morphology Designing, *Adv Mater Interfaces* 6 (2019) 1801317. <https://doi.org/10.1002/admi.201801317>.
- [150] S. Anantharaj, S.R. Ede, K. Karthick, S. Sam Sankar, K. Sangeetha, P.E. Karthik, S. Kundu, Precision and correctness in the evaluation of electrocatalytic water splitting: revisiting activity parameters with a critical assessment, *Energy Environ Sci* 11 (2018) 744–771. <https://doi.org/10.1039/C7EE03457A>.
- [151] X. Ye, S. Song, L. Li, Y.-C. Chang, S. Qin, Z. Liu, Y.-C. Huang, J. Zhou, L. Zhang, C.-L. Dong, C.-W. Pao, H.-J. Lin, C.-T. Chen, Z. Hu, J.-Q. Wang, Y. Long, *A*–*B* Intersite Cooperation-Enhanced Water Splitting in Quadruple Perovskite Oxide $\text{CaCu}_3\text{Ir}_4\text{O}_{12}$, *Chemistry of Materials* 33 (2021) 9295–9305. <https://doi.org/10.1021/acs.chemmater.1c03015>.
- [152] A. Safakas, G. Bampos, S. Bebelis, Oxygen reduction reaction on $\text{La}_{0.8}\text{Sr}_{0.2}\text{Co}_x\text{Fe}_{1-x}\text{O}_{3-\delta}$ perovskite/carbon black electrocatalysts in alkaline medium, *Appl Catal B* 244 (2019) 225–232. <https://doi.org/10.1016/j.apcatb.2018.11.015>.
- [153] N. Khellaf, A. Kahoul, F. Naamoune, N. Alonso-Vante, Electrochemistry of Nanocrystalline $\text{La}_{0.5}\text{Sr}_{0.5}\text{MnO}_3$ Perovskite for the Oxygen Reduction Reaction in Alkaline Medium, *Electrocatalysis* 8 (2017) 450–458. <https://doi.org/10.1007/s12678-017-0397-3>.

- [154] N. Sreenivasulu, U.N. Kumar, K.M.V. V. Madhav, T. Thomas, S.S. Bhattacharya, Structural and Electrochemical Investigations on Nanocrystalline High Entropy Spinel Oxides for Battery-Like Supercapacitor Applications, *ChemistrySelect* 7 (2022).
<https://doi.org/10.1002/slct.202104015>.
- [155] D. Carta, M.F. Casula, A. Falqui, D. Loche, G. Mountjoy, C. Sangregorio, A. Corrias, A Structural and Magnetic Investigation of the Inversion Degree in Ferrite Nanocrystals MFe_2O_4 ($M = Mn, Co, Ni$), *The Journal of Physical Chemistry C* 113 (2009) 8606–8615. <https://doi.org/10.1021/jp901077c>.
- [156] H. Xu, Z. Zhang, J. Liu, C.-L. Do-Thanh, H. Chen, S. Xu, Q. Lin, Y. Jiao, J. Wang, Y. Wang, Y. Chen, S. Dai, Entropy-stabilized single-atom Pd catalysts via high-entropy fluorite oxide supports, *Nat Commun* 11 (2020) 3908. <https://doi.org/10.1038/s41467-020-17738-9>.
- [157] T.X. Nguyen, Y. Liao, C. Lin, Y. Su, J. Ting, Advanced High Entropy Perovskite Oxide Electrocatalyst for Oxygen Evolution Reaction, *Adv Funct Mater* 31 (2021) 2101632. <https://doi.org/10.1002/adfm.202101632>.
- [158] W. Xu, F. Lyu, Y. Bai, A. Gao, J. Feng, Z. Cai, Y. Yin, Porous cobalt oxide nanoplates enriched with oxygen vacancies for oxygen evolution reaction, *Nano Energy* 43 (2018) 110–116.
<https://doi.org/10.1016/j.nanoen.2017.11.022>.
- [159] Y.-Q. Zhang, H.-B. Tao, Z. Chen, M. Li, Y.-F. Sun, B. Hua, J.-L. Luo, *In situ* grown cobalt phosphide (CoP) on perovskite nanofibers as an optimized trifunctional electrocatalyst for Zn–air batteries and overall water splitting, *J Mater Chem A Mater* 7 (2019) 26607–26617.
<https://doi.org/10.1039/C9TA08936E>.
- [160] Y. Lee, J. Suntivich, K.J. May, E.E. Perry, Y. Shao-Horn, Synthesis and Activities of Rutile IrO_2 and RuO_2 Nanoparticles for Oxygen Evolution in

Acid and Alkaline Solutions, *J Phys Chem Lett* 3 (2012) 399–404.
<https://doi.org/10.1021/jz2016507>.

- [161] Y. Zhu, W. Zhou, J. Yu, Y. Chen, M. Liu, Z. Shao, Enhancing Electrocatalytic Activity of Perovskite Oxides by Tuning Cation Deficiency for Oxygen Reduction and Evolution Reactions, *Chemistry of Materials* 28 (2016) 1691–1697. <https://doi.org/10.1021/acs.chemmater.5b04457>.
- [162] C. Alegre, E. Modica, A.S. Aricò, V. Baglio, Bifunctional oxygen electrode based on a perovskite/carbon composite for electrochemical devices, *Journal of Electroanalytical Chemistry* 808 (2018) 412–419.
<https://doi.org/10.1016/j.jelechem.2017.06.023>.
- [163] C.N. Chervin, J.W. Long, J.F. Parker, D.R. Rolison, *Rechargeable Zn-Air Batteries with Pulse-Power Capability*, 2020.
- [164] T. Yamashita, P. Hayes, Analysis of XPS spectra of Fe²⁺ and Fe³⁺ ions in oxide materials, *Appl Surf Sci* 254 (2008) 2441–2449.
<https://doi.org/10.1016/j.apsusc.2007.09.063>.
- [165] M. Retuerto, F. Calle-Vallejo, L. Pascual, G. Lumbeeck, M.T. Fernandez-Diaz, M. Croft, J. Gopalakrishnan, M.A. Peña, J. Hadermann, M. Greenblatt, S. Rojas, La_{1.5} Sr_{0.5} NiMn_{0.5} Ru_{0.5} O₆ Double Perovskite with Enhanced ORR/OER Bifunctional Catalytic Activity, *ACS Appl Mater Interfaces* 11 (2019) 21454–21464. <https://doi.org/10.1021/acsami.9b02077>.
- [166] R.A. Rincón, J. Masa, S. Mehrpour, F. Tietz, W. Schuhmann, Activation of oxygen evolving perovskites for oxygen reduction by functionalization with Fe–N_x/C groups, *Chem. Commun.* 50 (2014) 14760–14762.
<https://doi.org/10.1039/C4CC06446A>.
- [167] D. Antipin, M. Risch, Trends of epitaxial perovskite oxide films catalyzing the oxygen evolution reaction in alkaline media, *Journal of Physics: Energy* 2 (2020) 032003. <https://doi.org/10.1088/2515-7655/ab812f>.

- [168] L. Heymann, M.L. Weber, M. Wohlgemuth, M. Risch, R. Dittmann, C. Baeumer, F. Gunkel, Separating the Effects of Band Bending and Covalency in Hybrid Perovskite Oxide Electrocatalyst Bilayers for Water Electrolysis, *ACS Appl Mater Interfaces* 14 (2022) 14129–14136. <https://doi.org/10.1021/acsami.1c20337>.
- [169] X. Li, Y. Bai, Z. Cheng, Revealing the Correlation of OER with Magnetism: A New Descriptor of Curie/Neel Temperature for Magnetic Electrocatalysts, *Advanced Science* 8 (2021). <https://doi.org/10.1002/advs.202101000>.
- [170] M. Qu, X. Ding, Z. Shen, M. Cui, F.E. Oropeza, G. Gorni, V.A. de la Peña O’Shea, W. Li, D.-C. Qi, K.H.L. Zhang, Tailoring the Electronic Structures of the $\text{La}_2\text{NiMnO}_6$ Double Perovskite as Efficient Bifunctional Oxygen Electrocatalysis, *Chemistry of Materials* 33 (2021) 2062–2071. <https://doi.org/10.1021/acs.chemmater.0c04527>.
- [171] B. Prajapati, S. Roy, S. Sharma, A.G. Joshi, S. Chatterjee, A.K. Ghosh, Bandgap Engineering and Signature of Ferromagnetism in $\text{Ti}_{1-x}\text{Mn}_x\text{O}_2$ Diluted Magnetic Semiconductor Nanoparticles: A Valence Band Study, *Physica Status Solidi (b)* 256 (2019). <https://doi.org/10.1002/pssb.201800262>.
- [172] R. Xie, Z. Nie, X. Hu, Y. Yu, C. Aruta, N. Yang, Pr-Doped LaCoO_3 toward Stable and Efficient Oxygen Evolution Reaction, *ACS Appl Energy Mater* 4 (2021) 9057–9065. <https://doi.org/10.1021/acsaem.1c01348>.